HAL
open science

Synthesis of Strontium Cuprate (SrCu2O) by MOCVD as a P-type Transparent Conducting Oxide Thin Film

Afzal Khan

To cite this version:

Afzal Khan. Synthesis of Strontium Cuprate (SrCu2O) by MOCVD as a P-type Transparent Conducting Oxide Thin Film. Materials. Université de Grenoble, 2011. English. NNT : 2011GRENI008 . tel-00582901

HAL Id: tel-00582901

https://theses.hal.science/tel-00582901v1

Submitted on 4 Apr 2011

HAL is a multi-disciplinary open access archive for the deposit and dissemination of scientific research documents, whether they are published or not. The documents may come from teaching and research institutions in France or abroad, or from public or private research centers.

L'archive ouverte pluridisciplinaire **HAL**, est destinée au dépôt et à la diffusion de documents scientifiques de niveau recherche, publiés ou non, émanant des établissements d'enseignement et de recherche français ou étrangers, des laboratoires publics ou privés.

UNIVERSITÉ DE GRENOBLE

THÈSE

Pour obtenir le grade de

DOCTEUR DE L'UNIVERSITÉ DE GRENOBLE

Spécialité : **Matériaux, Mécanique, Génie Civil, Electrochimie**

Arrêté ministériel : 7 août 2006

Présentée par

« Afzal / KHAN »

Thèse dirigée par **« Jean-luc/DESCHANVRES »**

préparée au sein du **Laboratoire Laboratoire des Matériaux et du Génie Physique (LMGP)**
dans **l'École Doctorale Ingénierie - Matériaux, Mécanique, Energétique, Environnement, Procédés, Production (I-MEP2)**

Synthèse de Cuprates de Strontium (SrCu2O) par MOCVD comme couche mince d'oxyde transparent conducteur de type P

Thèse soutenue publiquement le **« 13 janvier 2011»**,
devant le jury composé de :

M. BELLET Daniel (Président)
M. GALTIER Pierre (Rapporteur)
M. TAILHADES Philippe (Rapporteur)
M. DESCHANVRES Jean-Luc (Directeur)
M. MODREANU Mircea (Examinateur)

Dedication

To my Kids

Being away from home, the moral and emotional support of my family played a vital role in energizing me for accomplishing this four and half years of research study in France. All time prayers of my parent and my wife, and good wishes of my kids made it possible to stay alone and concentrate on study.

Presence of the Pakistani students community in Grenoble was really a great source of support with whom one feels like at home. At the end I would like to thank Hajra Basit an Indian Ph.D student of Grenoble university, who really proved a good and cooperative friend.

Above All, I am thankful to the Almighty Allah, who gave me strength to complete this research study.

0.6.1 Principe de la CVD xxxvi

0.6.2 Le procédé MOCVD à injection xxxix

0.7 Analyse des résultats xliii

1 Introduction - Context and Background 1

1.1 Introduction 1

1.2 Context and Background 3

1.3 Thesis Organization 3

2 Transparent Conducting Oxides (TCOs) 5

2.1 TCO Theory 6

2.2 Historical Background 8

2.3 Structure Mechanism for TCO 9

2.4 Criteria for choosing TCOs 11

2.5 TCO Relevant Properties 12

2.5.1 Optical and electrical performance 12

2.5.1.1 Electrical Conductivity 14

2.5.1.2 Optical Transparency 14

2.5.2 Plasma Frequency 15

2.5.3 Other relevant factors 16

2.6 TCO's Applications 17

2.7 Types of TCOs 18

2.7.1 N-type TCOs 18

2.7.2 P-type TCOs 19

2.8 Problems in designing p-type TCOs 20

2.9 Chemical Modulation of the Valence Band 21

2.9.1 Copper-based delafossite structure 23

2.9.2 Copper-based non-delafossite structure 24

2.10 $SrCu_2O_2$ 25

2.10.1 Reports on SCO 28

2.11 Ba Doping of SCO 29

2.11.1 Reports on p-type TCOs 31

3 Thin Films Experimental Techniques 33

3.1 Thin Films Deposition Techniques 34

3.1.1 Physical Vapor Deposition Techniques 35

3.1.2 Chemical Deposition Techniques 37

3.2 Criteria for selection of a deposition technique 39

3.3 Material Characteristics 41

3.4 Thin films characterization techniques 44

3.5 Post-deposition Treatments 46

3.5.1 Annealing 46

3.5.1.1 Conventional Annealing 47

3.5.1.2 Rapid Thermal Process Annealing 48

3.5.2 Light Exposure 49

3.5.3 Aging 49

3.6 Thin Film Characterization Instruments 49

3.6.1 Electron Microscope 50

3.6.1.1 Scanning Electron Microscope 50

3.6.1.2 Transmission Electron Microscope 51

3.6.1.3 Atomic Force Microscope 52

3.6.2 X-ray Diffractometer 52

3.6.3 Fourier Transform Infrared Spectroscopy 52

3.6.4 Raman spectroscopy 53

3.6.5 UV-Visible Spectrometer 54

3.6.6 Ellipsometer 54

3.6.7 Four-point Probe Technique 55

3.6.8 Van der Pauw setup 55

4 Materials and Methods **57**

4.1 Thermodynamics of Sr-Cu-O system 58

4.2 CVD Principle and Film Growth 59

4.3 Structure of CVD Deposits 64

4.4 Types of CVD Reactors 66

4.4.1 Thermal CVD Reactor 67

4.4.2 Plasma-enhanced CVD Reactor 69

4.4.3 Photo-chemical CVD Reactor 69

4.5 Metal-Organic CVD (MOCVD) 70

4.6 MOCVD system at LMGP 72

4.6.1 Microvalve Injector 74

4.6.2 Evaporator and Delivery Line 76

4.6.3 Process Reactor 76

4.6.4 Precursor Solution Preparation 78

4.6.5 Deposition Parameters 79

5 Results and Discussion 81

5.1 As-deposited Films and their Characterizations 82

5.1.1 Visual Aspect 82

5.1.2 Morphological Characterization 83

5.1.3 Elemental Analysis 84

5.1.4 Uniformity of Elemental Composition 87

5.1.5 Thickness Uniformity 88

5.1.6 Chemical Phases 88

5.2 Post-Deposition Treatment 91

5.3 Phase Transformation Pathway 95

5.4 Slow and Fast Cooling of the films in Ar 102

5.5 Effect of Gas Flow rate 104

5.6 One Step N_2 Annealing 106

5.7 Film Deposition on Glass Substrates 107

5.8 Optical Transparency Measurement 115

5.9 Electrical Conductivity Measurement 123

6 Conclusions and perspectives **125**

6.1 Conclusions 125

6.2 Perspectives and further work 127

Bibliography **131**

List of Figures

1 La conception de gap de bande pour les conducteurs transparents. Les Photons visibles (2.1 à 3.1 eV) n'ont pas assez d'énergie pour exciter les électrons de la bande de valence vers la bande de conduction, ils ont l'énergie suffisante pour exciter les électrons du niveau donneur vers la bande de conduction (type n) ou de la bande de valence vers niveau accepteur (type p) xxix

2 Illustration schématique de la liaison chimique entre un ion oxyde et un cation qui a une configuration saturée de la couche électronique appropriée pour la technique CMVB [1] xxxi

3 Structure cristalline de delafossite, A et B indiquent cations monovalents et cations trivalents respectivement [2] xxxii

4 (a) Conception CMVB de la CBM et la VBM, et des orbitales moléculaires de la SCO [1]. (b) La structure cristalline de la SCO, des chaînes unidirectionnelles zigzages de -O-Cu-O-Cu-O- le long des directions [100] et [010] résulte la haute transparence de la SCO par élargissant du gap de bande [3] xxxiii

5 Diagramme de phase du système Sr-Cu-O. Variation en pression partielle de O_2 et de température donne lieu à des phases différentes chimique des oxydes de cuivre et de strontium. $SrCu_2O_2$ pour $\frac{Cu}{Sr}$ = 2 peuvent être obtenus à basse température et à faible pression partielle de O_2 et vice versa xxxv

6 Schéma les différentes des étapes d'un dépôt chimique en phase vapeur [4] xxxvii

7 Représentation des différents régimes de croissance d'un film déposé par CVD, en fonction de l'inverse de la température du substrat, pour deux valeurs de pression totale (P1>P2) [4] xxxviii

8 Zones d'évaporation et de décomposition de précurseur un système MOCVD à injection xli

9 schéma de la machine MOCVD dans LMGP utilisé pour dépôt xlii

10 Spectres de diffraction RX de dépôts MOCVD sur silicium à différentes températures montrent que $SrCO_3$ et CuO sont des principaux composants des couches brutes . . xliii

11 Spectres de diffraction RX de différents étapes de recuit RTP dans Ar pour 30 seonds à 600°C. Le troisième étape de recuit RTP produit SCO avec du Cu métallique . . . xliv

12 Analyse du recuit RTP en deux étapes (O_2 and Ar) par les spectres de diffraction RX. Le recuit du film brut sous O_2 pour 30 seconds à 600°C élimine $SrCO_3$ et produit $Sr_{14}Cu_{24}O_{41}$. La deuxième étape sous Ar donne SCO xlv

13 Analyse du recuit RTP en deux étapes (O_2 and Ar) par la spectroscopie FTIR. Le recuit du film brut sous O_2 pour 30 seconds à 600°C élimine $SrCO_3$ et produit $Sr_{14}Cu_{24}O_{41}$. La deuxième étape dans Ar donne SCO xlv

14 Effet de la température dans O_2 sur les phases $SrCO_3$ et CuO, et sur le pic de substrat de Si. Les pics de Raman pour CuO, Si, et $SrCO_3$ disparaissent et on trouve une nouvelle phase $Sr_{14}Cu_{24}O_{41}$ à 600 °C. xlvi

15 Inversion des phases pendant le refroidissement lent dans Ar xlvii

16 Perte de la phase SCO pendant le refroidissement lent à cause d'inversion entre SCO et $Sr_{14}Cu_{24}O_{41}$ et conservation de la phase SCO pendant le refroidissement vite . . xlvii

17 Recuit conventionnel dans N_2. La première étape de recuit dans N_2 à 600 °C pour 2 heurs donne $SrCuO_2$ et la deuxième étape à la même conditions donne SCO xlviii

18 Analyse Diffraction RX de la phase de SCO sur le substrat de verre. La phase pure de SCO sur le substrat verre se développe pendant 5 minutes de recuit conventionnel dans N_2 avec $SrCuO_2$ comme une phase intermédiaire qui se développe pendant 3 minutes. xlviii

19 L'effet de la durée de recuit et le vitesse d'échauffement sur la morphologie. (a) La morphologie de couche brute, (b) morphologie de couche après le recuit de 4 heurs avec le réchauffement lent, (c) morphologie de couche après le recuit de 5 minutes avec un échauffement rapide. xlix

20 (a) la transparence du substrat de verre, (b) la transparence de la couche mince SCO corresponde à image 19-c, (c) la transparence de la couche brute corresponde à image 19-a, (d) la transparence de la couche mince SCO corresponde à image 19-b . . . l

21 La Transparence en pourcentage de (a) substrat de verre, (b) couche mince de SCO sans substrat, et (c) couche mince de SCO avec substrat. L'insert est une trace de $(\alpha h\nu)^2$ et de lénergie de photon incident $h\nu$ pour calculer le gap de bande l

2.1 Sorting map of the materials (metals, semimetals, semiconductors) on the basis of conductivity in '$n - \mu$' correlation (electron carrier density n and electron mobility μ). The diagonal straight lines are the lines of constant conductivity [5] 6

2.2 Bandgap designing for transparent conductors. Visible photons (2.1-3.1 eV) do not have enough energy to excite electrons from valence band to conduction band, but have sufficient energy to excite holes (for p-type) from acceptor level to VB or electrons (for n-type) from donor level to CB [6] 10

2.3 Electronic band structures calculated for (a) undoped and (b) Sn-doped indium oxide. The Sn-doped Indium Oxide shows large bandgap and dispersed single s band the bottom of conduction band owing to high transparency and conductivity in comparison to undoped indium oxide 10

2.4 Schematic illustration of the chemical bond between an oxide ion and a cation that has a closed-shell electronic configuration suitable for CMVB technique [1] 21

2.5 Crystal structure of delafossite, A and B denote mono- and trivalent cations, respectively. DB stands for the dumbbell layers and ES for edge-sharing layers [2] 22

2.6 Crystal structure of (a) Cu_2O and (b) $SrCu_2O_2$. $SrCu_2O_2$ can be considered as derived from Cu_2O, in which one Cu atom is removed for each unite of distorted Cu_2O, plus an inter-penetrating body-centered tetragonal Sr sublattice [7] 25

2.7 (a) CMVB approach for CBM and VBM, and molecular orbitals for SCO [1]. (b) Crystal structure of SCO, the zigzag one dimensional chains of -O-Cu-O-Cu-O- running along [100] and [010] directions causes high transparency in SCO by enlarging the bandgap [3] 26

2.8 Calculated electronic band structures of (a) Cu_2O [7], (b) $SrCu_2O_2$ and (c) $CuAlO_2$ [8]. Clearly Cu_2O and $SrCu_2O_2$ have direct bandgaps, while $CuAlO_2$ has indirect bandgap. 27

2.9 Charge carrier generation mechanism in SCO. Positions of single particle levels in band gap of $SrCu_2O_2$ at the Γ point. Empty circles indicate holes and arrows indicate electrons in the up/down spins [9]. 27

4.1 Phase diagram of Sr-Cu-O system. Variation in O_2 partial pressure and temperature gives rise to various chemical phases of strontium copper oxides. $SrCu_2O_2$ for $\frac{Cu}{Sr} = 2$ can be obtained at low temperature for low O_2 partial pressure and vice versa [10]. 59

4.2 Sequence of stages involved in vapor phase chemical deposition of thin film [4]. . . 61

4.3 Dependence of CVD deposition rate on temperature and pressure (P_1<P_2). Growth rate increases in the surface reaction region, remains almost constant in mass transport region, and decreases in precursor depletion region [4]. 63

4.4 Dependence of CVD deposition rate on reactant concentration. Increase in reactant concentration increases the deposition rate till the precursor depletion occurs due to gas phase nucleation [11] 64

4.5 The effects of supersaturation and temperature on the structure of CVD deposits. Change in supersaturation and substrate temperature yield amorphous to epitaxial films [12]. 65

4.6 Schematic diagram of MOCVD deposition system in LMGP for thin film deposition. 73

4.7 a) Image of the injector and precursor container assembly, b) Image of the micro droplets in the evaporator after injection 75

4.8 Evaporation and reaction zones of the MOCVD system in LMGP 77

4.9 Organic chemical structure of precursors and solvent 78

5.1 Digital camera images of the films deposited at various temperatures. Image (a) corresponds to lower deposition temperature yielding only a dark strip at the border, image (b) represents film deposited at high temperature, and image (c) corresponds to higher temperature of deposition film showing a rough and diffusive visual aspect 83

5.2 Comparison of SEM images of films deposited at various temperatures. Films deposited at higher temperature shows diffusive aspect due to formation of aggregates of grains 83

5.3 SEM-FEG high resolution images of the film for thickness and grain size measurements 84

5.4 The Cu to Sr ratios at different deposition temperatures in the film measured by WDX versus their molar ratios in the solution. The $\frac{Cu}{Sr}$ ratio in film decreases with the increase in temperature due to the increase of Sr content in the film 85

5.5 Cu/Sr+Ba ratio in the precursor solution versus Cu/Sr+Ba ratio in the as-deposited film, higher deposition temperatures tend to reduce Cu/Sr+Ba ratio in the film . . . 86

5.6 Effect of doping percentage on Cu/Sr ratio in the film. Low doping (5-15%) of Ba doping do not change significantly the Cu to Sr ratio in the film. 86

5.7 Radial variation of elemental composition along the diameter of circular Si substrate 87

5.8 Measure of film thickness variation on 4 inch Si wafer. Thickness goes on decreasing as one moves away from the center 88

5.9 XRD pattern of the as-deposited films deposited at various temperatures showing $SrCO_3$ and CuO as main components of the as-deposited films 89

5.10 FTIR analysis of the as-deposited film showing characteristic peaks of $SrCO_3$ and CuO 89

5.11 Raman peaks of the as-deposited film with 520.9 cm^{-1} as the Si substrate peak and rest of the peaks correspond to CuO $SrCO_3$ 90

5.12 XRD analysis of the RTP annealed film under Ar 91

5.13 XRD analysis of the two steps RTP annealed film under O_2 and Ar. RTP under O_2 completely decompose $SrCO_3$ and gives rise to new phase Cu_2SrO_3. RTP under Ar then leads to SCO phase along with a very small quantity of metallic copper 93

5.14 XRD analyses of the two steps RTP annealed film under O_2 and Ar with low copper concentration in the precursor solution that results in a pure SCO phase 94

5.15 Elimination of Cu contents by O_2 annealing at low temperature as 300 °C. 94

5.16 FTIR analysis of the two steps RTP annealed film under O_2 and Ar. O_2 annealing above 500 °C decompose carbonates and develops $Sr_14Cu_24O_41$ (peaks at 490 cm^{-1} and 540 cm^{-1} and Ar annealing at 600 °C leads to SCO phase (peak at 570 cm^{-1}) . 95

5.17 In-situ Raman spectra of the as-deposited film on Si substrate at room temperature . 96

5.18 Shift in the Raman peaks with the increase in temperature in O_2 atmosphere. The peaks for CuO, Si substrate, and $SrCO_3$ disappear and new phase $Sr_14Cu_24O_41$ appears 97

5.19 Devolution and shifting of Si peaks towards lower frequency value with the increase in annealing temperature under O_2 98

5.20 New phase formation with replacement of O_2 by Ar 99

5.21 Reversal of phase on slow cooling of the film under Ar 100

5.22 In-situ XRD study of transformation pathway of Sr-Cu-O system 101

5.23 Confirmation of In-situ XRD study of transformation pathway in figure 5.22 101

5.24 Conventional annealing system with fast and slow cooling facility. Moving the furnace away from the sample and allowing high gas flow rate results in fast cooling of the sample 102

5.25 Fast and slow cooling rate under Ar. Movable furnace arrangement and heavy flow of gases reduce the cooling duration from 200 to 8 minutes 103

5.26 Fast cooling under Ar gives rise to SCO, while slow cooling to $Sr_14Cu_24O_41$ phase 104

5.27 Effect of gas flow rate during annealing on the chemical phases. No or low gas flow (< 5 lit/min) cannot develop SCO phase, while heavy gas flow ($\geq$ 5lit/min) is sufficient to develop SCO phase. 105

5.28 Effect of gas flow rate during annealing on the film morphology. The big white spots may correspond Cu_3Si phase formed at high temperature during annealing due to low or no gas flow 105

5.29 Formation of Cu_3Si phase due to diffusion of Cu into Si substrate 106

5.30 Conventional annealing under N_2 107

5.31 XRD analysis of SCO phase on glass substrate. Pure SCO phase in films glass develops after 5 minutes conventional annealing under N_2 with $SrCuO_2$ as an intermediate phase which develops during 3 minutes. 108

5.32 5 minutes annealing in N_2 at 680 °C give rise to SCO phase. 109

5.33 Effect of long annealing ($\geq$4 hours) in N_2 at 650 °C. Sr contents in film defuse into the substrate and the film is composed of only Cu_2O 110

5.34 Cross-sectional view of the prolonged annealed film on glass substrate by TEM. EDX analysis were performed at Points 1,2,3 and 4. 110

5.35 EDX analysis of the points 1,2,3 and 4 shown in figure 5.34. 111

5.36 Cross-sectional view of the SCO film on glass substrate obtained after short annealing (5 minutes) by TEM. EDX analysis were performed at Points 1,2,3...7. 112

5.37 EDX analysis of the points 1,2,3,4 and 5 shown in figure 5.36. 113

5.38 EDX analysis of the points 6 and 7 shown in figure 5.36. 114

5.39 Ex-situ Raman study of 3 and 5 minutes annealing effect at 650 °C. Annealing under N_2 for 3 minutes leads to $SrCuO_2$ and Cu_2O, and SCO phase appears after 5 minutes. 115

5.40 Transparency measurement of as-deposited and SCO thin film on glass substrate. As-deposited film shows higher transparency than SCO 116

5.41 Morphology comparison of the film before and after conventional annealing. Wides cracks in the film appear after conventional annealing 117

5.42 Morphological comparison of the RTP and slow heated conventionally annealed films. RTP annealed film has no cracks due to high heating and cooling rate, and short annealing duration 118

5.43 Conventional annealing system with high heating and cooling rate facility. High heating and cooling rate is achieved by moving the heated furnace towards and away from the sample 119

5.44 Conventionally annealed films with high heating and cooling rate. High heating and cooling rate greatly reduce cracks in the film 119

5.45 Transparency measurement of (a) glass substrate, (b) low thickness film with small cracks, (c) high thickness film with small cracks, (d) as-deposited film, and (e) film with wider cracks. Film with small cracks and low thickness shows high transparency 120

5.46 Transparency measurement of (a) glass substrate, (b) film without substrate, and (c) film along with substrate. The inset shows plot of $(\alpha h\nu)^2$ versus photon energy $h\nu$. 121

5.47 Slow and fast heating. Movable pre-heated furnace arrangement shown in figure 5.43 reduce heating time form 24 to 4 minutes 122

5.48 Effect of annealing duration on magnitude of crack formation. Longer annealing duration tends to produce wide cracks and vice versa 123

5.49 Almost complete removal of the film after very long annealing duration 124

List of Tables

2.1 Minimum required properties of TCOs 12

2.2 Reports on SCO with its corresponding deposition techniques and its opto-electrical properties 29

2.3 Cu vacancy formation energy in the undoped, Ca-doped and Ba-doped SCO 30

Abbreviations

TCO	Transparent Conducting Oxide
SCO	Strontium Coper Oxide $SrCu_2O_2$
NATCO	Novel Advanced Transparent Conducting Oxide
MOCVD	Metal Organic Chemical Vapor Deposition
PLD	Pulsed Laser Deposition
LMGP	Laboratoire des Matériaux et du Génie Physique
ITO	Indium Tin Oxide
VB	Valence Band
VBM	Valence Band Maximum
CB	Conduction Band
CBM	Conduction Band Minimum
UV	Ultra Violet
IR	Infrared
YSZ	Yttrium Stabilized Zirconia
CMVB	Chemical Modulation of the Valence Band
CVD	Chemical Vapor Deposition
PVD	Physical Vapor Deposition
MBE	Molecular Beam Epitaxy

WDX	Wavelength Dispersive X-ray
EDX	Energy Dispersive X-ray
FTIR	Fourier Transform Infrared)
SEM	Scanning Electron Microscope
TEM	Transmission Electron Microscope
RTA	Rapid Thermal Annealing
RTP	Rapid Thermal Process
CA	Conventional Annealing
AFM	Atomic Force Microscope

Abstract

Transparent Conductive Oxides (TCOs) are simultaneously optically transparent and electrically conductive materials. TCOs continue to be in high demand for their immediate applications in a variety of new technologies ranging from thin film coating and sensor devices to light detecting and emitting devices in telecommunications. All TCOs can be classified into two major classes; p-type and n-type. However, n-type TCOs are most readily available and therefore more commonly found in practical applications. Among the n-type TCOs reported so far, Indium Tin Oxide (ITO) has the lowest resistivity (10^{-4} Ωcm) and good transparency (80-90%). However, ITO on one hand is very expensive and scarce and on the other hand just half part of the story; as the goal is to develop the "transparent electronics" as the next generation of electronics.

Development of p-type TCOs is thus an undeniable fact. Until now, so many p-type TCOs have been reported after NiO as a first p-type TCO 1993. However, $SrCu_2O_2$ has been found a promising candidate for p-type TCOs because of its direct bandgap and due to the fact that it can be deposited at relatively low temperature. The principal application of TCO is in the form of thin film as transparent electrode in solar cells, gas sensors, and LCD screens etc,. Several different deposition techniques are used to deposit TCO thin films with superior optoelectrical properties. We selected Metal Organic Chemical Vapor Deposition (MOCVD) technique due to its low cost, high speed and large area deposition facilities.

Undoped, K-doped, Ca-doped, and CaO-doped SCO has already been reported using Pulsed Laser Deposition (PLD), e-beam evaporation and spin coating techniques respectively. However, the obtainable optoelectrical properties are much inferior than those of the n-type TCOs. We synthesized Ba-doped SCO as the theoretical calculations of Ba-doped SCO reveals better performance in terms of optical transparency and electrical conductivity compared to previously reported undoped and doped SCO.

As-deposited films regardless of the deposition temperature were always composed of $SrCO_3$ and CuO, and according to the in-situ Raman and XRD characterizations high temperature (600 °C) annealing with fast cooling is necessary to obtain SCO. Optical transparency and electrical conductivity of a homogeneous and well adherent Ba-doped SCO is in the range of previously reported K-doped and Ca-doped SCO. However, explicit role of Ba-doping in enhancing optoelectrical properties of SCO has not yet determined in this research work due to the reproducibility problem in post-deposition annealing conditions.

Résumé

0.1 Introduction

Dans cette thèse, nous abordons le sujet des couches minces transparents semi-conducteurs de type oxyde, communément appelés TCO (Transparent Conducting Oxides). Les TCOs sont des matériaux qui possédent à la fois conductivité électriques et la transprance optiques. Pour les applications technologiques, on utilise les TCOs comme des électrodes transparentes dans des cellules solaires, des écrans à cristaux liquides, des écrans tactiles etc. Les TCOs sont de deux types; soit n soit p, selon la polatié des porteurs de charge. Toutefois, les applications technologiques sont actuellement limitées, car les TCO possédant des propriétés électriques et optiques satisfaisantes sont des semi-conducteurs de type n uniquement. Dans ce cadre, l'oxyde d'indium dopé par l'étain (ITO) ptésent la meilleure conductivité (10^4 Scm^{-1}) et une transparence supérieure à 80% dans le spectre visible. Mais l'ITO souffre de la rareté de l'indium et du fait qu'il est trop cassant pour être déposés sur des substrats souples. Le dépôt d'ITO demande également un traitments à haute température, réduisant ainsi le choix de son substrat. Donc, il est important de trouver des nouveaux TCOs de haute qualité. Tout particulirement de type p pour permetre la fabrication d'une jonction pn transparente qui constiturait la fondation de "l'électronique transparente". Dans le futur, les applications de l'électronique transparente incluront la fabrication de circuit invisible pour les systèmes de sécurité et la communication optique etc. Parmi les TCOs de type p

rapportés jusqu'à présent, le $SrCu_2O_2$ (SCO) présente propriétés très interessantes liée à son large gap direct. Le SCO non-dopé est de faible conductivité et transparence, donc pour l'augmentater sa conductivé et sa transparance, on a besoin d'un meilleur dopant. Basée sur des calcules théorétique développes dans le cadre du pojet éuropen "NATCO" (Novel Advanced Transparent Conducing Oxides) par M. Nolan du Tyndall Institute, nous avons choisi d'utiliser le Ba comme dopant pour SCO.

Il y a beaucoup de techniques pour le dépôt de couche mince. On a choisi la MOCVD (Metal Organic Chemical vapor Deposition) comme technique de dépôt à cause de son coût bas et de sa grande vitesse de dépôt. Dans notre cas les couches minces déposées par MOCVD sont des phases $SrCO_3$ et CuO. Donc pour obtenir la phase SCO, quelques étapes de recuit sont obligatoires. On a utilisé deux types de recuit; RTP (recuit thermique rapide) et recuit conventionel. Pour les couches minces déposées sur les substrats Si, le recuit RTP conduit à la bonne phase de SCO à 600 °C pendant 30 seconds dans le gaz oxygène et puis dans le gaz argon. La même conditions de RTP sont valable aussi pour le recuit conventionnelle pour une durée de recuit plus longe (une heure et 30 minutes) avec refroidissement rapide. Si la température de recuit augmente, la durée de recuit diminue. Donc on a obtenu la phase SCO avec recuit conventionnel de 5 minutes à 650 °C dans azote gazeux.

Les propriétés électrique et optique varient avec la taille des fissures qui se développent dans la couche mince pendant le recuit. Pour obtenir des propriétés électrique et optique meilleures, la taille des fissures doit être la plus réduite possibles. La valeur de conductivité electrique que nous avons mesurée est de 4.3×10^{-2} Scm^{-1}, la valeur du gap est de 3.26 eV et la transparence est de 75% à 550 nm.

0.2 La Théorie de TCO

Les TCOs sont des matériaux avec un large gap ($\geq$ 3.1 eV) et exposent un comportement de semi-conduction de l'ordre de 10^4 Scm^{-1}. Donc , cette valeur ne peut pas être obtenue pour des matériaux conventionnels avec une valeur de gap de bande plus que 3.1 eV. Le comportant transparent et semi-conducteur simultanément est basé soit sur un niveau donneur proche du la bande de conduction soit sur un le niveau accepteur proche du haut de la bande de valence. Dans cette situation, un photon visible n'a pas d'énergie pour exciter les électrons de la bande de valence vers la bande conduction. Par contre, il a l'énergie suffisante pour exciter les électrons du niveau donneur vers la bande de conduction dans le cas de TCO de type n ou pour exciter les électrons de la bande de valence vers niveau accepteur en cas de TCO de type p. Cette situation théorique est presenté dans la figure 1 suivant [6].

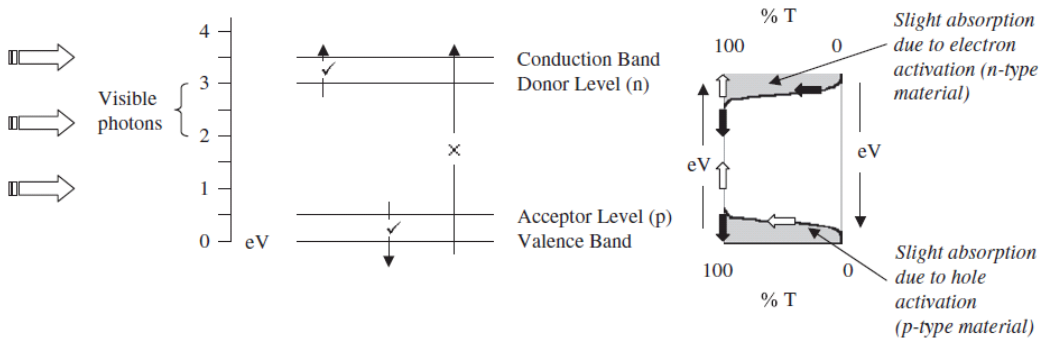

Figure 1: La conception de gap de bande pour les conducteurs transparents. Les Photons visibles (2.1 à 3.1 eV) n'ont pas assez d'énergie pour exciter les électrons de la bande de valence vers la bande de conduction, ils ont l'énergie suffisante pour exciter les électrons du niveau donneur vers la bande de conduction (type n) ou de la bande de valence vers niveau accepteur (type p)

En plus, un haute niveau de dopage est aussi important pour obtenir des TCOs de haute efficacité en terme de conductivité et de transparence.

0.3 TCOs de type p

Il y a deux type de TCOs par rapport à la polarité de porteurs de charge. Les TCOs sont de “type n” si les porteurs de charge sont des électrons et si les porteurs de charge sont des trous, les TCOs s’appellent de “type p”. Les TCOs de type n sont disponibles depuis 1960 et sont utilisé dans nombreuses applications technologiques. A notre connaissance, il y n’a aucun TCO de type p qui peut être utilisé dans des applications technologiques. La raison de cette non utilisation des TCOs de type p est leur faible conductivité et faible transparence. Des nombreux oxydes métalliques ont des larges bande interdites en raison des liaisons ioniques entre les cations métalliques et les ions d’oxygǹes. La nature ionique des liaisons chimiques supprime la formation des niveaux peut profond, i.e. niveaux donneur ou accepteur, facilement ionisables et renforce également la localisation des électrons et des trous. Cependant, les oxydes métallique (métaux lourds) de bloc p avec des configurations électroniques ns^0 (où n est le nombre quantique principal) tels que ZnO, CdO, In_2O_3, SnO_2, PbO_2, Sb_2O_3 et leurs oxydes mixtes peuvent être changé en semi-conducteurs de type n par le dopage des électrons. Mais, la situation pour les TCOs de type p n’est pas aussi simple que pour les TCOs de type n en raison de la localisation forte des trous positifs dans la bande de valence de l’oxyde métallique qui ne peuvent pas migrer sous l’effet d’un champ électrique défini. En effet pour les type n, le minimum de la bande de conduction (CBM) des oxydes métalliques est constitué d’orbitales s sphérique de métal spatialement étalé et la haute conduction électrique est possible si une haute densité de dopage d’électrons est atteint. Par contre les types p le maximum de la bande de valence (VBM) est constitué d’orbitale 2p d’oxygène qui est située plus bas que l’orbite de valence des atomes métalliques. A cause de la grande électronégativité de l’oxygène, les trous positifs introduites sont localisés près des ions d’oxygène et poursuivent un piège de profondeur. Par ailleurs, la dispersion spatiale de la bande de valence est faible et donc le niveau VBM est plus profond que le dopage de trous

est difficile. Etant donné que cette localisation est due à l'ionicité des oxydes métalliques, la solution proposée a été l'introduction d'un caractère de covalence dans la liaison métal-oxygène pour la formation de bande de valence plus étalé. Cette méthode d'obtention TCOs de type p est appelé modulation chimique de la bande de valance (CMVB) telle que proposé par H. Kawazoe et al [13].

0.4 Modulation Chimique de la Bande de Valance

Modulation Chimique de la Bande de Valance (CMVB) est une méthode pour induire un caractère de covalence dans la liaison métal-oxygène afin de permettre une délocalision des trous dans la bande de valence des matériaux oxydes. Toutefois, cette méthode a besoin du choix approprié à la fois des espèces cationiques et des structures cristallines. Si le niveau d'énergie de la couche électronique supérieure saturée du cation métallique est presque équivalent à cellui des niveaux 2p des ions d'oxygène (comme illustré dans la figure 2), des liaisons chimiques avec une covalence considérable seront formées entre les cations métalliques et les anions oxydes.

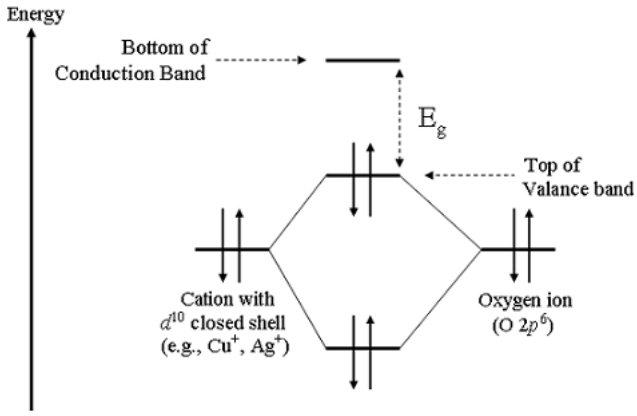

Figure 2: Illustration schématique de la liaison chimique entre un ion oxyde et un cation qui a une configuration saturée de la couche électronique appropriée pour la technique CMVB [1]

Dans ce cas une configuration avec la couche électronique pleine est nécessaire pour éviter l'absorption optique dans le spectre visible. Les investigations ont montré

que les espèces cationiques requises sont les ions Cu^+ du niveau électronique saturé de la forme $3d^{10}$ ou les ions Ag^+ du niveau électronique saturé de la forme $4d^{10}$.

La deuxième condition est la structure cristalline pour avoir des TCOs de type p. La coordination tétraédrique des ions d'oxygènes est intéressante pour la conductivité de type p, parce qu'elle réduit la localisation des électrons 2p des ions d'oxygènes. Cela justifie le fait que le Cu_2O est un conducteur oxyde de type P, mais avec une faible transparence due à une bande interdictie trop faible. La faible transparence de Cu_2O est attribuée à des interactions en trois dimensions entre les électrons de $3d^{10}$ des ions du Cu^+. Il est prévu que la structure cristalline de faible dimension augmente la bande interdite et donc la transparence. Les matériaux avec des structures delafossites (figure 3) ont une transparence plus grande que Cu2O à cause des interactions en deux dimensions entre les atomes de Cu proche voisin.

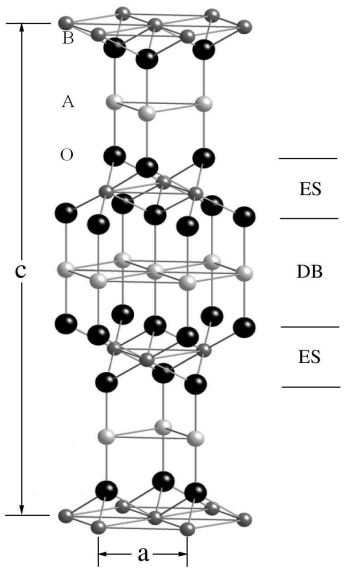

Figure 3: Structure cristalline de delafossite, A et B indiquent cations monovalents et cations trivalents respectivement [2]

Dans la catégorie de structure delafossite, il y a deux groupes de TCOs de type p; $CuBO_2$ basé sur le Cu et $AgBO_2$ basé sur le Ag, où B est un cation trivalent. Cepen-

dant, la plupart des matériaux semi-conducteurs delafossite de type p sont basés sur le Cu. Les matériaux de structure delafossite basés sur Ag sont difficiles à synthétiser par une réaction simple à l'état solide. Les delafossites à base de Cu ont une plus grande mobilité de trous en raison du caractère Cu-3d de la bande de valence. Cependant que, le delafossites à base de Ag sont de caractère O-2p, et les trous de d-manifold sont plus mobiles que celle de p-manifold.

Le matériau plus étudié dans le groupe des delafossites basés sur le Cu, est le $CuAlO_2$ (CAO). Après la première publication sure CAO comme un TCO de type p, un nouveau domaine de recherche "lélectronique transparente" a émergé. Les autres TCOs de type p dans ce groupe sont: $CuGaO_2$, $CuInO_2$, $CuCrO_2$, $CuYO_2$, et $CuScO_2$ etc,.

Les structures delafossites ont bien satisfait les conditions pour obtenir des TCOs de type p en suivant la technique CMVB. Comme extension de cette idée, une autre phase cristalline $SrCu_2O_2$ (SCO) a été examinée en suivant la technique CMVB, mais cette structure cristalline n'est pas celle de delafossite.

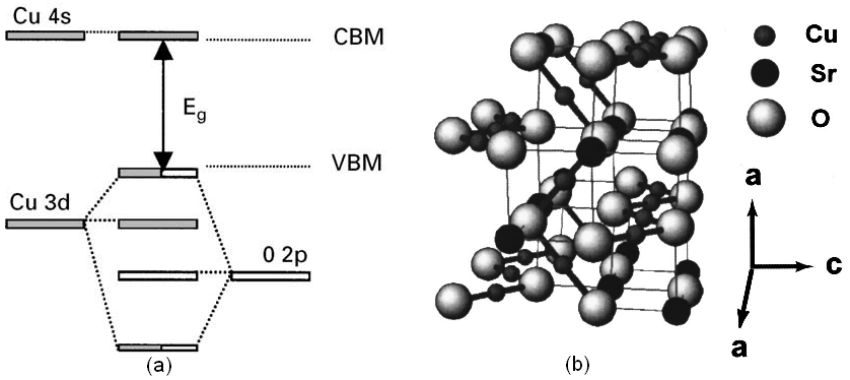

Figure 4: (a) Conception CMVB de la CBM et la VBM, et des orbitales moléculaires de la SCO [1]. (b) La structure cristalline de la SCO, des chaînes unidirectionnelles zigzages de -O-Cu-O-Cu-O- le long des directions [100] et [010] résulte la haute transparence de la SCO par élargissant du gap de bande [3]

Dans le cas des structures delafosites, l'interaction entre les atomes voisins est

en deux dimensions, par contre les atomes voisins dans le SCO interagissent dans un zigzag unidimensionnel comme le montre la figure 4.

0.5 Thermodynamiques de système Sr-Cu-O

La compréhension de la thermodynamique des matériaux réactifs et du principe de croissance sont essentiels pour la fabrication de couches minces. Roth et al. ont étudié les équilibres de phases du système SrO-CuO et ont déterminé son diagramme de phase. Basé sur ce diagramme de phase, ils ont trouvé trois composés; Sr_2CuO_3, $SrCuO_2$, et $Sr_{14}Cu_{24}O_{41}$ [14]. Par la suite, C. B. Alcock et B. Li ont étudié la thermodynamiques du système Sr-Cu-O et ont établi l'existence de la phase $SrCu_2O_2$ avec Sr_2CuO_3, $SrCuO_2$ et $Sr_{14}Cu_{24}O_{41}$ [15, 16]. Le système Cu_2O-SrO a été étudiée par C.L. Teske and H.K. Muller-Buschbaumdans dans les différents rapports molaires par frittage sous argon à 1220 K. Ils ont trouvé que le rapport de Cu_2O:SrO = 1:1 donne la phase $SrCu_2O_2$ [17]. L'étude thermogravimétriques de $Sr_{14}Cu_{24}O_{41}$ a été faite en faisant varier la quantité d'oxygène et la température. Il a été trouvé que ce composé est stable seulement à une pression partielle d'oxygène supérieure à 6 kPa et à une temperature égale à 1193 K, il se décompose en $SrCuO_2$ et CuO lorsque la pression partielle d'oxygène est inférieure à 6 kPa. Les trois différentes étapes de la décomposition ont été observées sous une pression partielle d'oxygène de 200 Pa à 1193 K. La première étape correspond à la décomposition $\frac{2}{3}Sr_{14}Cu_{24}O_{41} = \frac{28}{3}SrCuO_2 + \frac{20}{3}CuO + O_2$, dans la deuxième étape, CuO se décompose en Cu_2O, i.e. $4CuO = 2Cu_2O + O_2$, et la troisième étape conduit à la formation de $SrCu_2O_2$, i.e., $4SrCuO_2 + 2Cu_2O = 4SrCu_2O_2 + O_2$ [15, 16]. Cette dernière phase est la phase d'équilibre sous les conditions expérimentales. Cependant, la coexistence de $SrCuO_2$ et $SrCu_2O_2$ a également été confirmée [15]. Le diagramme de phase (figure 5) basée sur les travaux de Suzuki et al. montre les différents domaines de phases du Sr-Cu-O en fonction de la pression partielle d'oxygène et de la température pour un ratio fixe de métaux Cu / Sr = 2, qui

est approprié pour le $SrCu_2O_2$ [10].

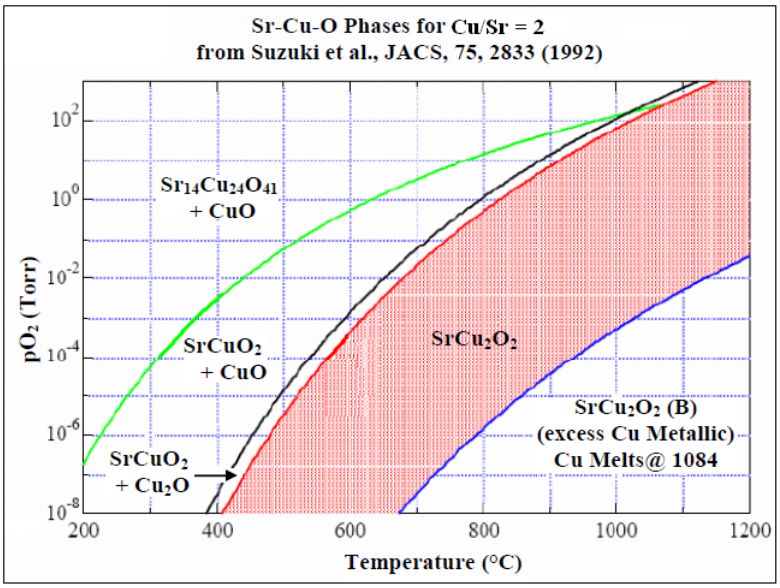

Figure 5: Diagramme de phase du système Sr-Cu-O. Variation en pression partielle de O_2 et de température donne lieu à des phases différentes chimique des oxydes de cuivre et de strontium. $SrCu_2O_2$ pour $\frac{Cu}{Sr}$ = 2 peuvent être obtenus à basse température et à faible pression partielle de O_2 et vice versa

Le diagramme de phase présenté dans la figure 5 a été construit pour des échantillons massif de Sr-Cu-O, recuit à différentes températures dans un environnement d'oxygène réduite. Toutefois, les couches minces de Sr-Cu-O suivent également la même transition de phase avec certaines déviations [18].

0.6 Elaboration par MO-CVD

De très nombreuses techniques d'élaboration en couche mince existent avec une grande diversité en terme de coût, de qualité, de contraintes thermiques, entre autres. Il en existe deux grandes catégories ; les techniques physiques (ablation laser, pulvérisation cathodique, etc,.) et chimiques (procédés sol-gel et CVD, etc,.). Cependant il existe des techniques hybrides alliant à la fois des phénomènes physiques et chimiques telle la CVD assistée par plasma.

Les techniques physiques produisent des dépôts de grande qualité, cependant elles nécessitent souvent un vide poussé et/ou des températures élevées. Ces contraintes limitent la nature des substrats utilisables. De plus elles induisent des coûts qui selon l'application peuvent être prohibitifs. La CVD dite classique a été conçu comme alternative bon marché à ces techniques. Elles consistent à décomposer thermiquement les précurseurs gazeux des matériaux à déposer. La nature gazause des précurseurs, en restreignant, le nombre des produits utilisables, constitue une importante limitation. Celle-ci a été levée avec l'apparition de la CVD utilisant des précurseurs organométalliques (MOCVD) solides sous forme de poudre. Ces produits ont une volatilité suffisante pour des température de l'ordre de la centaine de degré Celsius. Cela permet un débit de réactants élevé. Cependant cette technique n'est pas exempte d'inconvénients:

- le débit de vapeur est difficile à contrôler car il dépend/évolue au cours du temps en fonction de la quantité restante, de la répartition et de la morphologie de la charge de précurseur.
- il faut chauffer les vapeurs à température constante durant l'élaboration, car leur recondensation sur les points froids ou leur décomposition prématurée sur les zones chaudes sont à éviter. Ceci nécessite l'utilisation de vannes résistantes à haute température (200 °C), très onéreuses.

La solution à ces problèmes est alors d'employer des précurseurs solides dissous dans des solvants ou bien directement des précurseurs liquides.

0.6.1 Principe de la CVD

La CVD est basée sur la décomposition de molécules de précurseurs à l'état vapeur adsorbées à la surface d'un substrat. La modélisation de l'écoulement des gaz au voisinage du substrat conduit à introduire le concept de couche limite. Il s'agit d'une zone de transition dans laquelle la vitesse du flux gazeux passe de sa valeur

moyenne loin du substrat à une valeur nulle à la surface de celui-ci. Le processus CVD a lieu intégralement à l'intérieur de cette couche. Les paramètres de cette zone tels que le gradient thermique et le gradient de concentration des espèces réactives contrôlent donc le dépôt. En particulier l'apport de matière à la surface du substrat dépend des coefficients de diffusion des espèces et de l'épaisseur de la couche limite. Une fois les espèces actives adsorbées à la surface, ce sont les lois de la thermodynamique chimique qui vont déterminer les réactions qui ont lieu. La qualité du dépôt résulte de leur cinétique respective.

La figure 6 suivante décrit les étapes du processus.

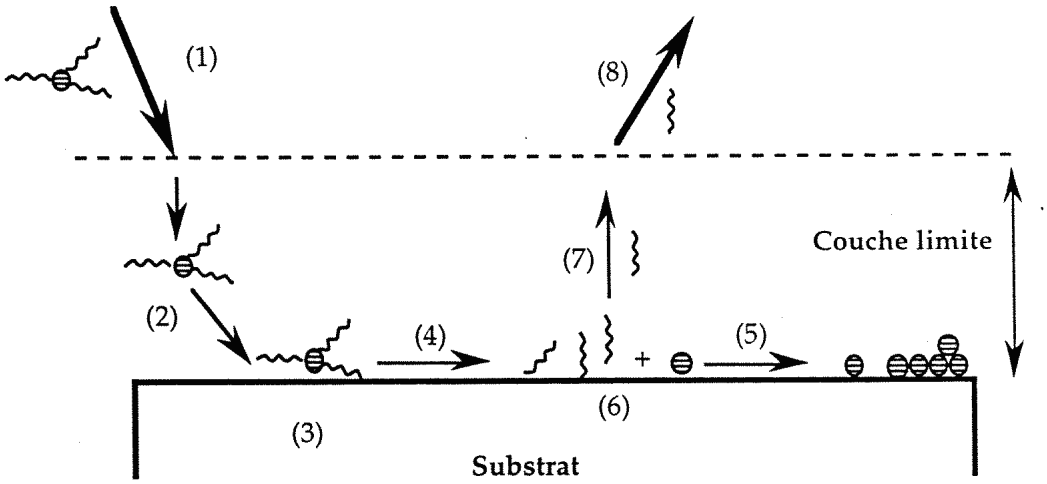

Figure 6: Schéma les différentes des étapes d'un dépôt chimique en phase vapeur [4]

1. transport en phase gazeuse des précurseurs vers la couche limite;
2. diffusion des molécules de précurseurs à travers la couche limite;
3. adsorption de ces molécules à la surface du substrat;
4. décomposition des molécules;

5. diffusion des atomes à la surface et fixation sur un site de nucléation ou de croissance du film;
6. dans le même temps, désorption des produits de la réaction (4);
7. transport de ces produits à travers la couche limite;
8. évacuation des produits.

Parmi ces différentes étapes, c'est la plus lente qui va déterminer la cinétique du dépôt. Sur un diagramme d'Arrhenius, où la vitesse de dépôt (en échelle logarithmique) est représentée en fonction de l'inverse de la température du substrat, trois régimes de croissance se distinguent (figure 7)

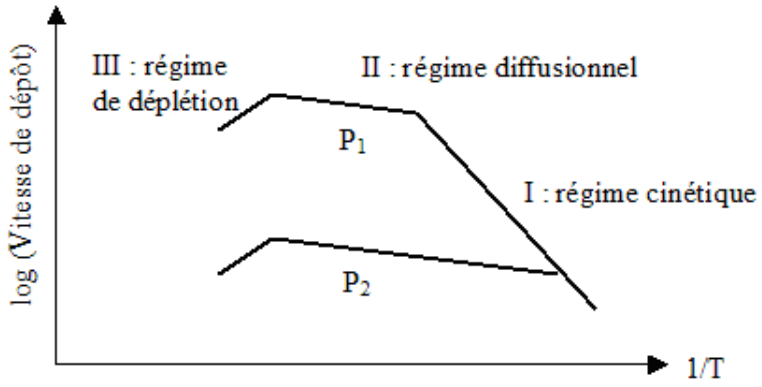

Figure 7: Représentation des différents régimes de croissance d'un film déposé par CVD, en fonction de l'inverse de la température du substrat, pour deux valeurs de pression totale (P1>P2) [4]

- Aux températures les plus basses, la vitesse de dépôt est limitée par la cinétique des réactions de surface (régime I). Ces réactions étant activées thermiquement, la vitesse de croissance augmente fortement avec la température.
- Au-delà d'une température critique, la cinétique des réactions devient plus rapide que celle d'apport de matière. Le facteur limitant est alors la diffusion des es-

pèces actives à travers la couche limite, qui dépend peu de la température. Ce régime est dit diffusionnel (régime II).

- Lorsque l'on augmente encore la température, une chute de la vitesse de croissance s'observe. Cette diminution a pour origine une chute de la concentration des espèces actives à l'intérieur de la couche limite. Cette chute résulte elle-même de la réaction prématurée des espèces chimiques soit en phase homogène, soit en phase hétérogène sur les parois de l'enceinte de la réaction. C'est le régime de déplétion (régime III).

Chacun de ces régimes a des avantages et des inconvénients. Par exemple, déposer à haute température permet de réaliser des films sans impuretés et bien cristallisés. Cependant le rendement de dépôt n'est pas satisfaisant (régime de déplétion).

Se placer en régime diffusionnel donne accès aux vitesses de croissance les plus élevées, ce qui permet de réduire le temps de dépôts. De plus ce régime est peu sensible aux fluctuations de température (c'est à dire en régime cinétique). On peut alors obtenir un dépôt conforme, c'est à dire sans amincissement de la couche au niveau du passage des marches sur les substrats présentant des reliefs.

Comme la température, la pression a une influence notable sur la cinétique de dépôt. Lorsqu'elle diminue, le coefficient de diffusion des espèces augmente, ce qui permet d'atteindre des vitesses de croissance plus élevées (cf figure 7). En outre cela étend le domaine sur lequel la croissance est contrôlée par la cinétique de réaction (régime cinétique).

0.6.2 Le procédé MOCVD à injection

La MOCVD à injection est basée sur l'évaporation flash de micro quantités de solution renfermant les précurseurs est dans une enceinte sous vide. Toute l'originalité de cette technique dans la source de précurseurs. Elle repose sur l'utilisation de micro

électrovannes rapides employées dans l'industrie automobile sur les moteurs dits à "injection électronique".

Ce que l'on nomme "source" dans le cadre de ce procédé est l'ensemble injecteur-réservoir. Chaque électrovanne est couplée à un réservoir en verre pressurisé par une arrivée de gaz neutre et contenant la solution source. Les sources sont montées à l'extérieur du réacteur. Seul le "nez" de l'injecteur y pénètre. Les solutions utilisées sont constituées des différents précurseurs organométalliques dissous dans un solvant adapté à ce procédé.

L'ouverture de l'injecteur est pilotée par ordinateur au moyen d'un boîtier d'alimentation et d'une carte électronique. En effet des temps d'ouverture très brefs (de l'ordre de la milliseconde) sont nécessaires pour injecter des micro quantités de solution. Les gouttelettes sont injectées dans une enceinte sous vide, puis vaporisées dans un évaporateur. L'enceinte est thermostatée à une température au moins égale à celle de l'évaporateur. Il est en effet essentiel de maintenir un gradient thermique positif entre la zone d'évaporation et de réaction, afin d'éviter toute recondensation ou réaction prématurée.

Les vapeurs sont alors entraînées jusqu'à la zone de réaction par un flux gazeux assurant le rôle de gaz vecteur et de comburant. Elles sont alors décomposées au voisinage du substrat (plaque de silicium) placé à l'intérieur d'un four.

Un système de pompage maintient un vide de quelques torrs dans l'enceinte et assure l'évacuation des résidus de la réaction.

Les differentes caractéristiques des dépôts; vitesse de croissance, épaisseur, composition, morphologie et structure sont contrôlées par:

- la nature de la solution source (précurseurs, solvants, concentrations)
- la séquence d'injection (durée et fréquence d'ouverture de l'injecteur, pressuri-

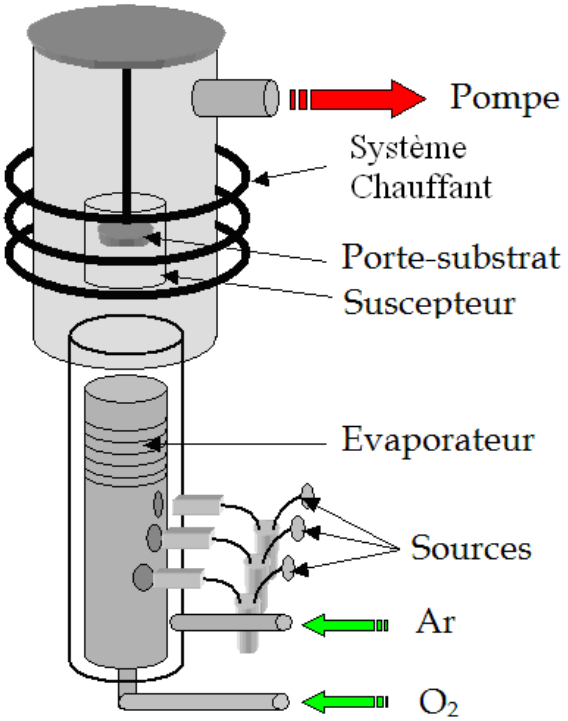

Figure 8: Zones d'évaporation et de décomposition de précurseur un système MOCVD à injection

sation du réservoir, nombre total d'injections)

- les températures du substrat et de l'évaporateur
- la pression totale dans l'enceinte
- la nature et le débit des gaz vecteur/actifs

Ces nombreux paramètres rendent cette technique très souple d'emploi. Cependant un grand nombre d'expériences est nécessaire pour les ajuster. Pour ce faire dans cette thèse, une étude d'optimisation a été nécessaire afin d'ajuster les differents parametres.

Le schéma de la machine que j'ai utilisée dans cette thèse pour dépôt de couche mince de $SrCu_2O_2$ est montré dans la figure 9 suivante.

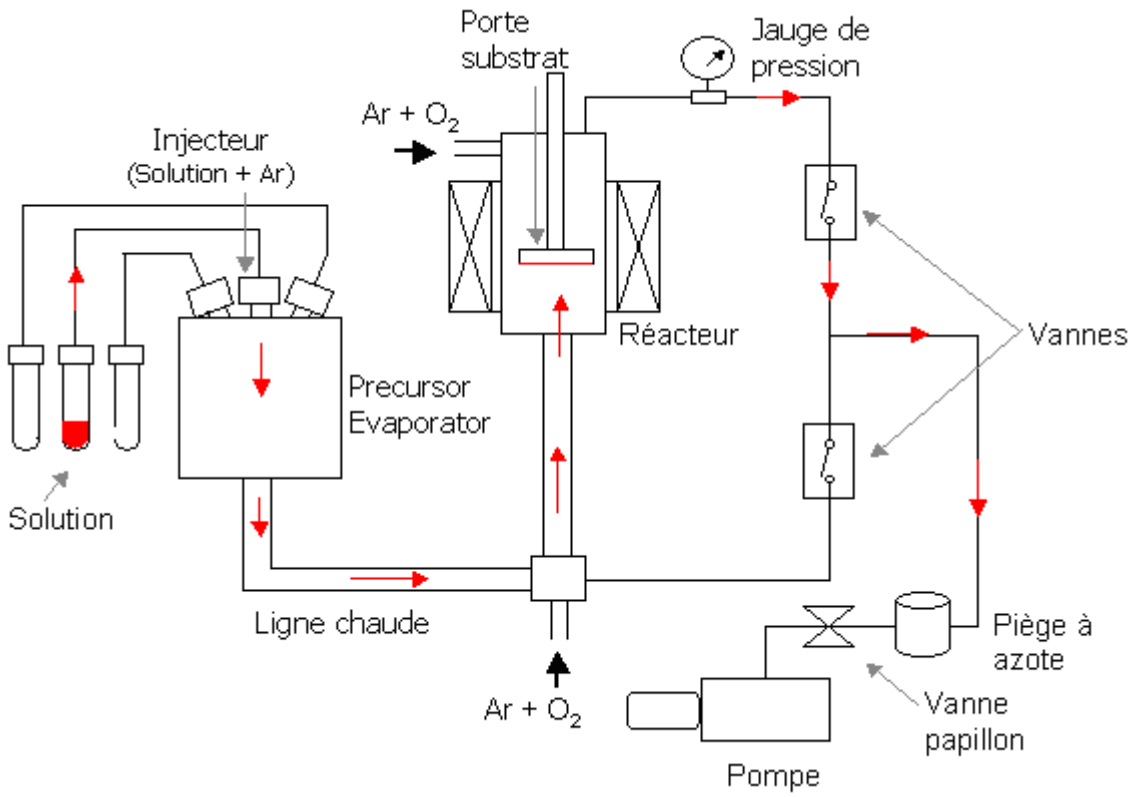

Figure 9: schéma de la machine MOCVD dans LMGP utilisé pour dépôt

La solution source est préparée par la dissolution de composés organométallique Tetraméthylheptanédate (tmhd) en poudre de Cu et de Sr comme composants principause et de Ba comme dopant dans un solvant organique, le meta-xylène. Le précurseur liquide est injecté par un injecteur dans une zone d'évaporation maintenu à haute température 280 °C pour obtenir l'évaporation en flash des gouttelettes de précurseur injecté. Les vapeurs de précurseur sont transportées par le gaz Ar de la zone d'évaporation à zone de réaction dans la ligne chaude. Le gaz O_2 est connecté avec la ligne chaude pour accompagner les vapeurs de précurseur jusqu'à la zone de réaction pour produire les dépôts d'oxydes sur le substrat. Le substrat est plac8'e sur le porte substrat dans la zone de réaction à une plus haute température appropriée (480-570 °C) pour la décomposition des vapeurs de précurseur. Lors du pompage les sous-produit de réaction

est accumulé dans un vase maintenu à très basse température par l'azote liquide.

0.7 Analyse des résultats

Il existe un très grand nombre de techniques de caractérisations differentes de couches minces. Ces techniques permettent de remonter aux proprietes structurales, thermiques, électriques, chimique, morphologiquee, optique, magnétique etc. Dans ce present travail, nous sommes intéressés par l'analyse des properietes chimique, morphologique, électrique et optique. L'analyse par Diffraction RX des couches minces brutes montre la coexistance des phases $SrCO_3$ et CuO pour la gamme des températures 480-570 °C de dépôt (figure 10). Les résultats ont été confirmés par spectrometrié Raman et IR. De plus la variation de la concentration en O_2 de 10% à 70% n'a pas permis d'obtenir $SrCu_2O_2$ directement.

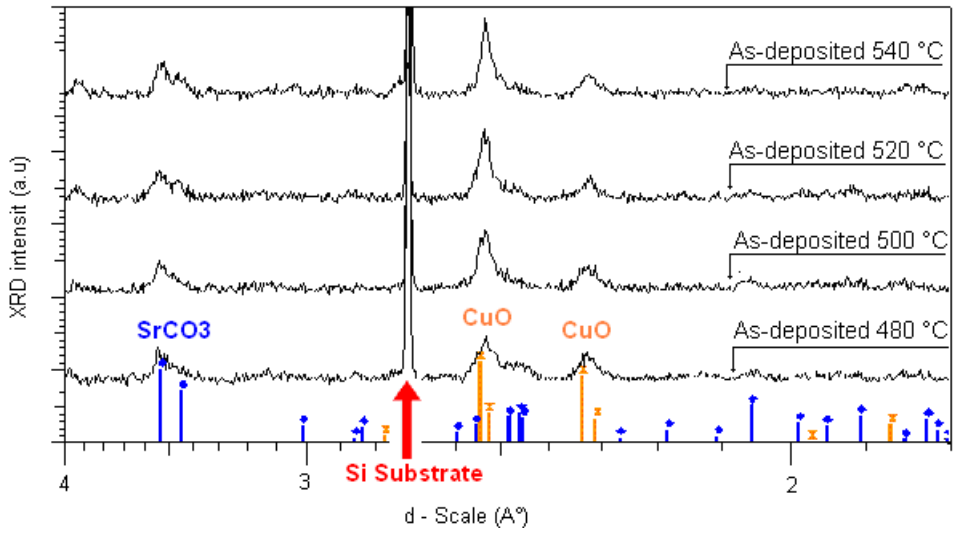

Figure 10: Spectres de diffraction RX de dépôts MOCVD sur silicium à différentes températures montrent que $SrCO_3$ et CuO sont des principaux composants des couches brutes

Aussi pour décomposer la phase $SrCO_3$, bien cristalliser le film, et obtenir la phase $SrCu_20_2$ (SCO) nous avons étudié different traitement thermique. Ainsi en premier lieu on a fait quelques étapes de recuit RTP sous le Ar à 600°C pour 30 seconds.

Le résultat de chaque étape de ce recuit est résumé dans la figure 11 par les spectres de diffraction RX.

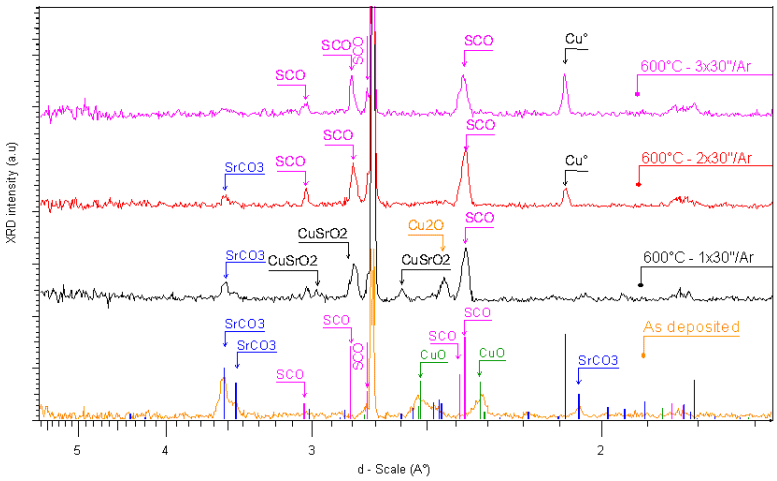

Figure 11: Spectres de diffraction RX de différents étapes de recuit RTP dans Ar pour 30 seonds à 600°C. Le troisième étape de recuit RTP produit SCO avec du Cu métallique

Bien que le recuit RTP sous Ar élimine $SrCO_3$ et produit SCO, cela donne aussi une grosse quantité de Cu métallique. L'obtention de Cu métallique peut être attribupremiere à environnement réduit d'oxygène pendant le recuit sous Ar et à la présence de carbone lié à la décomposition incompléte des précurseurs. Pour y reédier, nous avons realisé un recuit RTP en deux étapes. La première, sous oxygène permet d'éliminer completement $SrCO_3$ et de faire appraître la phase $Sr_{14}Cu_{24}O_{41}$. La deuxième étape, un recuit RTP sous Argon permet d'avoir SCO pure (figure 12).

L'ensemble des resultats trouvés par Diffraction RX sont confirmés par la spectroscopie Infrarouge à Transformée de Fourier (FTIR) dans la figure 13.

Le SCO peut être obtenu par un recuit conventionel en deux étapes (O_2 et Ar), mais cela n'est pas possible qu'après un refroidissement rapide dans Ar. L'effet de la vitesse de refroidissement est montré par spectrocopie Raman in-situ. Dans la première étape de recuit sous O_2, les pics de Raman à température ambiante de $SrCO_3$, CuO, et

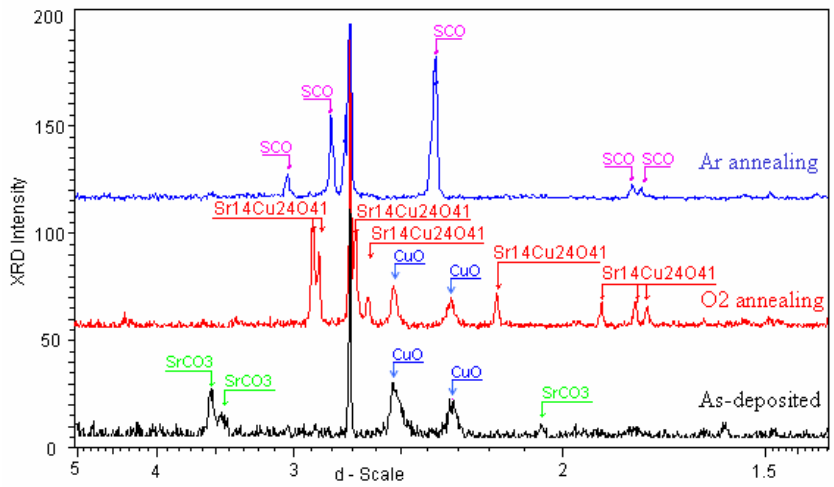

Figure 12: Analyse du recuit RTP en deux étapes (O_2 and Ar) par les spectres de diffraction RX. Le recuit du film brut sous O_2 pour 30 seconds à 600°C élimine $SrCO_3$ et produit $Sr_{14}Cu_{24}O_{41}$. La deuxième étape sous Ar donne SCO

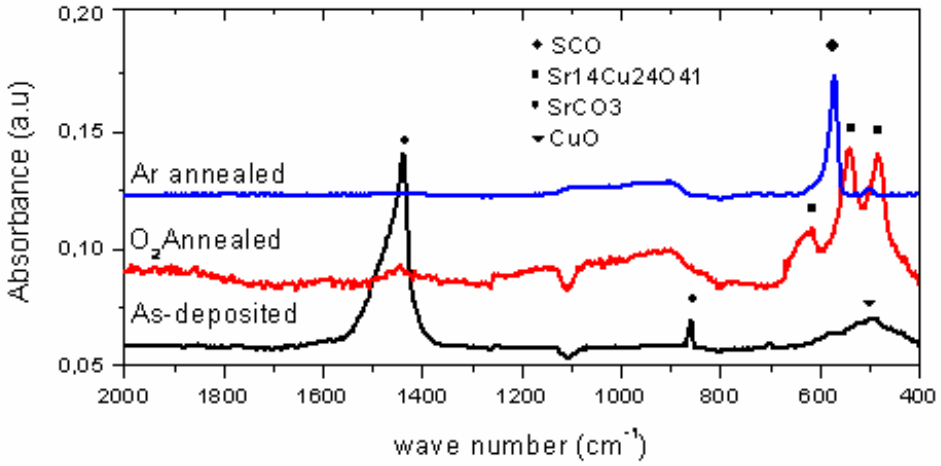

Figure 13: Analyse du recuit RTP en deux étapes (O_2 and Ar) par la spectroscopie FTIR. Le recuit du film brut sous O_2 pour 30 seconds à 600°C élimine $SrCO_3$ et produit $Sr_{14}Cu_{24}O_{41}$. La deuxième étape dans Ar donne SCO

Si diminuent avec l'augmentation de la température et disparaissent au délà de 550 °C. A 600 °C on trouve une nouvelle phase $Sr_{14}Cu_{24}O_{41}$. L'effet de la température sous O_2 sur les phases $SrCO_3$ et CuO, et le pic de substrat de Si est presenté dans la figure 14.

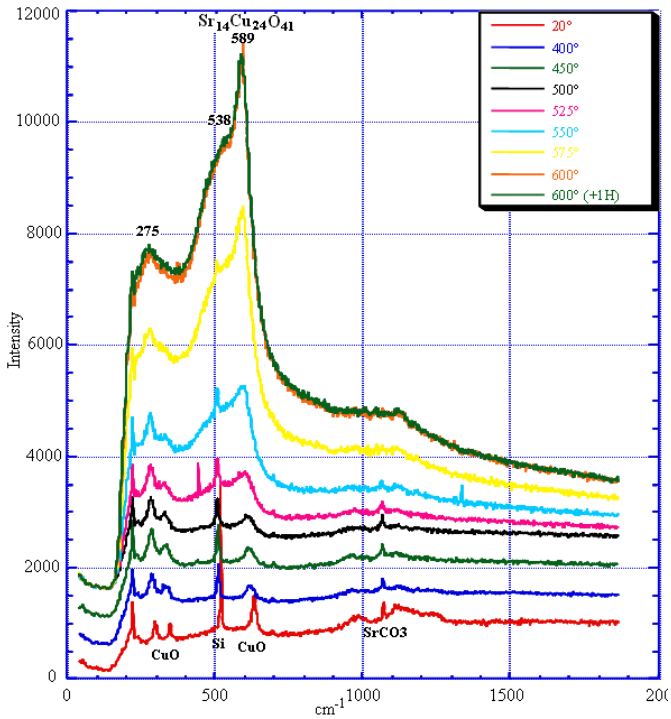

Figure 14: Effet de la température dans O_2 sur les phases $SrCO_3$ et CuO, et sur le pic de substrat de Si. Les pics de Raman pour CuO, Si, et $SrCO_3$ disparaissent et on trouve une nouvelle phase $Sr_{14}Cu_{24}O_{41}$ à 600 °C.

Le changement de gaz de recuit de l'oxygène à l'argon, permet l'obtention de la phase SCO à 600 °C. Par contre pendant le refroidissement à la température ambiante cette phase disparaître et donne naissance à la pahse $Sr_{14}Cu_{24}O_{41}$ (figure 15). Cette perte de la phase SCO pendant le refroidissement peut être attribuer à refroidissement lent.

Pour étudier l'effect de la vitesse de refroisdissement, nous avons realisé un recuit en deux étapes dans un four conventionel suivie d'un refroidissement lent ou rapide. Les couches traitées sont analysées par DRX (figure 16) et la phase SCO est obtenue seulement après un refroidissement rapide.

Nous avons également obtenu la phase SCO par le recuit conventionnel dans N_2 avec $SrCuO_2$ comme une phase intermédiaire (figure 17). La première étape de

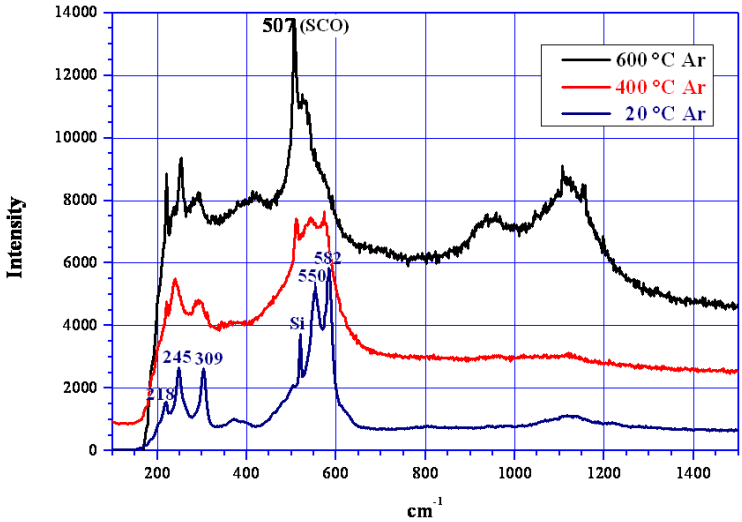

Figure 15: Inversion des phases pendant le refroidissement lent dans Ar

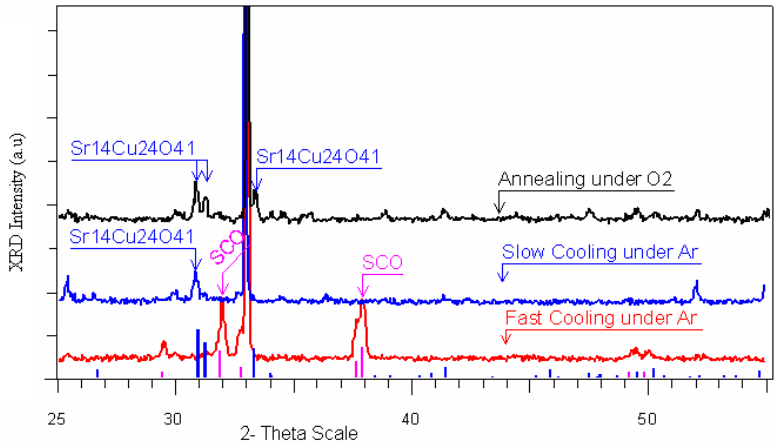

Figure 16: Perte de la phase SCO pendant le refroidissement lent à cause d'inversion entre SCO et $Sr_{14}Cu_{24}O_{41}$ et conservation de la phase SCO pendant le refroidissement vite

recuit dans N_2 à 600°C pour 2 heurs donne $SrCuO_2$ et la deuxième étape à la même conditions donne SCO.

On a appliqué la même conditions de recuit que de celle de la figure 17 pour obtenir la phase SCO sur substrat de verre. A partir de plusieurs traitements de recuit conventionnel on a trouvé que la durée de recuit est connecté avec la température de

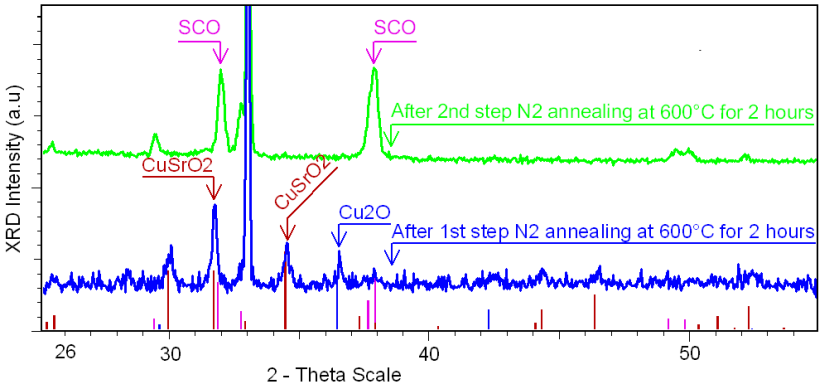

Figure 17: Recuit conventionnel dans N_2. La première étape de recuit dans N_2 à 600 °C pour 2 heurs donne $SrCuO_2$ et la deuxième étape à la même conditions donne SCO

recuit. C'est à dire que la durée de recuit est plus courte, si on augmente la température. Par exemple, le résultat dans figure 17 est obtenu sur le substrat de verre pour la durée de 3 et 5 minutes à 650 °C (figure 18)

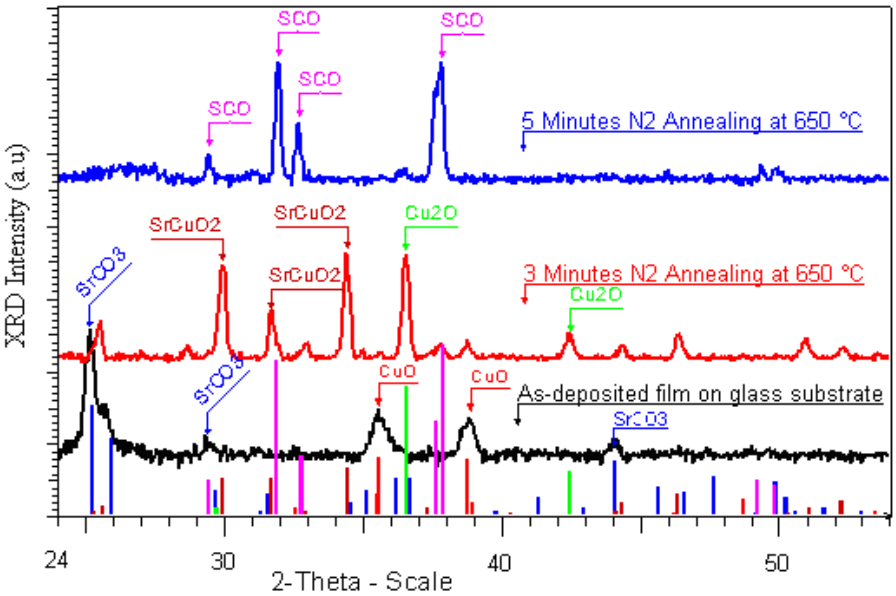

Figure 18: Analyse Diffraction RX de la phase de SCO sur le substrat de verre. La phase pure de SCO sur le substrat verre se développe pendant 5 minutes de recuit conventionnel dans N_2 avec $SrCuO_2$ comme une phase intermédiaire qui se développe pendant 3 minutes.

La transparence optique et la conductivité électrique dépendent de la pureté de phase SCO et de la morphologie de la couche mince. Par exemple, la contamination de Cu_2O augmente la conductivité de couche mince de SCO, mais diminue en même temps la transparence. D'un autre côté, les fissures qui se développent dans la couche mince de SCO pendant le recuit, diminue la conductivité ainsi que la transparence. La taille de fissures peut être réduite par un échauffement rapide et par un recuit de durée courte. L'effet la durée de recuit et le vitesse de d'échauffement sur la morphologie est montrée dans la figure 19 suivante.

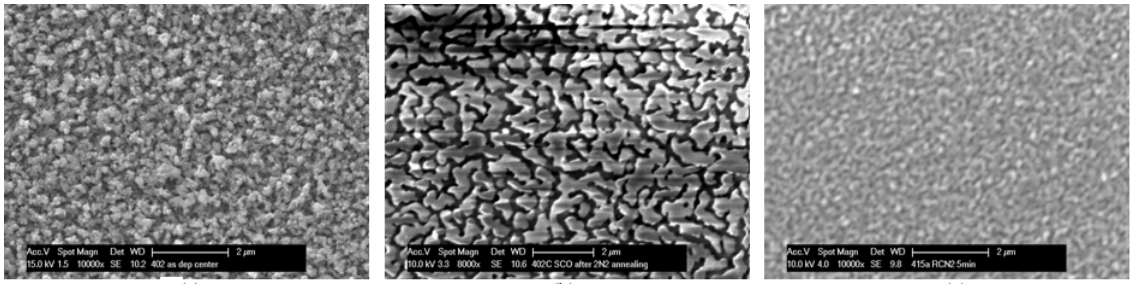

Figure 19: L'effet de la durée de recuit et le vitesse d'échauffement sur la morphologie. (a) La morphologie de couche brute, (b) morphologie de couche après le recuit de 4 heurs avec le réchauffement lent, (c) morphologie de couche après le recuit de 5 minutes avec un échauffement rapide.

On peut voire des fissures de grande taille dans la couche mince recuit avec un échauffement lent pour durée longue de 4 heures. Par contre, la couche mince recuit avec un échauffement rapide pour une durée courte de 5 minutes n'a pas plus de fissures.

La mesure de la transparence en pourcentage correspondant aux échantillons des images de la figure 19 est montrée dans la figure 20.

Le valeur de la transparce en pourcentage du substrat de verre et de la couche mince de SCO avec et sans substrat est donné dans la figure 21. La figure 21 montre une transparence de 75% à 550 nm dans la gamme visible.

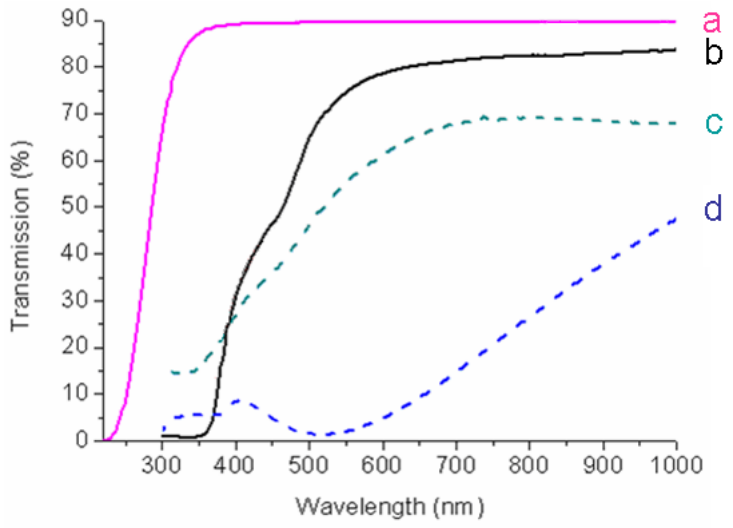

Figure 20: (a) la transparence du substrat de verre, (b) la transparence de la couche mince SCO corresponde à image 19-c, (c) la transparence de la couche brute corresponde à image 19-a, (d) la transparence de la couche mince SCO corresponde à image 19-b

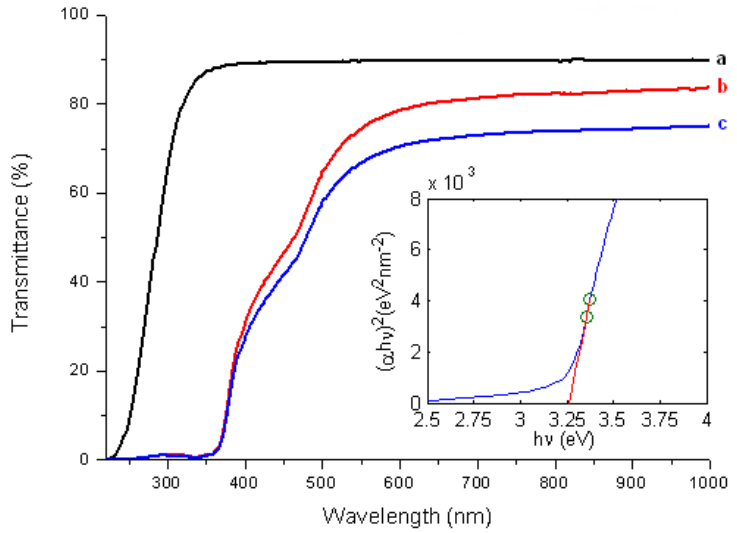

Figure 21: La Transparence en pourcentage de (a) substrat de verre, (b) couche mince de SCO sans substrat, et (c) couche mince de SCO avec substrat. L'insert est une trace de $(\alpha h\nu)^2$ et de lénergie de photon incident $h\nu$ pour calculer le gap de bande

L'absorption optique qui correspond à l'excitation des électrons de la bande de valence à la bande de conduction peut être utilisé pour déterminer la nature et la valeur

de gap. La relation entre les coefficients d'absorption (α) et l'énergie de photon ($h\nu$) incident pour le gap de bande direct est

$$(\alpha h\nu)^{1/2} = A(h\nu - E_g)$$

où A est une constante, E_g est la valeur du gap du matériau. Un tracé entre $(\alpha h\nu)^2$ et $h\nu$ est montré dans l'insert de la figure 21. Le valeur du gap 3,26 eV est calculée par interception sur l'axe d'énergie.

La conductivité électronique pour une dizaine d'échantillons a été mesurée par quatre poits ou par le methode de Van der Pauw, la plus haute conductivité que on a trouvé est 4.26x10^{-2} Scm^{-1}.

1

Introduction - Context and Background

1.1 Introduction

EVERY solid object has a surface, this surface is the discontinuity in the properties of the bulk materials and has been the target of modifications (artistic decoration and/or functional improvement) since the earliest times of mankind [19].

Today, modern products offer even more new functions with the unusual properties that often cannot be found in bulk sample. These product materials open completely new areas of applications. The multifunctionality of these technical products especially concerns their surface properties. Surface coating of glass with different types of films is one of the technologies that occupy a key position in the material and product development. Transparent Conducting Oxide (TCO) thin films are deposited on transparent substrates to form transparent electrodes [19]. Transparent electrodes is the key component of a variety cutting-edge applications, such as solar cells, gas sensors, organic light-emitting diodes, liquid crystal displays, electrochromic smart windows, as well as architectural coatings. All TCOs can be classified into two major classes; the p-type and the n-type, on the basis of their majority charge carriers. However, the n-type TCOs are the most readily available and therefore more commonly

found in practical applications. Major use of these n-type TCOs are in the transparent electrodes. Their applications for transparent electronics are rather restricted. The lack of p-type TCOs prevent fabrication of transparent p-n junction composed of transparent semiconductors.

Fabrication of p-type TCOs with high optoelectrical properties is, indeed, still a challenge. In comparison to the research in n-type TCOs, little work has been done on the development of p-type TCOs. The effective p-type doping in the TCOs is often compensated due to their intrinsic oxide structural tolerance to oxygen vacancies and metal interstitials. Recently, significant development have been reported about p-type TCOs. Among these p-type TCOs reported so far, $SrCu_2O_2$ (SCO) is considered to be one of the most promising. Advancements in p-type TCO materials development are still in a growth stage. Although the conductivity of the p-type oxide semiconductors is still lower than their n-type counter parts, the p-type TCOs offer the potential for a variety of new devices [20].

Currently there is a large amount of enthusiasm in the search for a p-type TCO. This PhD research work is an effort to search for efficient p-type TCOs in the framework of a European project Novel Advanced Transparent Conducting Oxides (NATCO). For p-type TCOs, Cu_2O derived materials are currently the leading candidates. Based on the previously published reports and on the theoretical calculations by the NATCO partners, we opted for SCO as our target material for p-type TCO in this PhD research work. We successfully deposited SCO thin film on various substrates by Metal Organic Chemical Vapor Deposition (MOCVD) technique followed by some post-deposition annealing processes.

1.2 Context and Background

NiO was the first p-type TCO reported by H. Sato et al. in 1993. In 1997, H. Kawazoe et al. reported $CuAlO_2$ as another p-type TCO with considerable improvement over NiO. This triggered the development of a series of p-type TCOs. And in the subsequent year, $SrCu_2O_2$ with the optoelectrical properties superior than $CuAlO_2$ was reported by Kudo et al. The primary advantage of SCO ($SrCu_2O_2$) over the previously reported p-type TCOs is its large direct bandgap and the possibility of its deposition at low temperature. The undoped SCO has lower conductivity in comparison to the K-doped, reported by Kudo et al., and Ca-doped, reported by Sheng et al. using Pulsed Laser Deposition (PLD) techniques. However, the optoelectrical properties of these doped SCOs were still inferior to commercially available n-type TCOs. Since the properties of thin films also varies with the change in deposition techniques, therefore, in addition to efficient SCO doping, various deposition techniques like sol-gel by Roy et al., e-beam evaporation by Bobeiko et al., and RF-magnetron sputtering by Nakamura et al. etc, were employed to synthesize thin film of better performance. In this context, we opted for the MOCVD as a deposition technique and Ba as a doping material in order to enhance the previously reported optoelectronic properties of SCO.

1.3 Thesis Organization

In addition to the first chapter which gives a brief introduction of thin films, their utility, and of TCOs as a special class of thin films with the importance of p-type TCOs. The second chapter of this six chapter thesis is devoted to a detailed discussion on TCO thin film ranging from its theoretical perspectives to technological applications, from historical emergence to the present applications and future opportunities, and importance of p-type TCOs and their limitations. The third chapter throws light on thin film experimental techniques both for deposition and analysis. The fourth chapter

named as “material and methods” is devoted to the theoretical details and practical implications of the available equipments in Laboratoire des Matériaux et du Génie Physique (LMGP) used in thesis work for the synthesis and characterization of SCO thin films. In chapter five, we discuss in details all the significant experimental results we obtained during these three years of PhD research work. Conclusion and future perspectives of this work are described in the chapter six.

2

Transparent Conducting Oxides (TCOs)

THE basic Electromagnetic Theory (Maxwell's equations) does not permit a material to be both electrically conducting and optically transparent simultaneously. Optically transparent materials tend to be electrical insulators by virtue of their large bandgaps (>3.1 eV). However, Transparent Conductive Oxides (TCOs) is a group of materials with unique physical properties. Despite their large bandgaps (>3.1 eV), the TCOs show electrical conductivity of the order of 10^4 S cm^{-1}.

Transparent conducting oxides have been known for a century. However, the technological and commercial use of TCO thin films has been emerged for half a century. In general, the TCO thin films in practical use as transparent electrodes are reported to exhibit conductivity of the order of 10^4 S cm^{-1} and an average transmittance above 80% in the visible range. The TCO semiconductors suitable for transparent electrodes should have a carrier concentration of the order of 10^{20} cm^{-3} or higher and bandgap energy approximately above 3.1 eV; i.e., degenerate n-type or p-type semiconductors. The most widely used TCO for optoelectronic device applications has been indium tin oxide (ITO). However, ITO has some limitations due to the rarity and high price of indium and the fact that it is too brittle to be used on flexible substrates. It also requires high deposition temperature thus limiting the choice of its substrates.

Today, the area of practical use of TCO has been broadened and the commercial demand for less expansive, more flexible and environmentally friendly TCOs continues to stimulate further research.

2.1 TCO Theory

All well-known and widely used TCO materials show similar electric properties and carrier generation mechanisms [21]. The electron-gas model of solids can equally be applied to TCOs as well. Within the Boltzmann formulation, the electrical conductivity of such materials is given by $\sigma = ne\mu$ where n is the density of free carriers, μ is their mobility and e is the electronic charge. It is possible to establish a materials 'sorting map' of electrical conductors within an '$n - \mu$' diagram, as given in Figure 2.1.

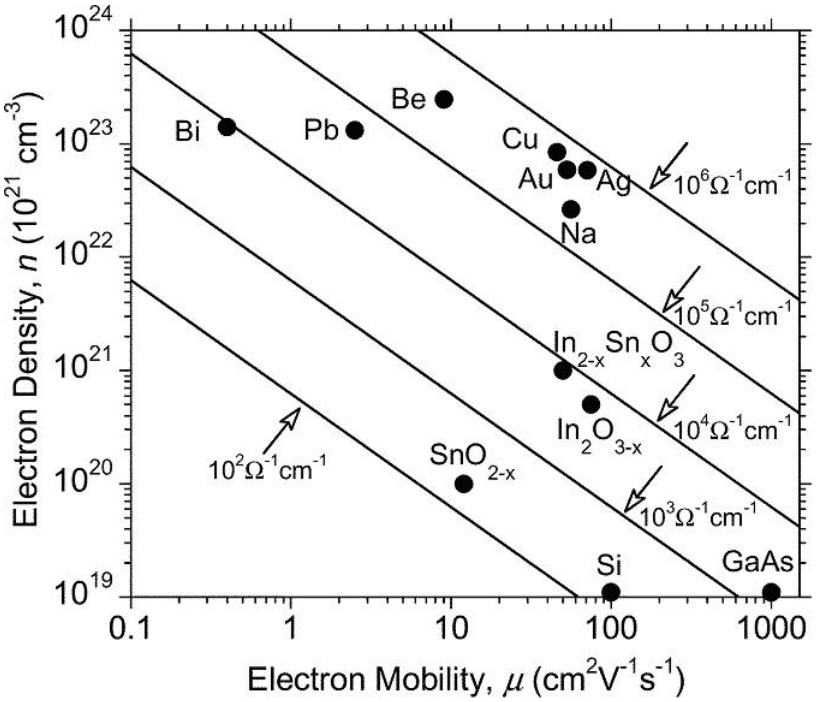

Figure 2.1: Sorting map of the materials (metals, semimetals, semiconductors) on the basis of conductivity in '$n - \mu$' correlation (electron carrier density n and electron mobility μ). The diagonal straight lines are the lines of constant conductivity [5]

In Figure 2.1 the diagonal straight lines are the lines of constant conductivity. The semimetals lie on the top-left, metals are in the upper-middle and the conventional semiconductors are in the bottom-right. As a particular class of materials the "Transparent Conducting Oxides" exhibit intermediate characteristics between highly conducting/reflecting elemental metals and low-carrier density/high mobility conventional semiconductors [5].

Charge carriers in these oxides arise from three fundamental sources: interstitial metal ion impurities, oxygen vacancies and doping ions. When an oxygen vacancy is present in the lattice it acts as a doubly-charged electron donor while the interstitial metal ions impurities as electrons acceptor. The high conductivity of TCO is related to the presence of these shallow donors or impurity states located closed to the host conduction band via chemical doping or by the presence of oxygen vacancy impurity states [5, 22–24].

Dopant ionization within the TCO occurs in the same way as in other semiconductor crystals. Shallow donors near the conduction band (n-type) allow electrons to be thermally excited into the conduction band, while acceptors near the valence band (p-type) allow electrons to jump from the valence band to the acceptor level, populating the valence band with holes [5]. Upon further doping a degenerate semiconducting system is created which gives rise to high conductivity along with good optical transparency as the fundamental host bandgap remains intact, i.e., an electrically conductive material remains optically transparent [5, 23, 25].

It is important to note that charge carrier scattering in these oxides arises primarily from ionized impurity scattering. Charged impurity ions and point defects have scattering cross-sections that are much greater than their neutral counterparts. Other scattering mechanisms such as scattering of electrons by phonons in pure single crystals and the grain boundary scattering in polycrystalline films also take place in

TCOs [26]. Increase in scattering decreases the mean-free path of the charge carriers, which leads to poor device performance and high resistivity.

These materials can be modeled reasonably well by the free electron gas theory assuming a parabolic conduction band and doping levels above the Mott Criterion. This criterion states that an insulator such as an oxide can experience a composition-induced transition to a metallic state given a minimum doping concentration n_c, determined by:

$$n_c^{1/3} a_H^* = 0.26 \pm 0.05$$

Where a_H^* is the mean ground state Bohr radius. For ITO this value requires a minimum doping concentration of roughly 10^{19} cm^{-3}. Above this level, the typically-electrically insulating material becomes metallic and is capable of allowing carrier flow [5].

2.2 Historical Background

The history of TCO starts from 1907, with the discovery of Cadmium Oxide (CdO) thin film by a German scientist Karl Baedeker [27]. Due to small bandgap, transparency of CdO was too low to be used for practical applications. The practical use of TCO started with discovery of tin-doped In_2O_3 in 1954 by G. Rupprecht [28]. In 1960s, it was recognized that thin films composed of binary compounds such as ZnO, SnO_2, In_2O_3 and their alloys were also TCOs [29]. In addition to binary compounds, the ternary compounds such as Cd_2SnO_4, $CdSnO_3$ and $CdIn_2O_4$ were developed as TCO materials prior to 1980. In 1980s, impurity-doped ZnO such as ZnO:Al and ZnO:Ga along with abundant of binary compounds were developed. In 1990s, new TCO materials consisting of multicomponent oxides, like combination of ZnO, CdO, In_2O_3 and SnO_2, have been developed [23]. Among all these TCO materials the tin-doped indium oxide commonly known as indium tin oxide (ITO) offers the

best available performance in terms of electrical conductivity and optical transparency along with excellent environmental stability, reproducibility and good surface morphology [30]. However, due to rarity and high price of indium the ITO cannot remain in continuous commercial use for device application [22, 31]. All the TCOs mentioned above are just some of the TCO materials reported so far. All these TCOs have electrons as majority charge carriers and hence known as n-type TCOs. There was no p-type TCO reported until 1993, when H. Satu and his co-workers reported NiO as p-type TCO [32]. The second report on $CuAlO_2$ as a p-type TCO was published in 1997, by H. Kawazoe et al., with considerable improvements over NiO [33]. This opened the development of a series of p-type TCOs [34]. However, until now no efficient p-type TCO having optoelectrical properties comparable to its n-type counterpart is available. If there would be an efficient p-type TCO, it can be used as alternative to ITO along with the fabrication of transparent pn-junction which will lead to a new generation of electronics known as "transparent electronics".

2.3 Structure Mechanism for TCO

A pivotal requirement for the continued and expanded applications of transparent conductors is the better understanding of the fundamental relationships between conductivity and transparency. It is crucial to better understand the origin of the carriers in the TCOs and the dominant scattering mechanism limiting performance, especially in the critical area of mobility of the carriers [35]. The applications of TCOs is based on the fact that the electronic bandgap of a TCO should be higher than 3.1 eV, so that a visible photons (having energy between 2.1 and 3.1 eV) cannot excite electrons from valence band (VB) to the conduction band (CB) and hence are transmitted through it, whereas they have enough energy to excite electrons from donor level to CB (for n-type TCO) or holes from acceptor level to VB (for p-type TCO) as described in Figure 2.2 [6].

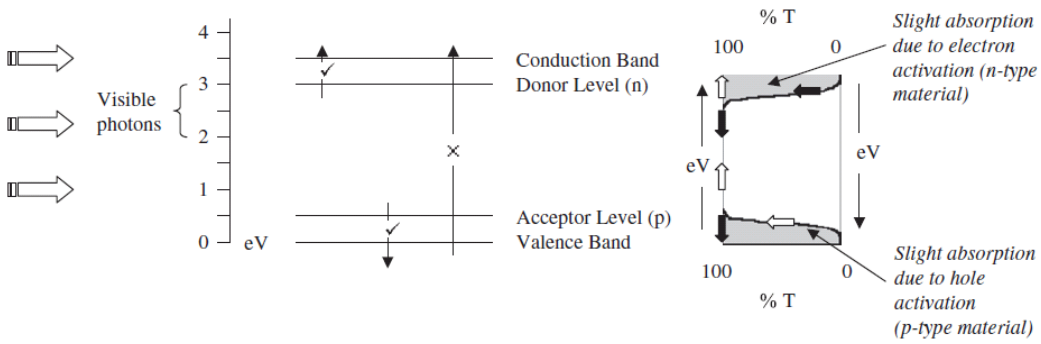

Figure 2.2: Bandgap designing for transparent conductors. Visible photons (2.1-3.1 eV) do not have enough energy to excite electrons from valence band to conduction band, but have sufficient energy to excite holes (for p-type) from acceptor level to VB or electrons (for n-type) from donor level to CB [6]

The first-principles band-structure techniques are used to understand how doping and carrier generation alter the band structure of transparent conductors. Figure 2.3 gives the calculated band structures of undoped and Sn-doped In_2O_3, illustrating the essential features of transparent conductivity, that is, a highly dispersed single s band at the bottom of the conduction band, which explains the well-known Burstein-Moss (B-M) shift (i.e., increase in bandgap with carrier doping) [36].

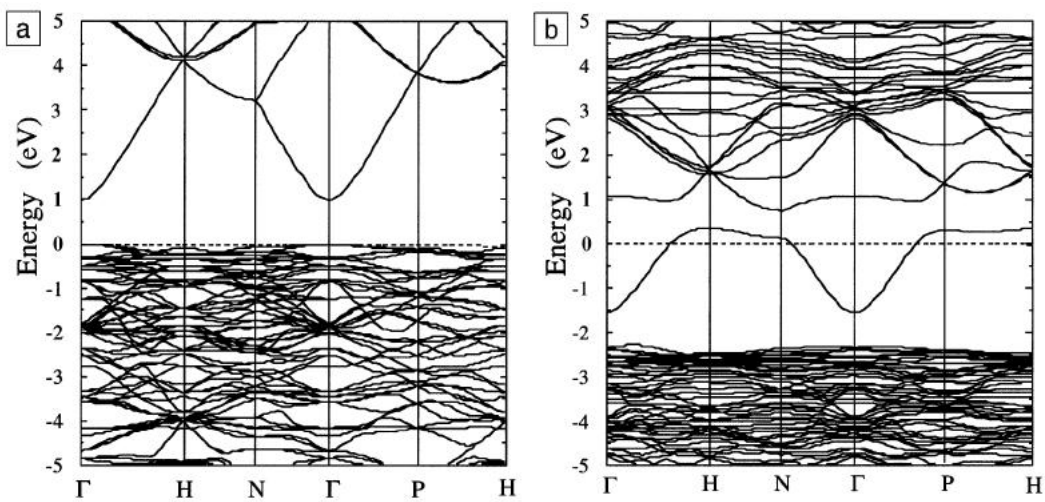

Figure 2.3: Electronic band structures calculated for (a) undoped and (b) Sn-doped indium oxide. The Sn-doped Indium Oxide shows large bandgap and dispersed single s band the bottom of conduction band owing to high transparency and conductivity in comparison to undoped indium oxide

The high dispersion and s-type character of this band also explain the high conductivity due to the high mobility of these states and result in a rather uniform distribution of their electron charge density and hence their relatively low scattering [36].

On the basis of these calculated band structures the formulated conditions for transparent conducting behavior are: (1) a highly dispersed single s band at the bottom of the conduction band, (2) separation of this band from the valence band by a fundamental bandgap large enough to exclude interband transitions in the visible range, and (3) band properties such that the plasma frequency is below the visible range [36].

2.4 Criteria for choosing TCOs

For each application, the most suitable TCO is the one that shows good electrical conductivity along with good optical transparency [35]. The physical, chemical, and thermal durability, etchability, plasma wavelength, work function, thickness, deposition temperature, toxicity, and cost are other factors that may also influence the choice of transparent conducting material for any particular application [26].

Transparent and electrically conductive thin films have been prepared from a wide variety of materials. These include: oxides of tin, indium, zinc, gallium, cadmium, silver, gold, and copper etc [26]. The existing TCO materials have limitations in one way or the other. For example, the limited use of ITO in flexible electronics is due to the brittleness of ITO thin films [37–39]. Least development of the "transparent electronics" is due to the unavailability of efficient p-type TCO materials [3, 6, 35, 40].

High transparency (>85%) combined with useful electrical conductivity (>10^3 S cm^{-1}) is achieved by selecting a wide bandgap oxides through the introduction of suitable dopants [30, 41].

Parameters	Transparent Conductive Materials
Band gap	>3.1eV (380nm)
Transparency at 550nm	>90% (for n-type) and >85% (for p-type)
Resistivity	$10^{-4}\Omega$ cm (for n-type) and $10^{-3}\Omega$ cm (for p-type)
Carrier Concentration	>10^{20}cm^{-3} (for n-type) and >10^{18}cm^{-3} (for p-type)
Mobility	>40cm^2(V s)$^{-1}$(for n-type) and >20cm^2(V s)$^{-1}$ (for p-type)
Sheet resistance	$\leq$ 10kΩ /square (for 20nm thickness)

Table 2.1: Minimum required properties of TCOs

2.5 TCO Relevant Properties

It might be reasonable to ask which TCO is the best. However, this question does not have a unique answer, since different TCOs are best suited for different applications [26]. In general, a TCO must exhibit three important qualities: high optical transparency, good electrical conductivity and mechanical durability including flexibility [42]. The properties of a TCO depend not only on its chemical composition, but also on the method used for its preparation [26]. Some of the most relevant properties of a TCO are:

2.5.1 Optical and electrical performance

Besides high conductivity an efficient TCO thin film should have a very low absorption coefficient in the near-ultraviolet (NUV), visible (VIS) and near-infrared (NIR) region. The transmission in the NUV is limited by the bandgap energy E_g, as photons with energy larger than E_g are absorbed by raising electron from the valence band to conduction band. A second transmission edge exists at the NIR region, mainly due to reflection at plasma frequency. Ideally, a wide band gap TCO should not absorb photons in the NUV-VIS-NIR region. However, there is no "ideal" TCOs thin film, and even if such film could be deposited, reflection and interference would also affect the transmission. Hence, 100% transparency over a wide region cannot be obtained [43].

The optical properties such as transmission (T), reflection (R), and absorption (A), are determined by its refractive index (n), extinction coefficient (k), band gap energy (E_g) and geometry. Geometry includes film thickness, thickness uniformity and film surface roughness. The T, R and A are intrinsic, depending on the chemical composition and solid structure of the material, whereas the geometry is extrinsic. There exists a negative correlation between the carrier density and the position of the IR absorption edge due to plasma frequency reflection, but positive correlation between the carrier density and the UV absorption edge, as E_g increases at larger carrier density (Moss-Burstein effect). As a result, the TCO transmission boundaries and conductivity are interconnected [43].

An effective TCO should have high electrical conductivity combined with low absorption of visible light. Thus an appropriate quantitative measure of the performance of a TCO is the ratio of the electrical conductivity σ to the visible absorption coefficient α, given as

$$\sigma/\alpha = -\left\{R_s \ln(T+R)\right\}^{-1}$$

in which R_s is the sheet resistance in ohms per square, T is the total visible transmittance and R is the total visible reflectance. The σ/α is known as figure of merit and its larger value indicates the best performance of a TCO. Since σ and α depends on crystallite grain size which increases with the film thickness, hence the figure of merit σ/α depends somewhat on film thickness [26, 44, 45]. An epitaxial film has a larger value of "figure of merit", as the grain boundaries in case of polycrystalline film increase both electrical and optical scattering resulting in high resistivity and high absorption of light [46–48]. The deposition temperature and choice of suitable substrate are the key parameters that control the epitaxial nature of the films [49, 50]. According to the data published in the MRS Bulletin of August 2000, the fluorine-doped ZnO and the cadmium stannate Cd_2SnO_4 have the highest values of figure of merit [26].

2.5.1.1 Electrical Conductivity

TCOs are wide bandgap semiconducting oxides, with conductivity in the range $10^{-9} - 10^{5}$ Scm^{-1} [9, 51, 52]. TCOs may be n or p-type semiconductors depending upon their charge carrier generation mechanism. The conductivity of n-type TCOs is always higher than that of p-type due to relative small effective mass of electron in conduction band than that of hole in the valence band [9].In order to obtain a material with high electrical conductivity; high carrier concentration and mobility are essential [53]. For wide bandgap semiconductors the charge carriers concentration is determined by the maximum number of electronically active dopant atoms that can be placed in the lattice. However, attempt to place a larger number of dopant atoms in the lattice decreases the mobility due to increase in charge carriers scattering by ionized dopant atoms [26]. For charge carriers to be highly mobile, the conduction band (CB) should be wide enough i.e., a dispersed CB and such dispersed CB is obtained by a symmetric anion coordination environment which give rise to covalent bonding [54]. The mobility also depends on crystallographic structure. Polycrystalline films have lower mobility due to grain boundary scattering. An epitaxially grown film of ITO on YSZ (Yttrium-stabilized Zirconia) substrate has much more higher mobility than the same ITO grown film on silica substrate [46, 51, 55]. The obtainable electrical properties are strongly dependent on deposition methods as well as on the deposition conditions [22], for example decrease in electrical conductivity of Ca-doped SCO was observed as a result of increase in substrate temperature [56]. While increase in thickness of the film improves conductivity [26].

2.5.1.2 Optical Transparency

The optical bandgap widening or shrinkage is generally attributed to the doping level. The optical bandgap widening is due to the optical band filling effect above the critical Mott carrier density: a well-know Burstein-Moss effect. This effect is usu-

ally attributed to the occupation of conduction band, inducing optical transitions at energies higher than the fundamental electronic gap. The optical shrinkage is due to electron-electron interaction and higher carrier concentration i.e., in this case, donor level approaches the conduction band [57–60]. The low optical absorption observed in the films can be reconciled with the high dc conductivity according to the recent electrical transport theories of wide band gap semiconductors [57]. For a material to be transparent, not only a wide fundamental bandgap is important, but there should be no visible light transition between occupied-unoccupied states inside CB and VB [8, 61]. The optical properties of a TCO thin film not only depend on the film itself but on the optical properties of the substrate as well. The thickness of the TCOs film also plays an important role in determining its optical properties; thinner films improve transparency by avoiding interference effect while increasing its sheet resistance [62]. In the past few years, improvement of the optical properties has been a dominating factor in increasing the commercial quality of opto-electronic devices [57, 59]. As a result of studies, it was observed that due to the increment in substrate temperature the optical transmission, low absorption, anti-reflection and required low intense photoluminescence properties were improved for ZnO thin films [57]. However, the increase in substrate temperature reduces the durability of transparent electrodes and causes thermal shrinkage to glass, ceramics, polythene tereph-thalate (PET) and polypropylene substrates [42].

2.5.2 Plasma Frequency

The plasma frequency being a function of carrier concentration is of key importance in calculating the transparency and reflectivity of TCOs [63]. Plasma frequency is the frequency of periodic oscillations of charge density in conducting media [64]. If the incident light has frequency higher than the plasma frequency of the material, the free charges cannot respond to the incident light and the material behaves as a transpar-

ent dielectric [26]. However, at frequencies below the plasma frequency, the materials reflect and absorb incident light [26]. For most TCO materials, the plasma frequency falls in the near-infrared part of the spectrum, that is why, the TCOs show good transparency to the visible light [26]. In most metals, the plasma frequency is in the ultraviolet region, making them shiny (highly reflecting) in the visible range [65, 66]. The plasma frequency increases approximately with the square root of the conduction-electron concentration [63]. Thus larger value of doping concentration increases the plasma frequency thereby reducing the wavelength range of transparency while increasing the electrical conductivity and vice versa.

2.5.3 Other relevant factors

Apart from the aforementioned important factors, there are some other relevant factors as well, such as: Work Function (the minimum energy required to remove an electron from conduction band to vacuum), Thermal Stability (a certain high temperature range within which TCOs shows stable resistivity, this temperature is slightly above the optimized deposition temperature), Deposition Temperature (plays a key role in case of flexible and thermally sensitive substrates), Diffusion Barrier between film and substrate (to avoid the diffusion of substrate materials into films and vice versa at high deposition temperatures and post-deposition thermal processes), Etching (easy etching of TCO thin films is favored in some applications), Chemical Durability (the ability of TCOs to withstand corrosive chemical environment), Mechanical Hardness (resistance to scratches), Production Cost (including cost of the raw materials and preparation process) and Toxicity (additional encapsulating need as a shield for TCOs using toxic element to protect the escape of toxic materials into the environment), etc [26].

2.6 TCO's Applications

TCOs have a wide variety of industrial and commercial applications. Their ability to reflect thermal infrared heat is exploited to make energy-conserving windows. These low emissivity windows are the largest area of current use for TCOs. Oven windows employ TCOs to conserve energy and to maintain an outside temperature that makes them safe to touch. Microwaves windows are coated with TCO which allows visible light to pass and block microwaves so as to protect eyes. TCOs are commonly applied to architectural glass in house windows to transmit visible light and reflect infra-red light, this feature is used to minimize the heating cost in winter and air-conditioning cost in summer. The electrical conductivity of TCOs is exploited in front-surface electrodes for Solar Cells and flat-panel displays. Automatically dimming rear-view mirrors for automobiles and electrically controlled "Smart Windows" use TCO thin films. Electric current is passed through TCOs to defrost windows of vehicles and to keep the deep cases of freezers frost-free. Their advantage over traditional hot air blowers is that they can have a much shorter effective defrosting and work uniformly over large areas. TCOs dissipate static electricity from the windows on xerographic copiers. Glass touch-control panels are etched from TCOs layers. TCOs can also be formed into transparent electromagnetic shields, invisible security circuits on windows and transparent radio antennas built into automobile windows [26].

The present applications are based on n-type TCOs. How many more applications would emerge with the development of active "transparent electronics"? The answer to this question will depend to a large extent on the availability of p-type TCOs having opto-electric properties comparable to those of n-type TCOs. Thus, the high-performance invisible transistor reported by Nomura et al. (2003) represents an important milestone in the development of transparent electronics [67]. The future applications of TCOs include holographic recording media, high-refractive index waveguide

overlays for sensors and telecommunication applications, write once read-many-times memory chips (WORM), electronic ink etc [6].

2.7 Types of TCOs

On the basis of majority charge carriers all TCOs can be classified into groups; n-type or p-type. The n-type conductivity of TCOs results from Oxygen-vacancies, interstitial metal ions impurities due to some intrinsic or extrinsic defects and n-type doping ions, while the p-type conductivity is due to oxygen-excess, interstitial metal ions vacancies and p-type doping. while the p-type conductivity arise from Oxygen-excess due to some intrinsic or extrinsic material defects [9]. Defects which result in good p-type conductivity should possess single particle levels near the valence band maximum (VBM) which result in p-type conductivity through hole-hopping, while successful n-type conductivity requires the relevant defects to have electron donor levels near conduction band minimum (CBM) [9]. Technological applications of TCOs depend critically on the ability to dope them. A given material is difficult to be doped n-type if the CBM is too high, likewise a p-type doping is difficult if VBM is too low. A wide bandgap transparent material cannot be doped both p-type and n-type [68].

2.7.1 N-type TCOs

An n-type TCO is one in which the majority charge carriers are the negatively charged electrons. Most of the known TCOs are n-type and therefore are most commonly found in practical applications [10]. The presence of extrinsic donors generate free electrons resulting in n-type conductivity [24]. Historically, most research to develop TCO thin films as transparent electrodes has been conducted using n-type semiconductors [22]. The most efficient n-type TCO is the ITO due to its superior electrical and optical properties [53]. There is a continued increase in its demand for the commercial use which is resulting in increase in its price and also jeopardiz-

ing its availability in the near future. Efforts are on the way for the development of alternative TCO materials to resolve this serious problem [22]. At present, resistivities of 2-3x$10^{-4}\Omega\mathrm{cm}$ and an average transmittance above 85% in the visible range is obtained in Aluminium-Zinc-Oxide (AZO) and Gallium-Zinc-Oxide (GZO) [22]. Historically, TCO materials were developed using binary compounds such as SnO_2 and In_2O_3 and subsequently ternary compounds such as Cd_2SnO_4, $CdSnO_3$ and $CdIn_2O_4$. Recently, multicomponent oxides have been attracting much attention as new TCO materials [23].

2.7.2 P-type TCOs

The n-type TCOs are playing their role very well, however, their applications are limited to transparent electrodes in flat panel displays and solar cells [69]. Now for diverse device applications, it is of the utmost importance to prepare various new p-type TCOs with superior optical and electrical properties, at least comparable to the existing widely used n-type TCOs [6]. In p-type TCOs the majority charge carriers are positively charged holes [10]. Preparation of p-type TCOs needs shallow acceptor level slightly above the valence band [61]. Synthesis of p-type TCOs is an emerging field in TCO technology. Intensive work has been done over the last decade to fabricate new p-type TCOs by various deposition techniques. Several studies have also been carried out for proper understanding of the structural, optical and electrical characteristics of p-type TCOs [6]. The p-type conductivity of TCO materials can be determined by measuring the Seebeck and Hall coefficients [24] or by examining the Fermi energy level which for p-type semiconductors lies at the edge of valence band [69]. However, since the design of first TCO reported by Badeker in 1907, no p-type TCO was reported until 1993 due to the localization behavior of the induced holes for p-type TCO fabrication [6].

2.8 Problems in designing p-type TCOs

Many metallic oxides have wide bandgaps because of the significant contribution of ionic character to the chemical bonds between metallic cations and oxides ions. Their ionic nature simultaneously suppresses the formation of easily ionisable shallow donors or acceptors levels and enhances the localization of electrons and positive holes. However, oxides of p-block heavy-metal cations with ns^0 electronic configurations (where n stands for principal quantum number) - such as ZnO, CdO, In_2O_3, Ti_2O_3, SnO_2, PbO_2, Sb_2O_3 and their mixed oxides can be changed into n-type conductors by electron doping [13]. But the situation for p-type TCOs is not as simple as for n-types, because of the strong localization behavior of positively charged holes at the valence band edge of the oxide materials [13], which can not migrate even under a consistent electric filed [24]. The CBM of most metal oxides is made of spatially spread spherical metal s orbital, and high electronic conduction is possible if high density electron doping is achieved [34]. In contrast, VBM is made of oxygen 2p orbital, which is far lower lying than the valence orbit of metallic atoms [34]. And because of the large electronegativity of oxygen, the positive holes introduced at the valence band edge are localized on oxygen ions and constitute a deep trap [25] with large energy barrier of migration, resulting in poor conductivity [9]. Furthermore, the dispersion of the valence band is small and thus the VBM level is so deep that the hole doping is difficult [34].

Since this localization is due to the ionicity of metallic oxides [25], so the proposed solution was the introduction of covalency in metal-oxygen bonding [24] to induce the formation of extended valence band structure [13]. This method of obtaining p-type TCOs is called Chemical Modulation of the Valence Band (CMVB) proposed by H. Kawazoe et al. in the year 2000 [13].

2.9 Chemical Modulation of the Valence Band

The Chemical Modulation of the Valence Band (CMVB) is a method of inducing covalency in metal-oxygen bonding, which delocalize the holes in the valence band edge of the oxide materials [13]. However, this method requires the choice of appropriate cationic species and crystal structures that serve the CMVB technique [6,13]. If the energy level of the uppermost closed shell on the metallic cation is almost equivalent to those of the 2p levels of the oxide ions (as shown in the figure 2.4), the chemical bonds with considerable covalency are formed between metallic cations and the oxide anions [13]. Here the closed shell is required to avoid the optical absorption in the visible range due to intra-atomic excitations [33]. In this combination considerable covalency can be expected for both bonding and anti-bonding levels [25,70]. Non-bonding states always have a high effective mass and so they give deep hole levels. They can also have a high mass, if the bond ionicity is large [71]. Investigations showed that the required cationic species are the $3d^{10}$ closed shell of Cu^{+} ions or $4d^{10}$ closed shell of Ag^{+} ions [6].

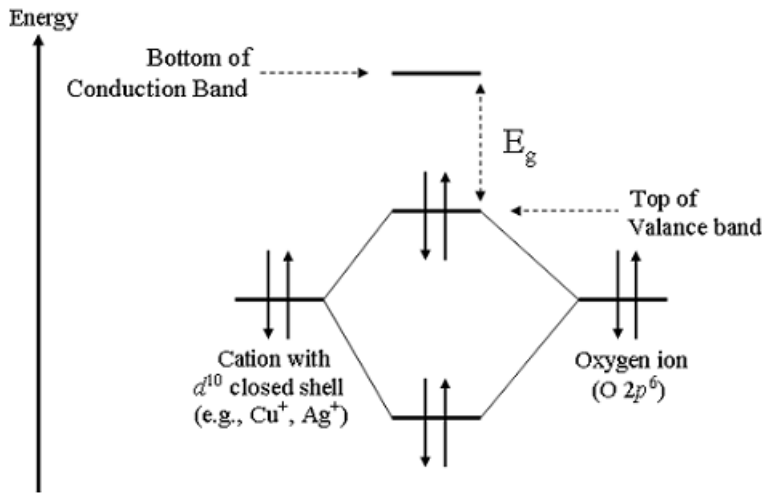

Figure 2.4: Schematic illustration of the chemical bond between an oxide ion and a cation that has a closed-shell electronic configuration suitable for CMVB technique [1]

In Figure 2.4, The energy of the closed-shell electrons on the cation is assumed to be equivalent to that of oxygen 2p electrons. The top of the valence band consists of cation d orbitals and oxygen 2p orbitals.

Next is the structural requirement for designing p-type TCO materials. This structural requirement is related to the delocalization of holes (for enhancing conductivity) and widening of the bandgap (for improving transparency) [33]. Materials with delafossite crystal structure ABO_2 (A = monovalent ions, e.g. Cu^{+}, Ag^{+} and B = trivalent ions, e.g. Al^{+3}, Ga^{+3}, In^{+3}, Cr^{+3}, Fe^{+3}, Co^{+3} etc) were chosen as candidates for p-type TCOs for several reasons as shown in figure 2.5 [6].

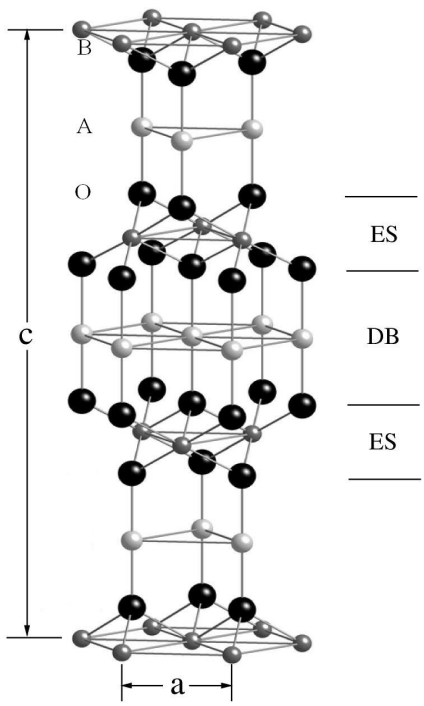

Figure 2.5: Crystal structure of delafossite, A and B denote mono- and trivalent cations, respectively. DB stands for the dumbbell layers and ES for edge-sharing layers [2]

If we investigate the delafossite structure shown in figure 2.5. First we see that delafossites have a hexagonal, layered crystal structure: the layers of A cations and

BO_2 are stacked alternately. The BO_2 layers consist of B-O_6 octahedral sharing edges. This two dimensional layered coordination of cations is advantageous for good transparency due to the enhancement of bandgap [6]. Second, each oxide ion is in pseudo-tetrahedral coordination, as B_3AO [13]. The tetrahedral coordination of oxide ions is advantageous for p-type conductivity, as it acts in reducing the localization behavior of 2p electrons on oxide ions. The valence state of the oxide ions can be expressed as sp^3 in this conformation. Eight electrons (including $2s^2$) on an oxide ion are distributed in the four σ bonds with the coordinating cations. This electronic configuration reduces the non-bonding nature of the oxide ions and increases the delocalization of holes at the valence band edge (that is why Cu_2O is a p-type conducting oxide) [13]. But Cu_2O, though p-type in nature, has rather small bandgap (2.17 eV). This is probably because of the three-dimensional interactions between $3d^{10}$ electrons of neighboring Cu^+ ions [6].

And finally, another important factor in this structure is the low coordination number of the A ions due to the large separation from oxygen ligands, which is the result of the strong columbic repulsion between 2p electrons in oxygen ligands and A d^{10} electrons. This leads to the A d^{10} energy levels almost comparable to the oxygen 2p level, resulting in a high degree of mixing of these levels, which is essential for the CMVB technique [6].

2.9.1 Copper-based delafossite structure

In the delafossite structure category, there are two groups of p-type TCOs: Cu-based $CuBO_2$ and Ag-based $AgBO_2$. However, most of the p-type semiconducting delafossite materials are Cu-based. The corresponding Ag-based delafossite materials are difficult to synthesize by simple solid state reaction. The Cu-based delafossites have greater hole mobility due to Cu-3d character of the valence band edge [6] as the VBM is dominated by Cu-3d states and a hole created on Cu ion is less localized [61]

whereas the Ag-based delafossites possess O-2p character, and d-manifold holes are more mobile than that of p-manifold [6]. Furthermore, the Cu-3d orbital energy is a bit higher than O-2p orbital energy, so the VBM rises up giving rise to higher p-type doping [8]. The Cu-Cu distance in copper-based delafossite can be a limiting factor in p-type conductivity, as the delafossites are governed by a polaronic hole hopping conduction mechanism. In delafossite materials, the hole hops from Cu to Cu, making shorter Cu-Cu distance is extremely beneficial for good undoped conductivity [61].

The most important material in this group is copper aluminium oxide $CuAlO_2$ (CAO) [6]. After the report of CAO as p-type TCO, a research field in device technology has emerged, called "transparent electronics" [25]. Other p-type TCOs in this group are: $CuGaO_2$, $CuInO_2$, $CuCrO_2$, $CuYO_2$, $CuScO_2$ etc [6]. Delafossite thin films, though show very nice optical and electrical properties, suffer from the serious drawback of very high deposition temperature (700 °C) [24]. Furthermore, all the delafossite TCOs are indirect bandgap semiconductors [72] and for the production of pn-junction a TCO with a direct bandgap [9] and low deposition temperature is preferred in order to avoid the chemical reaction with its n-type counter part [55].

2.9.2 Copper-based non-delafossite structure

Materials with delafossite structure were successfully found to be p-type TCO by following CMVB technique. As an extension of this approach, another crystalline phase $SrCu_2O_2$ was examined [3], other TCOs in this group are $MgCu_2O_2$, $CaCu_2O_2$ and $BaCu_2O_2$ [7]. All these new p-type TCOs have direct bandgaps [7] and can be deposited at low temperature in comparison to delafossites [3, 24]. Other Cu-base p-type TCOs are LnCuOCh (Ln = Lanthanide, Ch = Chalcogen) with a layered crystal structure consists of $(\mathrm{Ln_2O_2})^{2+}$ with $(\mathrm{Cu_2Ch_2})^{2-}$ layered stacked alternately along c-axis [34], $CuAlS_2$ with the chalcopyrite structure (a superlatice of zinc blende) [73] and layered oxysulfide $[\mathrm{Cu_2S_2}][\mathrm{Sr_3Sc_2O_5}]$ have also been recognized as p-type TCOs [74].

2.10 $SrCu_2O_2$

$SrCu_2O_2$ (SCO) is a promising candidate for p-type TCOs because of its large direct bandgap ($\sim$ 3.3 eV) and low deposition temperature [3,7]. The introduction of SrO into Cu_2O reduces the oxygen mediated d-d coupling between Cu atoms and increases the bandgap [7, 8]. The SCO exhibits a body-centered tetragonal crystal structure with bulk lattice constant of a = 5.48 Å and c = 9.82 Å [18]. In describing the SCO crystal structure, a Sr ion is coordinated by six O ions to form a slightly distorted octahedron. The Cu atoms form the well-known O-Cu-O dumbbell configuration, which is similar to that of Cu_2O (figure 2.6a) [7]. In fact, $SrCu_2O_2$ can be considered as derived from Cu_2O, in which one Cu atom is removed for each unite of distorted Cu_2O, plus an inter-penetrating body-centered tetragonal Sr sublattice (figure 2.6b) [7].

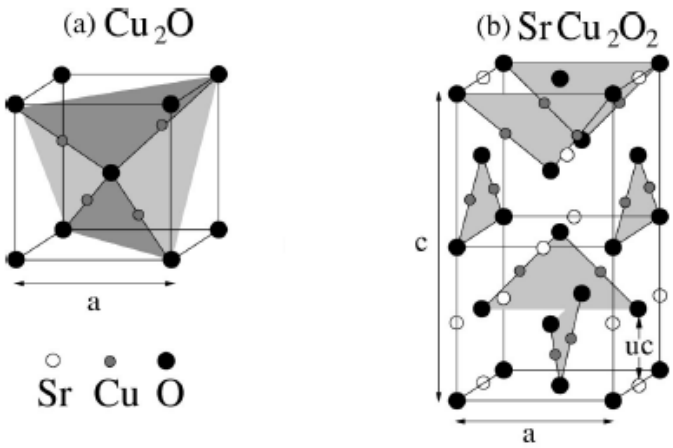

Figure 2.6: Crystal structure of (a) Cu_2O and (b) $SrCu_2O_2$. $SrCu_2O_2$ can be considered as derived from Cu_2O, in which one Cu atom is removed for each unite of distorted Cu_2O, plus an inter-penetrating body-centered tetragonal Sr sublattice [7]

Synthesis of SCO utilises the same CMVB approach and the VBM is composed of mostly Cu d and O p [7] (Figure2.7a) but the resulting crystal structure is not that of delafossite [1] (Figure2.7b).

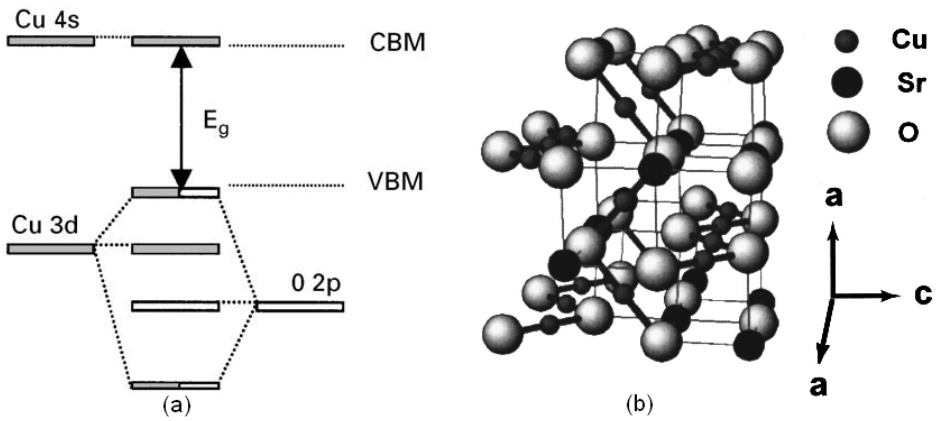

Figure 2.7: (a) CMVB approach for CBM and VBM, and molecular orbitals for SCO [1]. (b) Crystal structure of SCO, the zigzag one dimensional chains of -O-Cu-O-Cu-O- running along [100] and [010] directions causes high transparency in SCO by enlarging the bandgap [3]

The O-Cu-O dumbbells in SCO are connected to form one-dimensional zigzag chains along [100] and [010] directions, respectively. The angle between them is 96.25°. The electronic interactions between d^{10} electrons of the nearest neighboring Cu^+ ions are restricted to a one dimensional chain [3, 7], in contrast to the three-dimensional structure of Cu_2O and two-dimensional in delafossites [33]. This one dimensional Cu-Cu interaction leads to bandgap widening by narrowing the d band width [7, 13]. The origin of the p-type behavior in SCO appears to reside in the +1 valence state of Cu cation [18]. Both the Cu_2O and SCO are direct bandgap materials with their band edges at the zone center (Γ). The calculated bandgaps for SCO is 3.33 eV , whereas, that for Cu_2O is 2.1 eV [7, 18]. In SCO, the probabilities of transition between the VBM and other valence states below VBM within 4 eV is calculated to be negligible [7]. This factor is very important for a TCO to be transparent in the visible range in addition to large bandgap as the fundamental bandgap is not enough to guarantee transparency [7]. Unlike conventional semiconductors and n-type TCOs, it has been found that for SCO the effective masses of valence band states are smaller than those of conduction band states due to oxygen mediated coupling between Cu d states [7].

Comparison of the band structures of Cu_2O, $SrCu_2O_2$ and $CuAlO_2$ (a delafossite) is given in the figure 2.8 [7, 8].

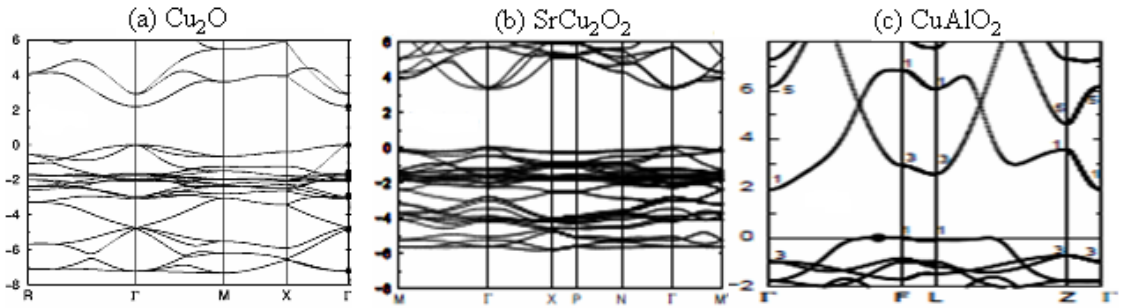

Figure 2.8: Calculated electronic band structures of (a) Cu_2O [7], (b) $SrCu_2O_2$ and (c) $CuAlO_2$ [8]. Clearly Cu_2O and $SrCu_2O_2$ have direct bandgaps, while $CuAlO_2$ has indirect bandgap.

Cu_2O and $SrCu_2O_2$ have direct bandgaps with both CBM and VBM states at Γ, whereas $CuAlO_2$ has an indirect bandgap with the CBM state at Γ and the VBM state on the Γ-F line near F, as indicated by the black circle in the figure 2.8(c) [7, 8].

In SCO the holes are generated as a result of oxygen interstitials O_i, copper vacancies V_{Cu} and strontium vacancies V_{Sr} as shown in the figure 2.9 [9].

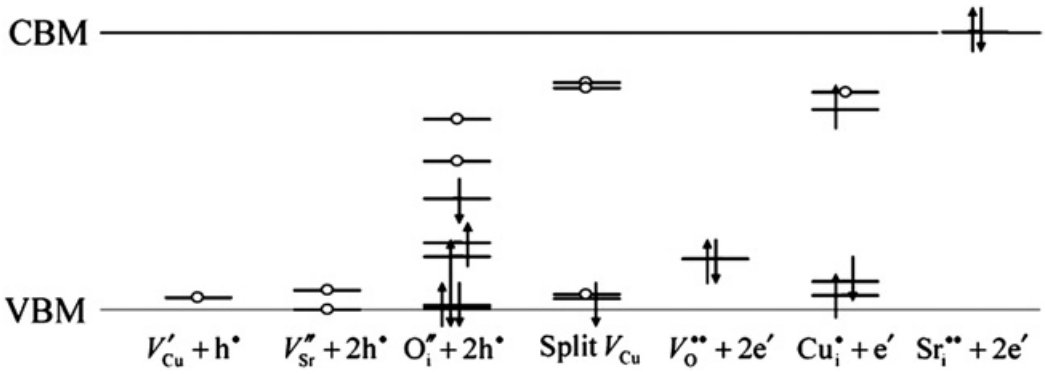

Figure 2.9: Charge carrier generation mechanism in SCO. Positions of single particle levels in band gap of $SrCu_2O_2$ at the Γ point. Empty circles indicate holes and arrows indicate electrons in the up/down spins [9].

Each Cu vacancy creates one hole state $V_{Cu'} + h^{\bullet}$ at 0.09 eV above the VBM,

while each Sr vacancy creates two hole states $V_{\mathrm{Sr}''}$ + $2h^{\bullet}$, one at VBM and the second at 0.15 eV above VBM and each O interstitial produce two hole states $\mathrm{O}_{\mathrm{i}}''$+ $2h^{\bullet}$ at 1.13 and 1.45 eV above VBM. Split vacancies which arise from two Cu vacancies and one interstitial Cu ion produce two hole states near CBM and one hole state near VBM [9].

2.10.1 Reports on SCO

SCO as a p-type TCO is of potential interest for wide bandgap electronics, photonics and sensors [18]. The first undoped and K-doped SCO deposited on SiO_2 glass substrate by pulsed laser deposition (PLD) at 300 °C was reported by A. Kudo et al. in 1998 [3]. Introduction of singly charged K^+ onto Sr^{2+} generates hole into the previously full Cu 3d bands, provided the oxygen stoichiometry is unchanged [75]. Su Sheng et al. reported Ca-doped SCO deposited by PLD in 2006 with higher conductivity than that of undoped and K-doped SCO [56]. Doping SCO with divalent Ca is expected to increase conductivity by decreasing the effective hole mass and to increase transparency by widening the bandgap [7]. Extending the idea of Ca doping, Zhuang et al. reported the synthesis of CaO-doped SCO thin film in 2006 [76]. Based on the first prinicples calculations of the NATCO project, Louloudakis et al. have recently reported Ba-doped SCO by PLD [77].

Most of the SCO thin films reported so far being fabricated by PLD [3, 18, 52, 56, 78, 79] have been difficult to reproduce [80]. Roy et al. reported the synthesis of SCO by sol-gel in 2003 [80]. Deposition of SCO by e-beam evaporation was reported by Bobeico et al. in 2003 with electrical conductivity comparable to that of K-doped SCO by Kudo via PLD [24]. In 2004, Alex Martinson reported synthesis of SCO from water based liquid precursors using a spray technique [10]. Fabrication of SCO on ZnO substrate by RF-magnetron sputtering was reported in 2005 by Nakamura et al [81]. The undoped and K-doped bulked SCO were prepared by firing an intimately ground and pelletised mixture of $SrCO_3$ and CuO by Lynch et al in 2005 [75]. Wei-Wei

Zhuang et al. reported the synthesis of SCO by spin coating process in 2007 [82]. In 2008, we reported synthesis of SCO for the first time by injection MOCVD [83].

Deposition technique	Doping	Conductivity (Scm^{-1})	Transparency (%)	Bandgap (eV)	Reference
PLD	–	7.3×10^{-3}	70	3.3	[3]
PLD	K	4.8×10^{-2}	70	3.25	[3]
PLD	Ca	8.2×10^{-2}	65	3.2	[56]
PLD	–	6.5×10^{-3}	80	3.3	[79]
PLD	Ba	–	60	3.24	[77]
Spray deposition	–	–	–	–	[10]
e-beam evaporation	–	5.3×10^{-2}	60	3.12	[24]
Sol-gel	–	–	–	–	[80]
Spin coating	CaO	10^4 ?	–	–	[76]
MOCVD	–	–	–	–	[83]

Table 2.2: Reports on SCO with its corresponding deposition techniques and its opto-electrical properties

The integration of SCO thin film into functional devices has already been reported. Transparent hetero pn-junctions have been fabricated by various researchers using SCO as p- and ZnO as n-type TCO [1, 81, 84–86]. This demonstrates the suitability of SCO for the use in transparent electronic devices. However, the obtainable electrical conductivity and optical transparency of SCO are yet to be improved.

2.11 Ba Doping of SCO

K and Ca doping of SCO have been reported so far [3,56]. However, a promising improvement in the optoelectronic properties of SCO has not been achieved as they appear to reduce the bandgap and increase the conductivity a little bit. The bandgap calculated for undoped SCO is 3.34±0.01 eV [78], for K-doped SCO is 3.25 eV [3] and for Ca-doped SCO is 3.2 eV [56]. Therefore, searching a new doping material for SCO which can simultaneously enhance its electrical conductivity and the bandgap to a promising level will be a milestone in the study of p-type TCOs. SCO is supposed to

be a p-type semiconductor with the holes as majority charge carriers. The formation of holes in SCO results from the Cu vacancies: $\mathrm{Cu_{lattice}(I)} \rightarrow \mathrm{Cu^{(0)}} + \mathrm{h^{+}}$. However, there had been no modelling work of this defect process [87]. The first principles calculations of SCO by our NATCO parnter in Tyndall indicates the low Cu vacancy formation energies, which result in the formation of acceptor states with favorable hole masses for p-type semiconducting properties. The calculated formation energy of oxygen vacancy (3.86 eV), which is the base of n-type conductivity, is much more higher than that of Cu vacancy (0.64 eV) [88]. For doping with Ba^{2+}, M. Nolan of Tyndall group demonstrated substitution of Sr atom with Ba atom. For Ba doped SCO, the calculated bandgaps and hole effective masses, shows improvements over K and Ca doped SCO. The formation energy of a single Cu vacancy in Ca and Ba doped SCO is given the table 2.2 [41], where for comparison, the formation energy of a Cu vacancy in undoped SCO is also presented. For the doped materials the dopant concentration is given in parenthesis beside the formation energy [89].

Vacancy Concentration	**E^{vac}(SCO)/eV**	**E^{vac}(Ca-SCO)/eV**	**E^{vac}(Ba-SCO)/eV**
12.5	0.73	0.82 (25%)	0.64 (25%)
6.3	0.60	.....	0.53 (12.5%)
3.0	0.57	0.58 (6.3%)	0.50 (6.3%)

Table 2.3: Cu vacancy formation energy in the undoped, Ca-doped and Ba-doped SCO

From this table, we see that Ba doping of SCO results in a notable decrease of the Cu vacancy formation energy for a given concentration, while Ca doping leads to an increase in the Cu vacancy formation energy, particularly for large Cu vacancy concentration. The measured bandgaps for 3 and 6% Ba-doped bulk SCO by spectroscopic ellipsometry are 3.37±0.01 eV and 3.40±0.01 eV respectively [89]. The ionic radius of Ba^{2+} is larger than Cu^{+}, which results in the strong structural distortion around the dopant sites. This structural distortion increases the Cu-Cu distance and decreases the Cu-Cu interaction which leads the widening of the bandgap [90]. Thus, from the point

of view of obtaining high transparency and useful p-type semiconducting properties, Ba doping of SCO might be a useful alternative approach to K and Ca doping.

2.11.1 Reports on p-type TCOs

Since the initial reports on NiO, $CuAlO_2$, and SCO as p-type TCOs, considerable research on finding promising p-type TCOs has been done in the last decade. Materials recognized so far as p-type TCO are $MgCu_2O_2$, $CaCu_2O_2$, $BaCu_2O_2$ [7], $BaCu_2S_2$ [91], BaCuSF [92], $CuAlS_2$ [93], $CuGaO_2$ [94], $CuInO_2$ [95], $CuCrO_2$ [96], $CuBO_2$ [97], $CuScO_2$ [98], $CuYO_2$ [99], InZnO [53], SnO, Bi_2O_3 [100], Ag_2O [101], LaCuOSe, LaCuOS [102], $[Cu_2S_2][Sr_3Sc_2O_5]$ [74], BiCuOS, BiCuOSe [103], YCuOSe [104], $ZnRh_2O_4$ [105], Sn-Sb_2O_4 [106] etc. All these reports signify the importance of p-type TCOs and the intensive research work going on in this field.

3

Thin Films Experimental Techniques

THE principal application of TCOs is in the form of thin films. Thin films can be deposited by various deposition techniques. Each of these techniques has advantages and disadvantages associated with it. A deposition technique is preferred on the basis of good film quality, simple deposition process, good control of deposition process, low price, high deposition rate, large area deposition, etc. Several different deposition techniques are currently in use in various research laboratories. Most common of these deposition techniques are; Pulsed Laser Deposition (PLD), Sputtering, Chemical Vapor Deposition (CVD), Spray Pyrolysis, Spin Coating, Dip Coating, Molecular Beam Epitaxy (MBE), Thermal Evaporation, Electron-beam Evaporation, etc. Different deposition techniques yield films with diverse structural, chemical, optical and electrical properties. Even for the same deposition technique, a slight variation in the deposition parameters produces films with different properties. Sometimes the as-deposited films are amorphous or contain unwanted phases (contaminations), such films need some post-deposition treatments to crystallize the film and decompose the unwanted phases. Various characterization techniques are used to determine the suitability of the TCO thin film in a particular application. The film morphology is characterized by electron and optical microscopy, film composition by Wavelength Dispersive

X-ray (WDX) and Energy Dispersive X-ray (EDX) analysis, and phase identification by X-ray Diffractometry (XRD), Infrared and Raman Spectroscopy, etc.

3.1 Thin Films Deposition Techniques

Thin film deposition is the process of adding a thin layer of one material on another. The underlying material on which the layer is added is known as substrate and the layer itself is called thin film [107]. Thin films have become a significant part of microelectronic circuitry because of their small thickness, i.e. a nearly two-dimensional structure, which permits the fabrication of very small devices or microcircuits [107]. Thin film technology is based on three foundations; fabrication, characterization and applications [108]. Thin films are used for electronic components, electronic displays, optical coatings, magnetic data storage, optical data storage, anti-static coating and hard surface coatings, etc. There are dozens of thin film deposition techniques for various applications [109]. Thin film deposition techniques can be conveniently divided into two classes; (1) Physical Vapor Deposition and (2) Chemical Vapor Deposition. However, a considerable number of deposition techniques combine both physical and chemical processes as-well [109].

The steps common to all techniques of film deposition are:

1. Generating a supply of atoms or molecules from a source that may be solid, liquid or vapor. This is done by supplying energy to the source by heating, by kinetic energy from incident energetic particles or by using chemical reaction to produce volatile species.

2. Transport of the constituent atoms or molecules to the substrate. From a technological point of view, this is the crucial part of a deposition, because the manner of transport determines the quality of the film.

3. Deposition of atoms or molecules on the substrate. The condition of the substrate

surface plays important role in this part of the deposition process. If the substrate surface is contaminated with a fraction of monolayer of impurity atoms, the surface mobility of the arriving atoms may be effected to an extent that the crystal orientation of the film bears little relationship to that of the substrate, and the structure is likely to be polycrystalline. Conversely, if the substrate surface is essentially clean, the arriving atoms are likely to adsorb on sites related to substrate orientation, and the film may be preferentially oriented or even epitaxial.

4. Post-deposition treatment. In this part of the process, a prolonged annealing of the film at elevated temperature may yield a film with superior properties as a result of crystal grain growth in the film, stress reduction, the changes in composition produced by diffusion of constituents, etc.

5. Process analysis. Modern in-situ analytical techniques are used to monitor the deposition or post-deposition parameters in order to improve quality of the film in term of structure or purity, or both [107].

3.1.1 Physical Vapor Deposition Techniques

Physical vapor deposition technique is the transfer of atoms and molecules from a source to a substrate by a process that relies on physical methods to produce the vapor species. Physical vapor deposition is carried out in high vacuum to avoid contamination of the film by ambient atmosphere [107]. Some common and well-known physical vapor deposition techniques are:

- Pulsed Laser Deposition (PLD): This technique is based on physical vapor deposition processes arising from the impact of high-power short pulsed laser irradiation of solid targets that leads to the removal of material from the focused zone [110]. PLD is relatively new but very efficient technique to deposit epitaxial films. It is a somewhat costly process, but can produce high quality films

with high accurate thickness control [6]. However, reproducibility, large area deposition and reduction of particulate emission have yet to be improved [110].

- Sputtering: This technique relies on the removal of atoms from the target by bombarding the target surface with high energetic particles. The target, which is called cathode, is the material to be deposited and substrate is referred to as anode [110]. Sputtering is relatively cost-effective compared with PLD and large area deposition is possible by this process [6].

- Thermal Evaporation: This process comprises evaporating source materials in a vacuum chamber and condensing the evaporated particles on a substrate. Thermal evaporation is conventionally called vacuum deposition. Resistive heating is commonly used in this deposition, therefore this technique cannot be applied to high melting point materials and poor thermal conductors [111, 112].

- Electron Beam Evaporation: This technique is an improvement over thermal evaporation in which a preheated target is bombarded with a highly accelerated beam of electrons in order to vaporise the target. Source electrons as well as secondary electrons trapping and electron beam arcing are the problems associated with this technique [112].

- Molecular Beam Epitaxy (MBE): This process is based on the deposition of thermal beam of atoms or molecules on the clean surface of a single-crystalline substrate held at high temperature under ultra high vacuum conditions to form an epitaxial film [113]. MBE is a sophisticated and finely controlled method for growing single-crystal epitaxial films in high vacuum. Limitations of MBE are the expensive equipment and its complex operation [109].

3.1.2 Chemical Deposition Techniques

A deposition technique, in which chemical components react on the surface of the substrate to form a solid film is called chemical deposition technique [114]. In contrast to physical deposition technique, the chemical deposition often utilizes an inert gases and may be carried out at atmospheric pressure [107]. Some of the commonly used chemical deposition techniques are:

- Chemical Vapor Deposition (CVD): The process by which the non-volatile products of a gas phase reaction are allowed to deposit onto a substrate is known as chemical vapor deposition [115]. The main feature of CVD is its versatility for synthesizing both simple and complex compounds with relative ease. Fundamental principles of CVD encompass an interdisciplinary range of gas-phase reaction chemistry, thermodynamics, kinetics, transport mechanisms, film growth phenomena and reactor engineering [109]. The advantages of CVD include high deposition rate, low price and flexibility in composition control. However, due to high deposition temperature, CVD is not suitable for substrates which are thermally unstable at high temperatures [116].

- Spray Pyrolysis: In this deposition technique, liquid precursors are sprayed by atomization processes and condensed by thermal decomposition on substrates maintained at elevated temperatures. The sprayed micro-droplets reaching the hot substrate surface undergo pyrolytic decomposition and form a single crystallite or a cluster of crystallites of the sprayed materials. Spray pyrolysis was used as early as 1910 to obtain transparent oxide films [117]. A disadvantage of spray pyrolysis in some cases is the lack of morphological control over the product particles and the subsequent frequent formation of hollow and/or porous particles. The hollowness of particles can cause a reduction in brightness and long-term stability. Therefore, morphology control of particles in the spray pyrolysis is

crucial [118]

- Spin Coating: Spin coating process consists of putting the drops of liquid precursor on the surface of a spinning substrate [119]. The film formed on the substrate results from two balancing forces: the centrifugal force (due to spinning) which drives the viscous sol radially outwards and viscous force (due to friction) which acts radially inwards [120]. Spin coating is the cheapest film production method in silicon technology [121]. However, thinner films (<100 nm) are hard to make and can waste 98% of the process materials [122].

- Dip Coating: Dip coating or immersion coating is a simple old way of thin film deposition by immersing a substrate in the solution of the coating material at a constant speed (preferably judder free). Film thickness is set by the competition among viscous force, capillary (surface tension) force and gravity. Thickness and uniformity can be sensitive to flow conditions of the substrate in the liquid bath and gas overhead. The faster the substrate is withdrawn, the thicker the film deposited. Theoretical prediction of process performance is more difficult, and control of the process more demanding. In R & D labs it is far less often used in coating manufacture [123].

The above mentioned deposition techniques are some of the commonly used techniques in thin film technology. There are number of other deposition techniques used for thin film growth due their corresponding advantages in one way or the other. For example, we used Metal-Organic CVD because of its low price, large area deposition and high growth rate. However, it suffers from high deposition temperature which is expected to be reduced with a UV-assisted reactor.

The selection of a specific technique for the deposition of thin films can be based on a variety of considerations. A multitude of thin films of different materials can be deposited for a large variety of applications; hence, no general guidelines can be given

of what the most suitable deposition technique should be [109].

3.2 Criteria for selection of a deposition technique

In recent years, thin film science has grown world-wide into a major research area. The importance of coatings and synthesis of new materials for industry have resulted in a tremendous increase of innovative thin film processing technologies [124]. As has been discussed earlier, a wide variety of techniques are available for the deposition of thin films. These techniques differ to a large degree in their physical and chemical principles of operation and in the commercially available types of equipment. Each technique has been pursued or developed because it has unique advantages over others. However, each technique has its limitations as-well. In order to optimize the desired film characteristics, a good understanding of the advantages and restrictions applicable to each technique is necessary [109].

The selection of a particular deposition technique depends on several factors, they are [125]:

1. The material to be deposited
2. Rate of deposition
3. Limitations imposed by substrate, e.g., maximum deposition temperature
4. Adhesion of the deposits to substrate
5. Throwing power
6. Purity of target material
7. Availability of the required equipment
8. Cost

9. Ecological considerations

10. Abundance of the material (to be deposited)

The desired film thickness is closely related to the film growth rate, which, in turn, depends on the reactivity of the source materials used for thin film deposition. These source materials can be either solid, liquid or gaseous and their delivery into the deposition reactor need considerable attention. Special techniques exist for each source material delivery and their rate of delivery to deposition reactor.

All thin-film deposition equipments are quite susceptible to the integrity of the processing environment. For proper pressure control inside the deposition reactor, the leakage of the gases has to be minimized. For example, in MBE deposition technique, a maximum leak rate (degassing rate) of 10^{-12}torr liter/cm^2 sec is acceptable, whereas some other techniques can easily tolerate much higher leak rate.

The purity of the deposited film not only depends on the purity of the source materials delivered to the reactor and the leakage-tightness of the system, but also to a large extent on the substrate cleaning procedure.

The stability and reproducibility of the process is of considerable importance. Many different factors can influence the deposition process and it is extremely important to understand and control these parameters.

Uniformity of the deposited films, both in thickness and composition, is of great concern for most deposition techniques. This impose severe restrictions on the design of deposition reactor, the delivery of the reactant materials, and the control of process parameters.

For multi-layered thin films, the thermal, chemical, topographical and metallurgical compatibility of the deposition with the existing layer is of major consideration for successful solid-state device fabrications [109].

The equipment for the deposition of thin films can be classified into three basic categories:

- Thin film deposition equipment for device research and development.
- Prototype equipment for the study of new or established deposition techniques.
- Thin film production equipment for device manufacturing.

The deposition equipment for the research and development of new device structures has to meet, in general, quite different requirements than the equipment used in the manufacturing of devices on large scale. Research and development equipment requires a high degree of flexibility in deposition parameters.

Cost-effectiveness of the deposition equipment is of major consideration, which can be characterized as the ratio of cost per device to the value added to the device. The cost per device include the price of raw-materials, device processing time, equipment price and its maintenance.

The automation of deposition equipment is making rapid progress. Automated deposition systems provide automatic loading and unloading of the substrate, process sequencing and control of variables, such as reactor pressure, gas flows and substrate temperature [109].

A variety of different thin-film deposition techniques and equipments are available from which selection of a particular thin-film deposition technique can be made in terms of specific applications, material characteristics and processing.

3.3 Material Characteristics

The desired material characteristics of the deposited thin films will be, in most cases, the decisive factor for the selection of a preferred deposition technique. In many, if not most, instances the characteristics of a thin film can be quite different from the

bulk material properties, because of the large surface to bulk-volume ratio of the thin films [109]. The high surface-to-volume ratio dramatically change both the physical properties; like, refractive index, extinction coefficient, homogeneity, density, hardness, internal stress, adhesion to surface and chemical characteristics like purity, stoichiometry, crystal structure, reactivity, gas permeability and solubility. These differences between bulk and thin film material depends strongly on the type of deposition process and its process parameters; like, deposition temperature, deposition rate, gas pressure, substrate geometry and preconditioning, preparation of the coating material and post-deposition treatment, etc [19]. The surface and/or interface properties of the substrate can drastically influence thin film characteristics due to surface contamination, nucleation effects, surface mobility, chemical surface reaction, adsorbed gases, catalytic or inhibitory effects on film growth, surface topography, crystallographic orientation and stress effects due to thermal expansion mismatch

In selecting an appropriate deposition technique for a specific application, several criteria have to be considered. Thin films applications area include, electronics, optics, magnetism and material protection coating.

The major physical and chemical parameters of the thin film to be considered in various applications are [109]:

Electrical: Conductivity of conductive films
Resistivity of resistive films
Dielectric constant
Dielectric loss
Stability under bias
Polarization
Electromigration
Radiation hardness

Thermal:	Coefficient of expansion
	Thermal conductivity
	Temperature variation of all properties
	Stability or drift of characteristics
	Thermal fusion temperature
	Volatility and vapor pressure
Mechanical:	Intrinsic, residual and composite stress
	Anisotropy
	Adhesion
	Hardness
	Density
	Fracture
	Ductility
	Elasticity
Morphology:	Crystalline or amorphous
	Structural defects
	Conformality/step coverage
	Planarity
	Microstructure
	Surface topography
	Crystalline orientation
Optical:	Refractive index
	Absorption

	Birefringence
	Spectral characteristics
	Dispersion
Magnetic:	Saturation flux density
	Coercive force
	Permeability
Chemical:	Composition
	Impurities
	Reactivity with substrate and ambient
	Thermodynamic stability
	Etch rate
	Corrosion and erosion resistance
	Toxicity
	Hygroscopicity
	Impurity barrier or gettering effectiveness
	Carcinogenicity
	Stability

3.4 Thin films characterization techniques

There are large number of characterization techniques used to evaluate film charateristics. One uses only some of them, the most relevant, and especially the most accessible. The art of characterization requires a great knowledge of the various existing techniques. Some are more precise, more reliable and faster. One can sometimes obtain the same information from two different techniques. It is thus necessary to know and to compile the results with their right values. Because, the characterization results

influence the modification of the deposition and post-deposition parameters settings.

The techniques used in studying thin films can be classified in two categories: in-situ techniques and ex-situ techniques. In-situ methods are those where thin film deposition process or post-deposition process is probed by one or several techniques during the deposition or post-deposition process. In the ex-situ techniques the film properties are characterized after the experiments (deposition and post-deposition processes) have been carried out [126].

When thin film materials, device structures and device processing conditions become increasingly more complex, there is a growing need for in-situ, real time, surface-specific analytical tools to characterize phenomena occurring at interfaces between layered structures and at the surface of thin films during growth. The analytical tools must be nondestructive, should provide a wide range of surface compositional and structural information on time scale that is in commensuration with the deposition rate, and must be compatible with geometric constraints of the deposition process [127]. Thin-film deposition equipment assisted with in-situ analytical tools consist of Reflection High-Energy Electron Diffraction (RHEED), Low-Energy Electron Diffraction (LEED), Scanning Probe Microscopy (SPM), X-Ray Photoelectron Spectroscopy (XPS) etc, and process monitoring techniques for measuring process parameters and film properties, such as, Ellipsometry and Plasma Analysis Techniques [124, 127].

In-situ characterization of deposition and post-deposition processes is necessary for the better understanding of thin-film properties and as an input for the modeling of the deposition process itself. Although in-situ methods provide more direct information on the film processing, the advantage of ex-situ technique is that the experimentalists may use several different characterization techniques to study various properties of the thin films after the deposition and post-deposition processes [126].

In-situ characterization techniques are also used to study the compositional, struc-

tural and morphological transformations in the films during the post-deposition treatment. These in-situ characterizations may include: Fourier Transform Infrared (FTIR) spectroscopy, Raman spectroscopy, X-ray diffraction measurements, Scanning Electron Microscopy (SEM), Transmission Electron Microscopy (TEM), etc. All these characterization tools need special modifications to be used in-situ, otherwise these can be equally used as ex-situ.

3.5 Post-deposition Treatments

Sometimes the as-deposited thin films do not exhibit the expected results. This may be due to lack of crystallinity, bad stoichiometry, contaminations, premature chemical reactions, or defects in microstructures, etc. Certain post-deposition treatments have been proposed by various researchers to obtain the expected results. These post-deposition treatments may include, Thermal Annealing, Aging, Etching or light exposure, etc. The most common of these treatments is annealing. Annealing can be performed in various gaseous atmosphere, for various durations and at various different temperatures [128].

3.5.1 Annealing

In semiconductor production annealing is an important process step. Annealing is a post-deposition process of heating thin-films at a predetermined temperature, holding for a certain time, and then cooling to room temperature to improve quality of the film and its properties [129] by reducing defects [130]. Post-deposition annealing is used to activate grain growth, alter stoichiometry, reduce the defects, introduce dopants, or cause oxidation [129]. High temperature annealing crystallizes the film and improves its structural quality by rearranging the crystal structure (e.g., point defect removal, doping activation) [19, 131, 132], thereby improving its optical and electrical properties [128]. For annealing treatment, many annealing parameters, such as tem-

perature, duration, atmosphere, and pressure could be varied [130]. Annealing can be performed in various environments ranging from vacuum to air or various gases. The effect of annealing rigorously depends on the annealing temperature, rate of heating and cooling, duration of annealing and the environment used inside the annealing chamber. The gases used for annealing may be steady or flowing continuously through the annealing chamber during the annealing process. Both these conditions have different annealing results.

Annealing can be classified into two types; (i) Conventional Annealing and (ii) Rapid Thermal Process Annealing.

3.5.1.1 Conventional Annealing

Conventional annealing also known as furnace annealing is a slow heating process (less than 20 °C/sec) for a prolonged duration (from hours to a day) [133]. Heating is achieved by electrical resistive heating system.

Historically, conventional annealing has been in the use of mankind to improve the mechanical properties of the materials. Today, it is used for improving/altering the mechanical as well as chemical, electrical, optical, magnetic, and microstructural properties of the materials. In thin film science, conventional annealing is a very effective tool for films on glass substrates. Control of temperature and its measurement is relatively an easy task for conventional annealing. Heating or cooling rate can also be controlled by moving the furnace towards or away from sample. This also makes possible observing the visual changes like color of the sample during annealing. Slow heating and cooling rate and the long duration of annealing are among the disadvantages of conventional furnace annealing.

3.5.1.2 Rapid Thermal Process Annealing

Rapid thermal Process (RTP) annealing is a process of heating the sample with very high heating rate (more than 100 °C/sec) for a very short duration (from fraction of minute to few minutes) [133]. The high heating rate is achieved by high intensity lamps or lasers.

In historical perspective RTP annealing was applied to introduce dopant atoms in Si crystal. The first RTP annealing technique using incandescent lamp was developed by W. K. Mannel in 1966 [134]. The key components of an RTP annealing system are: the radiant energy source with its reflector(s), the process chamber, the temperature measurement and control assembly, the gas panel, and the wafer transport system [135]. RTP annealing is essentially a heat transfer process between a radiant heat source and a semiconductor wafer, where, at high temperature radiation dominates convection and conduction. Due to this radiative character of heat transfer, the RTP annealing reactor walls are typically not in thermal equilibrium with the wafer, this prevent the contamination induced by the walls [136]. All RTP annealing systems possess essentially two methods of temperature measurements: an "absolute" method using a thermocouple that make contact with the wafer, or a non-contact optical method using a pyrometer [135]. Some advantages and disadvantages of RTP annealing are given as

Advantages:
- Large size sample
- High temperature
- Short processing duration (seconds to minutes)
- Computer controlled annealing process
- No cross-contamination due to cold wall configuration

Disadvantages:
- Exact temperatures are almost never known

- Less uniform heating due to high ramp heating rate
- Cannot be used for glass samples as glass reflects infrared radiations

3.5.2 Light Exposure

Internal stresses are developed in the film due to the mismatch in the thermal expansion coefficients of the film and the substrate [137, 138]. These stresses lead to the formation of cracks in the film [139] which degrade efficiency of the film [140]. The cracks so formed can be reduced significantly either by exposing the film to UV [141] or to laser [142]. The UV exposure promote cross linking between molecules [143], thereby shrinking the film and reducing the cracks [144].

3.5.3 Aging

Prolonged aging of the film has almost the same effect as that of thermal annealing to improve crystallinity and grain growth by releasing the stresses. However, upon prolonged aging local loss of adhesion has been observed in the films [138].

3.6 Thin Film Characterization Instruments

Thin films can be characterized in many different ways from microscopic to macroscopic scale by various characterization instruments. Analysis of the thin film properties varies from application to application. Geometry, microstructure, magnetic, electrical, optical, chemical, and mechanical properties are some of the common thin film properties analysed in most cases. Precise measurement of these properties requires sophisticated measuring instruments. Brief introduction of these instruments is given in the following subsections.

3.6.1 Electron Microscope

Electron microscope is an essential tool in modern research. An electron microscope is a type of microscope that produces an electronically magnified image of a specimen for detailed analysis. The electron microscope uses beam of electrons to illuminate the specimen and generates its magnified image. This microscope has higher magnification than a light powered optical microscope, because it uses electrons that have wavelengths about 100,000 times shorter than visible light photons, and can achieve magnifications of up to 1,000,000x, whereas light microscopes are limited to 1000x magnification. The electron microscope uses electrostatic and electromagnetic lenses to control and focus the electron beam on the specimen to form an image. These lenses are analogous to glass lenses in their functions (but different in geometry and working principle) of an optical microscope that form a magnified image by focusing light on or through the specimen.

An electron microscope is further classified into various types according to the measuring quantities.

3.6.1.1 Scanning Electron Microscope

A scanning electron microscope commonly known as SEM is used to study the topography, morphology, elemental composition and crystallographic orientation of the specimen. In the language of scanning electron microscopy, topography means the surface features of an object or “how it looks”. Morphology means the shape, size and arrangement of the particles making up the specimen. Elemental composition gives the information of the elements of which the specimen is composed of and their relative ratios. High resolution SEM can be used to measure thickness of the thin films. In most applications data is collected over a selected area of the surface of the sample, and a 2-dimensional image is generated that displays spatial variations in these properties. SEM is also capable of analysing selected point locations on the sample; this approach

is especially useful in determining chemical compositions. In SEM the electron beam is made to strike on the surface of the specimen and various signals such as secondary electron, backscattered electron, Auger electron and X-rays are detected and analysed to study the corresponding properties.

The scanning electron microscopes of the marks Phillips XL30 and Hitachi S-4500 available in LMGP were used in this Ph.D research work to study morphology, to measure the grain size and thickness and perform EDS analysis for determining the elemental composition of the as-deposited films and to compare with those of the annealed films.

3.6.1.2 Transmission Electron Microscope

Transmission electron microscope (TEM) is an improvement over SEM and is used for imaging solid materials at atomic resolution. Structural information can be acquired both by (high resolution) imaging as well as by electron diffraction. Additional detectors allow elemental and chemical analysis down to sub-nanometer scale. Unlike SEM, the electron beam in TEM passes through an ultra thin specimen and the transmitted beam is detected and analysed to study various properties of the specimen. The electron diffraction phenomenon in TEM is very useful in getting the crystallographic information of the specimen. TEM has a special feature of viewing a 3-dimensional image by acquiring a large series of images at many tilt angles (typically in 1° increments) of the sample.

The facility of transmission electron microscopy Jeol TEM 2010 in LMGP was utilized to study diffraction pattern of the SCO thin film and the film-substrate interaction at the interface in case of short and long annealing. In performing transmission electron microscopy, main focus was on the EDS analysis of the grains, their diffusion into the substrate, and their arrangement over the interface.

3.6.1.3 Atomic Force Microscope

Atomic Force Microscope (AFM) is a very versatile instrument to study the topography of various samples like metals, polymers, ceramics, composites, glass, and biological samples. Compared with SEM, AFM provides extraordinary topographic contrast, direct height measurements and unobstructed views of surface features as no conducting coating is required for sample preparation. Compared with TEM, three-dimensional AFM images are obtained without expensive sample preparation and yield far more complete information than the two-dimensional profiles available from cross-sectioned samples.

3.6.2 X-ray Diffractometer

X-ray diffraction (XRD) is one of the most important characterization tools for studying crystalline materials. XRD detects and analyses the diffracted X-rays from the crystallographic planes of the sample. This technique is mainly used for the chemical phase identification of both mono- and poly-crystalline unknown phases in a mixture. Moreover, XRD is used to determine structural properties like crystal structure, lattice parameters, d-spacing of crystal planes, grain size, expitaxy, and thickness of thin films.

To search for the SCO chemical phase in the as-deposited and annealed films, XRD of the mark Bruker D8 was used utilizing Cu as X-ray radiation source. The in-situ XRD facility of the mark INEL using Fe-$K_{\alpha 1}$ X-ray radiation source available in LMGP was utilized to study the transformation pathway of the crystallographic chemical phases during annealing under various gases atmosphere at different temperatures.

3.6.3 Fourier Transform Infrared Spectroscopy

Fourier transform infrared (FTIR) spectroscopy is a technique for identifying molecules through their molecular bond vibrations. The infrared transmittance or ab-

sorbance spectrum of a sample is recorded by passing a beam of infrared light through the sample. Performing a Fourier transform on this signal data (interferogram) results in a spectrum which reveals how much energy was absorbed at each wavelength. Analysis of these absorption characteristics gives information about the molecules present in the sample. FTIR spectroscopy can be equally applied to crystalline or non-crystalline molecules. However, molecules with symmetrical vibration modes cannot be observed by IR spectroscopy, such molecules can be observed by Raman spectroscopy.

To verify the results of XRD and to know about some amorphous phases (undetected by XRD) specially the carbonates present in the film before and after annealing, Bio Rad and Digilab FTIR spectrometers installed in LMGP were used in the wavenumber range 400-2000 cm^{-1} for 300 scans in transmission mode.

3.6.4 Raman spectroscopy

Raman spectroscopy is a technique used to identify molecules in a sample through the inelastic scattering of high energy monochromatic light (e.g. laser) by the molecules. The up or down shift in the scattered energy due the excitation/de-excitation is related to the vibrational energy of the molecules. This shift in energy of scattered light photon gives information about the chemical bond identification. However, molecules with antisymmetric vibrational modes cannot be detected by Raman spectroscopy, for the detection of such molecules IR spectroscopy is used. In this way, Raman and IR spectroscopy are complementary to each other. Both Raman and IR spectroscopy are very effective in determining the in-situ or ex-situ chemical phase transitions.

Since FTIR can only detect molecules with anti-symmetrical vibrations, therefore to verify once again XRD results and to know about the presence of amorphous phases undetected by FTIR, Olympus Jobin Yvon Raman spectrometer was used. With this microscope one can use three wavelengths of laser (red, blue and green) in the

wavenumber range 100-2000 cm^{-1}. This Raman microscope has also the facility to heat the sample up to 1000 °C in various gaseous atmosphere like O_2, Ar, air etc. So this Raman spectroscope was also used for the in-situ study of chemical phase transformation at different temperatures under various gases atmosphere.

3.6.5 UV-Visible Spectrometer

UV-Visible Spectrometer is used for measuring the optical transparency of thin films and chemical solutions in the UV-visible range. A beam of light in the UV-Vis-NIR range from a lamp is allowed to interact with the specimen. The optical properties such as the optical bandgap and refractive index of the specimen are measured by utilizing absorption, transmission, and reflection data as function of wavelength of the incident light.

Synthesis of highly transparent SCO thin film was one of the main objective of this Ph.D work. Optical transparency of the SCO thin films obtained after various deposition and post-deposition conditions on glass substrates was measured by Jasco UV/Vis spectrometer in the wavelength range 200-1100 nm and the results obtained were used to further optimize the deposition and post-deposition conditions to enhance the optical transparency of our SCO thin film.

3.6.6 Ellipsometer

An ellipsometer is used to measure the refractive index, thickness of thin films and modeling surface roughness. An elliptically polarized light is incident on the sample and the change in polarization of the reflected light is measured. This change in polarization is used to get information about the refractive index and thickness of the sample. An ellipsometer can be used to measure thickness of layers from 1 nm to several microns.

3.6.7 Four-point Probe Technique

The four-point probe technique was originally developed by Frank Wenner in 1916 to measure the earth's resistivity [145]. The four point probe technique is one of the most common methods for measuring resistivity for a known thickness of conducting/semiconducting thin films. This technique consists of four needle-like electrodes in a linear arrangement with a current injected into the material via the outer two electrodes and the resultant electric potential distribution is measured via the two inner electrodes. This technique is conveniently used for the spatial variation in resistivity of the thin films.

Fabrication of highly conducting SCO thin film is the main aim of this Ph.D work. To measure the resistivity and sheet resistance of our SCO thin films, we used the four-point probe measuring setup provided by Lucas in LMGP. Conductivities of the SCO thin films obtained under various deposition and post-deposition conditions were measured and the results obtained were used to further optimize the fabrication conditions of SCO thin film for enhancing its conductivity.

3.6.8 Van der Pauw setup

The Van der Pauw setup devised by L. J. van der Pauw in 1958 is used to measure the sheet resistance of conducting/semiconducting layer by making four Ohmic contacts on each corner of a square sample [146]. The electrical resistivity of the layer is then measured by multiplying the sheet resistance by the thickness of the layer. The Van der Pauw technique is also used for Hall measurements to calculate the charge carrier concentration density, Hall mobility and polarity of the charge carriers. The accuracy of measurement depends on the quality and size of the Ohmic contact and the uniformity of the conducting layers.

The four-point probe technique cannot determine the polarity of the charge carri-

ers of the semiconducting materials. Thus in order to determine polarity of the charge carriers in SCO thin film and verify the results of four-point probe measurement, we used the Van der Pauw measuring technique of electrical properties in our partner lab CIMAP of INP-Grenoble. This is very sensitive technique of measuring electrical properties and good ohmic contacts in a perfect square is very essential. Edward Auto 306 coating machine in LMGP was used to make gold ohmic contacts on four corners of 1 cm $\times$ 1 cm SCO thin film.

4

Materials and Methods

As discussed in the previous chapter, there are large number of thin-film deposition techniques. Each deposition technique has its own merits and demerits. Similarly, there are number of TCO thin-films recognized as p-type. Selection of thin film materials and its deposition technique requires a lot of considerations. Materials selection is based on its functionality, price, availability, stability and/or ecological factors etc. Likewise, selection of a deposition technique is based on its deposition efficiency, operational method, price and control of deposition parameters, etc. The main objective of this Ph.D research is to fabricate p-type TCO thin film. $SrCu_2O_2$ commonly known as SCO was chosen as a candidate material for this research study because of its large direct bandgap and low deposition temperature. Metal-Organic Chemical Vapor Deposition (MOCVD) technique was chosen for the fabrication of SCO as to our knowledge there was no report published on the synthesis of SCO by chemical method. Selection of MOCVD was also made because of its low price, high deposition rate, large area deposition facility and good control over the film's composition. We reported the deposition of SCO thin film by MOCVD for the first time in August, 2008. After this report, concentration was focused on the improvement of its optical and electrical properties, and on optimizing the deposition and post-deposition

parameters.

4.1 Thermodynamics of Sr-Cu-O system

In thin film fabrication, thermodynamics of the reactant materials and principle of the growth phenomenon are crucial to understand. Roth et al. studied phase equilibria of the SrO-CuO system and determined its phase diagram. Based on this phase diagram, they found three compounds Sr_2CuO_3, $SrCuO_2$ and $Sr_{14}Cu_{24}O_{41}$ out of this SrO-CuO system [14]. Subsequently, C. B. Alcock and B. Li reported thermodynamic study of the Sr-Cu-O system and established the existence of $SrCu_2O_2$ phase along with Sr_2CuO_3, $SrCuO_2$ and $Sr_3Cu_5O_{8+z}$ with z around 0.6 [15]. Later on, $Sr_3Cu_5O_{8+z}$ was recognized as $Sr_{14}Cu_{24}O_{41}$ by the group of Suzuki [16]. The Cu_2O-SrO system was studied in different molar ratios sintered under purified argon at 1220 K and it was found that the ratio of Cu_2O:SrO = 1:1 results in $SrCu_2O_2$ phase. $SrCu_2O_2$ was also found to co-exist with Cu_2O when the Cu_2O/SrO ratio is greater than 1 and with SrO when the ratio is less than 1 [17]. The thermogravimetric study of $Sr_{14}Cu_{24}O_{41}$ was carried out by varying the oxygen contents and temperature. It was found that this compound is stable only at oxygen partial pressure greater than 6 kPa at 1193 K and decomposes into $SrCuO_2$ and CuO when the oxygen partial pressure is less than 6 kPa. The three different steps of decomposition were observed under 200 Pa oxygen partial pressure at 1193 K temperature. The first step corresponds to the decomposition $\frac{2}{3}Sr_{14}Cu_{24}O_{41} = \frac{28}{3}SrCuO_2 + \frac{20}{3}CuO + O_2$, in the second step, CuO decomposes into Cu_2O, i.e., $4CuO = 2Cu_2O + O_2$ and the third step leads to the formation of $SrCu_2O_2$, that is, $4SrCuO_2 + 2Cu_2O = 4SrCu_2O_2 + O_2$ [15, 16]. This final phase is the equilibrium phase under experimental conditions, however, the coexistence of $SrCuO_2$ and $SrCu_2O_2$ was also confirmed [15].

The lack of thermodynamic data as a function of temperature and oxygen partial pressure prevents us from predicting the stabilities and coexistence of various phases

[16]. The phase diagram, based on the work of Suzuki et al. shows the various Sr-Cu-O phase fields as a function of oxygen partial pressure and temperature for a fixed metals ratio of Cu/Sr = 2 as is appropriate for $SrCu_2O_2$ [10].

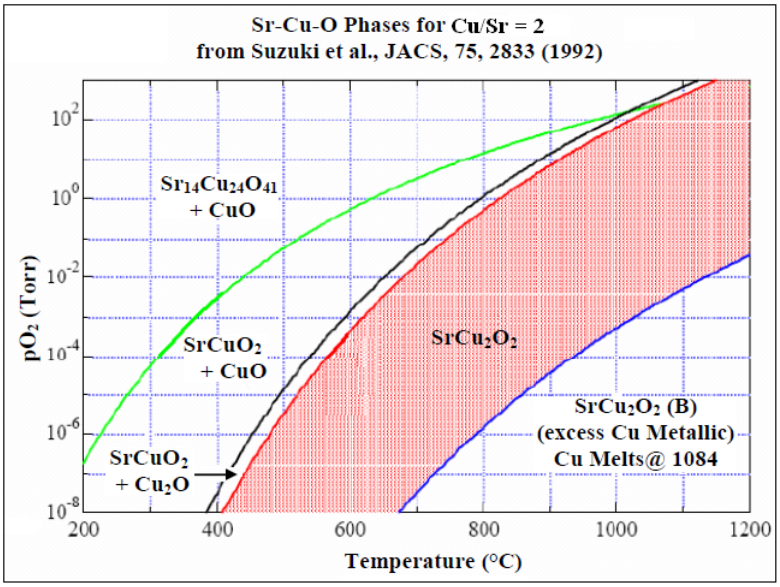

Figure 4.1: Phase diagram of Sr-Cu-O system. Variation in O_2 partial pressure and temperature gives rise to various chemical phases of strontium copper oxides. $SrCu_2O_2$ for $\frac{Cu}{Sr} = 2$ can be obtained at low temperature for low O_2 partial pressure and vice versa [10].

The phase diagram in figure 4.1 was constructed for Sr-Cu-O bulk materials annealed at various temperatures in reduced oxygen environment. However, Sr-Cu-O thin-films also follow the same phase transition with some deviation [18].

4.2 CVD Principle and Film Growth

CVD is a chemical process used to produce highly pure and high-performance solid state materials. The process is often used in semiconductor industry to produce thin films [147, 148]. CVD is a deposition process where chemical precursors are transported in the vapor phase to decompose on a preheated substrate to form a thin film [149]. In a typical CVD process, the substrate is exposed to one or more volatile

precursors, which react and/or decompose on the substrate surface to produce the desired thin-film [147]. The deposition reaction is generally either of thermal decomposition, oxidation or chemical reduction, in which case another reactant gas is added to the system. The substrate can also act as reductant, but only very thin films can be produced by this method [148]. The reactants transportation is achieved by carrier gases which can be either inert gases, like, N_2, He, or Ar, etc, or the reducing gases in the deposition reaction [11, 148] .

Modelling of the gas flow in the vicinity of the substrate introduces the concept of boundary layer [4]. As an object moves through a fluid, or as a fluid moves past over an object, the molecules of the fluid near the object are disturbed and move around the object. Aerodynamic forces are generated between the fluid and the object. Magnitude of these forces depend on shape of the object, speed of the fluid/object, mass of the fluid going by the object and on two other important properties of the fluid; viscosity or stickiness, and compressibility or springiness of the fluid. Aerodynamic forces depend in a complex way on the viscosity of the fluid. As the fluid moves past over the object, the molecules right next to the surface stick to the surface. The molecules just above the surface are slowed down in their collisions with the molecules sticking to the surface. These molecules in turn slow down the flow just above them. The farther one moves unaffected due to no or fewer collisions by the object surface. This creates a thin layer of fluid near the surface in which the velocity changes from zero at the surface, to the free stream value away from the surface. This layer is commonly referred to as "boundary layer" because it occurs on the boundary of the fluid and the object [150].

The CVD process completely takes place inside the boundary layer. The figure 4.2 describes the key steps involved in CVD process [11].

These various steps in CVD can be explained in the following way:

1. Transport of precursor vapors towards the boundary layer

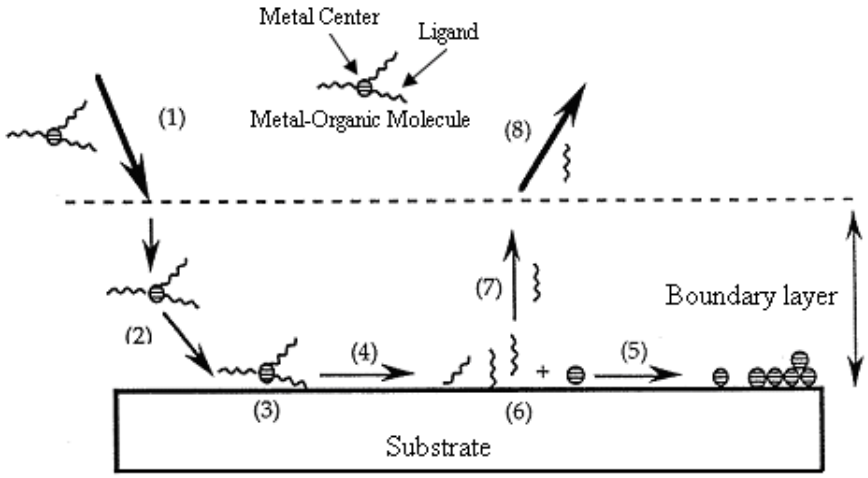

Figure 4.2: Sequence of stages involved in vapor phase chemical deposition of thin film [4].

2. Diffusion of the precursor molecules through the boundary layer
3. Adsorption of molecules on the substrate surface
4. Decomposition of molecules
5. Diffusion of the atoms on the surface and fixing on a site of nucleation or growth of the film
6. At the same time, desorption of the by-products of the reaction in step (4)
7. Exit of the by-products through the boundary layer
8. Evacuation of the by-products

During chemical vapor deposition, the growth rate of the film is limited by either reaction kinetics on the substrate surface, mass transport of the reactants to the substrate and of by-products out of the boundary layer or the feed rate of precursors [149]. It is the slowest of these three, which determine the rate of deposition [4]. Reaction kinetics on the substrate surface depends on the substrate temperature (lower the temperature,

slower is the reaction and vice versa). The mass transport to or out of the substrate is controlled by thickness of the boundary layer (thicker the boundary layer, slower is the diffusion and vice versa). Thickness of the boundary layer in turn depends on the inside chamber pressure (higher the pressure, thicker is the boundary layer and vice versa). The feed rate limits the rate of deposition when nearly all the reactants are consumed in the chamber. The feed rate is important for hot wall reactors, since the heated walls decompose a large amount of precursor. Cold wall reactors tend to have higher deposition rate, since the reactants are not depleted by the walls [149].

The transport of reactants to the surface of the substrate not only depends on the thickness of boundary layer but also on the coefficient of diffusion of the reactive species. Once the reactive species adsorb on the surface, the reactions which take place are determined by the laws of chemical thermodynamics. The quality of deposition results from their respective kinetics [4].

A plot of the growth rate (in logarithmic scale) versus inverse substrate temperature, knowns Arrhenius plot, can be used to determine rate limiting steps of the growth process [4].

Three limiting growth modes are distinguished.

- At lowest temperatures, the deposition rate is limited by kinetics of surface reactions (region I). These reactions being thermally activated, the deposition rate strongly increases with temperature.
- Beyond a critical temperature, kinetics of the reactions becomes faster than reactants collection on the substrate surface. The limiting factor is then the diffusion of active species through the boundary layer, which depends little on the temperature. The limiting factors in this region (region II) are the mass transport and feed-rate. The feed-rate limited reactions are independent of temperature.
- When temperature is increased further (region III), a fall in the deposition rate

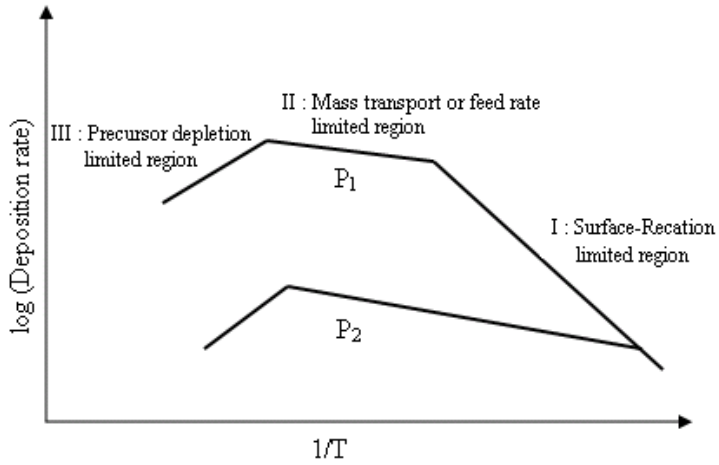

Figure 4.3: Dependence of CVD deposition rate on temperature and pressure (P_1<P_2). Growth rate increases in the surface reaction region, remains almost constant in mass transport region, and decreases in precursor depletion region [4].

is observed. The origin of this fall is the decomposition of precursor by the very hot walls of the reactor and the gas phase particle formation which depletes the reactant concentration.

Each one of these (regions I, II and III) growth modes has advantages and disadvantages. For example, deposition at high temperature results in pure and well crystallized films. However, the deposition yield is not satisfactory (depletion mode). The diffusional mode gives rise to high growth rate, due to which the deposition time is greatly reduced. Moreover, this mode is not very sensitive to temperature fluctuations. Deposition at low temperature yields a film of homogeneous thickness and good conformity [4].

Like temperature, the pressure too has a notable influence on the deposition rate. When the pressure decreases, the coefficient of diffusion of the reactant species increases, which makes it possible to reach a higher growth rate (*cf* figure 4.3). Moreover, it extends the domain over which the growth is controlled by the kinetics of reaction [4]. The effect of reactant concentrations on the deposition rate is demonstrated

in the figure 4.4 [11, 149].

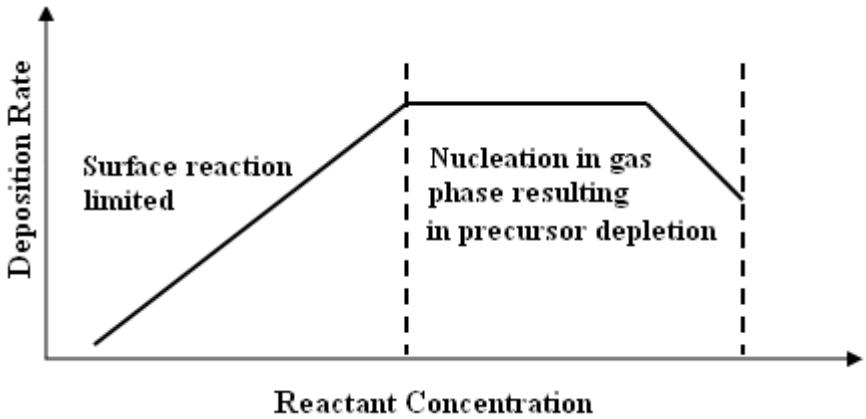

Figure 4.4: Dependence of CVD deposition rate on reactant concentration. Increase in reactant concentration increases the deposition rate till the precursor depletion occurs due to gas phase nucleation [11]

Increase in reactant concentration increases the deposition rate. However, at very high reactant concentrations, the gas phase nucleation will occur and the growth rate will drop [149].

Slow deposition in a CVD reactor can often be attributed to either gas phase nucleation, precursor depletion due to hot walls, thick boundary layer formation, low temperature, or low precursor vapor pressure [149].

4.3 Structure of CVD Deposits

CVD deposits are formed by nucleation and growth mechanism. Nucleation is preceded by the adsorption and diffusion of atoms on the surface of the substrate. Modern nucleation theory “Evaporation and Condensation” [151] has been shown to be applicable to chemical vapor deposition. Stable nuclei (consisting of few atoms) are formed at preferred sites on the substrate surface. Their growth proceeds by the addition of individual atoms both directly from the reactant gas stream and from the

surface diffusion of the substrate. Addition of atoms during this growth process generally occur at positions of lowest free energy and proceed to from crystallites [148].

Nature of the substrate surface can have a profound effect on structure of the deposits formed upon it. The resulting deposits may be amorphous, single or polycrystalline depending upon the nature of substrate materials, their crystal orientation and deposition parameters. Amorphous deposits are mainly obtained at low temperatures when the adsorbed molecules bears no structural relation with the substrate molecules, otherwise the adsorbed molecules nucleate and grow in preferred orientations which leads to crystalline structures.

Nucleation and growth of any structure of the CVD deposits on the substrate surface depend on two major factors: the supersaturation, which is related to the concentration of the adsorbed reactants species on the substrate surface and the temperature which affect their mobility. The supersaturation can be defined as the ratio of the reactant species to the equilibrium vapor pressure. The general effects of supersaturation and temperature on the structure of the materials are shown in the figure 4.5 [12].

Figure 4.5: The effects of supersaturation and temperature on the structure of CVD deposits. Change in supersaturation and substrate temperature yield amorphous to epitaxial films [12].

Since most of the CVD reactions are endothermic, the supersaturation increases with temperature. This implies that there is a possibility of reversal of the structure forms shown in the figure 4.5 [12]. Despite the complications of CVD and the limitations of quantitative interpretation, the trends shown in figure 4.5 are useful in pre-

dicting the effect of temperature, pressure, and reactant composition on the structure of CVD materials. [12].

Polycrystalline grain structure possess a high degree of preferred orientations. The preferred orientation develops in the absence of epitaxy. The degree of preferred orientation depends upon the process variables and choice of the reactant species. In the absence of randomly oriented layers, preferentially oriented deposits exhibit considerable resistance to grain growth. Further resistance to grain growth in such structure is also provided by grain-boundary, voids, or gas-containing bubbles. These voids or bubbles are formed as a result of agglomeration of atomic or molecular sized impurities [148].

Epitaxial films are the monocrystalline films deposited on monocrystalline substrates. An epitaxial film may be homo- or heteroepitaxial. A homoepitaxial film is of the same materials as those of the substrate, while in case of heteroepitaxial film, the substrate materials are different from the film. However, there must exist no or minimum lattice mismatch (<14%) between substrate and coating material [148]. According to the conditions depicted in figure 4.5, an epitaxial film can only be grown at very low supersaturation and at very high temperature [12], beacause, as the supersaturation is increased, the nucleation rate of other orientations becomes sufficiently great and the epitaxial ralation is lost [148].

4.4 Types of CVD Reactors

Chemical vapor deposition is carried out in various types of reactors depending upon the nature of the coating materials, required film properties (thickness, morphology, uniformity, etc), nature of film growth (amorphous, mono- or poly-crystalline, or epitaxial), rate of deposition, or nature of the substrate material. These various CVD reactors include; Thermal, Plasma-enhanced, Photochemical CVD reactors, etc

[149, 152].

4.4.1 Thermal CVD Reactor

In thermal CVD reactors high temperature is used to decompose the precursor molecules. Heating is normally accomplished by use of resistive heating, radio frequency induction heating, or radiant heating. There are two basic types of reactors for thermal CVD: the hot-wall reactor and the cold-wall reactor, according to the reactor's wall temperature relative to the substrate temperature [148, 149].

- Hot-wall reactors are mostly used in research laboratories for metal oxides deposition [11]. A hot-wall reactor is an isothermal furnace holding the substrates. Hot-wall reactors are large in size and are capable of deposition on several substrates simultaneously. Since the whole chamber is equally heated, precise temperature control can be achieved with correct furnace design [149]. The size and shape of the hot-wall CVD chamber relative to the size and shape of substrate is of typical importance. If size of the chamber is much larger than the size of the substrate, a lot of reactants will pass through the chamber without being reacted. Similarly, if the chamber is too small, a low velocity gas stream may be prematurely depleted of reactants and thereby cause formation of films with uneven thickness. The shape of the chamber is made best similar to that of the substrate (or its susceptor), especially where the distance of separation is not too large. This precaution provides a comparable gas flow pattern over all portions of the substrate and thus helps in the growth of films with uniform thickness and microstructure [148]. Hot-wall CVD systems are simple to operate, can be operated under a range of pressures and temperatures, and allow different orientations of the substrate relative to the gas flow [11]. The disadvantage of hot-wall reactor is the simultaneous deposition on the substrates as well as on the walls. As a consequence, hot-wall reactors must be frequently cleaned to reduce flaking of

particles from the walls that contaminate the substrate. In addition, a correspondingly large amount of precursor is consumed due to reactants depletion by the hot-wall decomposition, which also results in low deposition rate [11, 148, 149].

- Cold-wall reactors are mostly used in industries for the films growth on a single substrate in various orientation to the gas flow [11]. In cold-wall reactor only the substrate is heated by induction or radiant heating. Since most CVD reactions are endothermic, so deposition is preferentially on the area of highest temperature. As a result, deposition is only on the substrate and the cold reactor walls stay clean [149]. Cold-wall reactors result in no or less contamination of the substrate due to their clean walls and high deposition rate due to no or less precursor depletion by the reactor walls [11,148,149]. However, cold-wall methods of heating are not applicable to all systems because of the size, shape and composition of the substrate. For example, resistive heating of the substrate is limited to highly electrical resistive substrates of relatively small cross-sectional areas. Similarly, inductive heating cannot be applied to substrates which are either thermal insulators or semiconductors. Temperature control is also a quite difficult task in cold-wall configuration [148]. Due to single substrate deposition, cold-wall reactors have less throughput compared to hot-wall reactors where simultaneous deposition on multiple substrate is possible [149].

A further subdivision in reactor design occurs between vertical and horizontal reactors. In vertical reactor, the direction of gas flow is vertical and the plane of deposition is normal to it, while in the horizontal reactor, both the flow and the plane are horizontal. In a hybrid design, termed as barrel reactor, gas flow is vertical and parallel to the plane of deposition. There is some evidence that film thickness is less variable in horizontal reactor compared to the vertical one [148]. Another type of reactor uses rotating substrate holder to deposit thin films with unifrom thickness [153].

4.4.2 Plasma-enhanced CVD Reactor

Plasma-enhanced CVD (PECVD) or some times called plasma-assisted CVD (PACVD) is used to deposit films at much lower temperature compared to thermal CVD [149]. Other advantages include deposition of non-equilibrium phases, better control of stoichiometry, purity of deposits [154], and greater film uniformity due to low pressure for sustaining plasma [149]. Most plasmas used for PECVD are generated by RF-electric filed. In higher frequency electric field, the light electrons, compared to heavy ions of plasma are quickly accelerated by the field with no effect on the plasma temperature because of their low mass [149]. These highly accelerated electron are then used for bond breaking of the precursor molecules to form highly reactive free radicals. The desired deposition on the given substrate is thus possible at much lower temperature than conventional thermal CVD [154]. The so formed reactive species in plasma have lower activation energies for chemical reactions and usually have higher sticking coefficient to the substrate [149]. Disadvantage of PECVD is the damage of some films due to ion bombardment from the plasma [149].

4.4.3 Photo-chemical CVD Reactor

Photo-chemical CVD uses energy of photons to initiate the chemical reactions. Photodissociation of the chemical precursor involves absorption of one or more photons resulting in breaking of the chemical bonds. There are two basic configurations for photo-chemical CVD. The first method uses a laser primarily as localized heat source and the second method uses high energy photons to decompose the reactants on or near the substrate surface [149]. Photochemical effect can be induced by a laser if the precursor molecules can be dissociated by laser, otherwise UV photons have sufficient energy to break the bonds in the precursor chemicals. Laser-assisted CVD (LACVD) usually uses eximer laser to provide high energy UV photons to break the bonds of precursor molecules. The main advantage of the LACVD is that nearly no heat is re-

quired for the deposition of high quality films [149]. A UV-assisted CVD reactor is used to improve adhesion, hardness and thermal stability of the organic polymer thin films [143].

4.5 Metal-Organic CVD (MOCVD)

Metal-Organic CVD commonly known as MOCVD uses metalorganic compounds as a source material for thin film growth. The term metal-organic has been used to broadly cover compounds with metal-carbon bonds, metal-oxygen-carbon bonds, and the coordination compounds of metals and organic molecules. As the knowledge of molecular architecture improves, the combination of metals with organic molecules seems to offer possible solutions to many problems in metal extraction and purification, in formulation of heat-resistant polymers, in propellant systems, surface coatings, agricultural chemicals, and chemical synthesis [155]. The attractive properties of materials derived from metal-organic precursors generally include high purity, molecular level homogeneity in multicomponent materials, submicron particle size (typically 20 to 50 Å), high reactivity and surface area, and lower processing temperatures [156]. The optimal thermal decomposition of metalorganic compounds varies between 300 and 500 °C [157].

MOCVD is an improvement over conventional VPE (Vapor Phase Epitaxy) and LPE (Liquid Phase Epitaxy) for the epitaxial growth of compound semiconductor thin films [158]. Since its introduction in 1968, this technique has been established as one of the techniques for epitaxial growth of compound semiconductors both for research and production [159]. For the growth of metal oxide thin-films, MOCVD offers the attraction of simple apparatus, conformal coverage, growth under high gaseous partial pressure and adaptability to large area deposition [160]. The use of metalorganic compounds is advantageous in a sense that they are volatile at moderately low temperature as compared to metal halides for example. Since all constituents are in the vapor phase,

precise electronic control of gas flow rates and partial pressures is possible [159].

Modern techniques of organic chemistry allow to prepare metal-organic compounds of practically every metallic element [161]. The application of MOCVD for the fabrication of Cu-based thin films has proven a viable route to various phases with different metal oxidation state. Previous studies have demonstrated that nature of the phase formed in MOCVD experiment critically depends upon substrate temperature as well as on oxygen partial pressure and concentration of metallic reactants in the CVD reactor [162].

MOCVD offers many recognized advantages over other deposition techniques, however, several problems remain in the formation of high quality devices. Chief among these is the problem of obtaining good uniformity of deposition along the upper surface of the substrate. The problem of nonuniform thickness can be greatly reducing by deposition on a rotating substrate [163].

Metal-Organic Precursor:

In chemistry, a coordination compound is a structure consisting of a central atom or ion (usually metallic) bonded to a surrounding array of molecules or anions (ligands). The atom within a ligand that is directly bonded to the central atom or ion is called the donor atom. A ligand donates at least one pair of electrons to the central atom/ion. Coordination refers to the coordinate covalent bonds between the ligands and the central atom. A coordination structure is described by its coordination number, the number of ligands attached to the metal (more specifically, the number of σ-type bonds between ligand(s) and the central atom). The number of bonds depends on size, charge, and electronic configuration of the metal ion and the ligands. Coordination number is normally between two and nine, but large numbers of ligands are not uncommon for the lanthanides and actinides [164].

The coordination compounds in which ligands are organic or organic-like and the central atoms/ions are metals, are known as metalorganic compounds [164]. Volatile metalorganic compounds are decomposed on heated surfaces to form semiconducting thin films [165]. Ultrapure metalorganic compounds are required for many optoelectronic and microelectronic applications (e.g. MOCVD and Atomic Layer Deposition) with highest purity of the order of 99.9999% or greater. The vapour pressure of a metalorganic precursor is a crucial parameter that governs the concentrations of metalorganic precursors entering the reactor, and subsequently the rate of deposition [166].

4.6 MOCVD system at LMGP

Research at LMGP (Laboratory of Materials and Physical Engineering) is dedicated to material sciences and is concentrated on studies related to intrinsic properties of materials, their structure and the processing of crystals or thin films for applications in the fields of Information Technologies, Energy or Health. MOCVD apparatus used for the growth of SCO thin film at LMGP during this thesis research is provided by JIPELEC, a partner of France based Qualiflow Therm group. It is specialized in designing thermal equipments for the industry of semiconductor and advanced materials. A schematic diagram of MOCVD system is shown in the figure 4.6.

This apparatus is provided with an injecting system based on the principle of liquid delivery called injection CVD and uses a micro valve injector to deliver liquid precursor into the evaporator. The injector is capable of delivering the liquid precursor into the evaporator either in continuous or in discrete micro-droplet pulses. The evaporator is maintained at predetermined sufficient high temperature to evaporate the injected liquid in a flash. The evaporator is connected to Ar supply line to deliver precursor vapors to the reactor. On the way from the evaporator to the reactor these vapors pass through a hot line maintained at the same temperature as that of the evaporator so as to avoid the condensation of precursor vapors on the walls of delivery line. Tem-

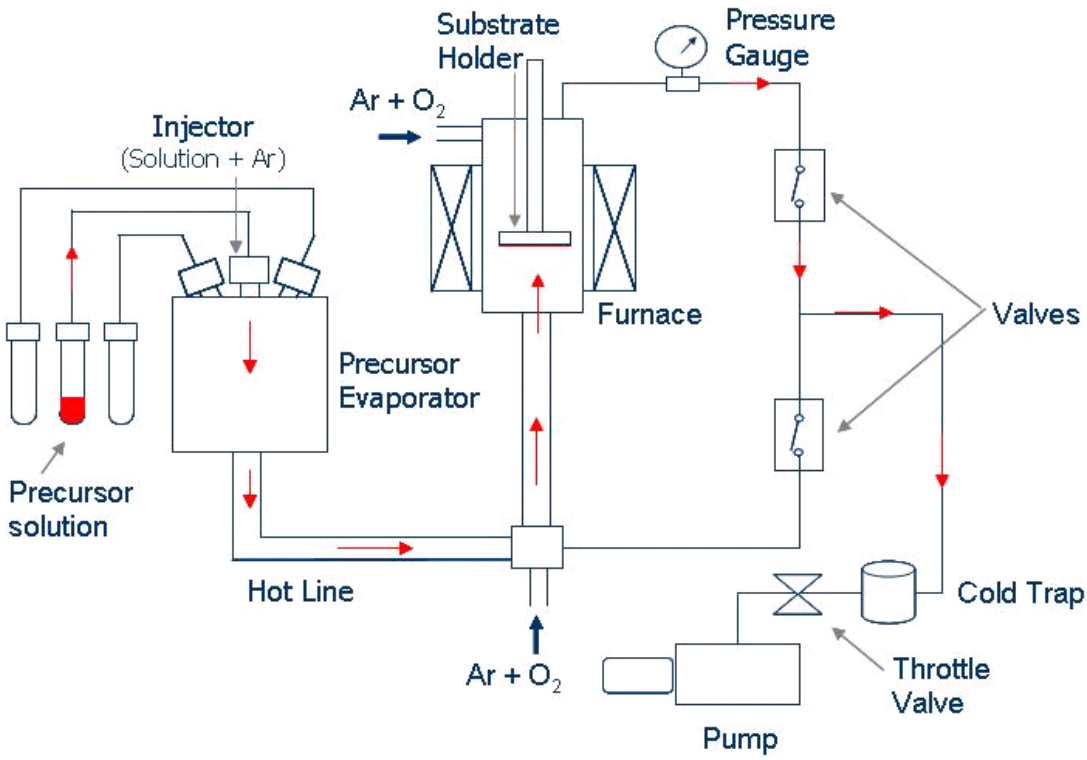

Figure 4.6: Schematic diagram of MOCVD deposition system in LMGP for thin film deposition.

perature of the evaporator and/or of the hot line must not be so high to decompose the precursor vapors there. A mixture of O_2 and Ar gas is allowed to enter the hot line to push the precursor vapors into the reactor. Here, Ar is used as carrier gas and O_2 as reaction gas. Precursor vapors along with O_2 enter the predetermined heated reactor, where precursor vapors are decomposed and deposited on the hot substrate to form oxidized deposits. This is a vertical hot-wall reactor and is heated by high resistive heating along with the substrate holder. By-products of the reaction are pumped out from the reactor and collected in cold vessel maintained at low temperature by liquid nitrogen. Due to the toxicity of the by-products trapping by condensation is necessary in order to avoid their leakage to the outside atmosphere during pumping out from the reactor. The gas lines are provided with control valves to maintain desired pressure inside the reactor, to change O_2 partial pressure in the reactor, and to determine direction

of the gas flow during heating, deposition, and cooling processes.

Characteristics of the deposition (growth rate, thickness, composition, morphology and structure) are controlled by:

- The nature of solution (precursor, solvent, and concentration)
- The sequence of injection (duration and frequency of opening of the injector, pressurization of the precursor containing tube, and the total number of injections)
- The temperature of substrate and evaporator
- The total pressure inside the reactor
- The oxygen partial pressure in the reactor
- The nature of the reaction/carrier gases

These parameters make this system very flexible for use. However, a large number of trial experiments are necessary to optimise them for a good quality growth ranging from amorphous to epitaxial.

4.6.1 Microvalve Injector

Precursor evaporator kept under vacuum is connected through microvalve injector to the tube containing the precursor solution. Precursor solution is pressurized by an inert gas Ar to ensure liquid delivery of precursor to the evaporator through opening of injector microvalve. Opening of the injector valve is controlled by a computer program to attain the desired delivery of precursor. Duration and frequency of injector valve opening is determined by computer through an injection software. Opening time of the injector must be kept very short so as to insure delivery of small microdroplets into the evaporator. Connection of injector to evaporator is made in such a way that only the injector nozzle is inside the evaporator while most of its remaining part is

outside and is kept cold by continuous circulation of water through it. Cooling of injector is important to keep the liquid precursor from evaporation before reaching the evaporator and keeping the injection rate under control. Figure 4.7 shows the injector and precursor solution containing tube assembly along with the image of microdroplets coming out of the injector nozzle.

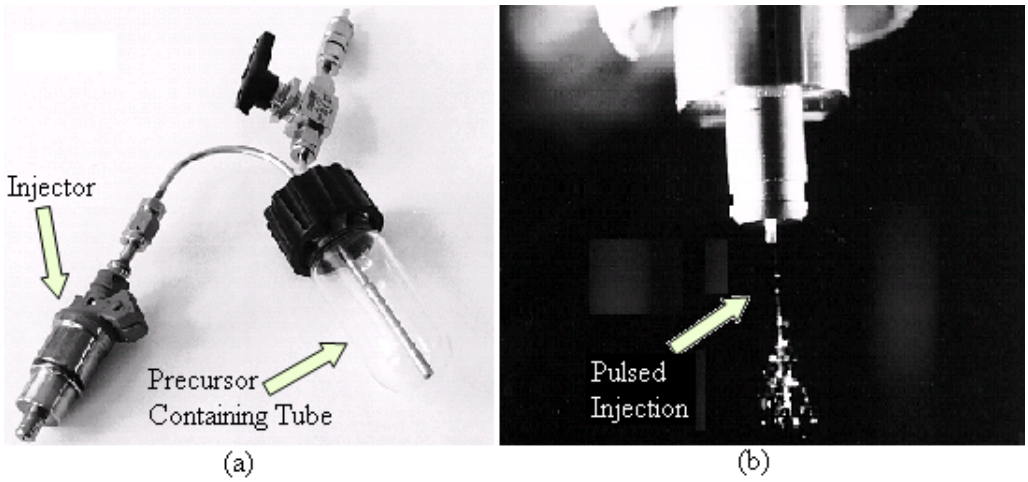

Figure 4.7: a) Image of the injector and precursor container assembly, b) Image of the micro droplets in the evaporator after injection

This innovative device for introducing precursors into the reaction chamber has been the subject of a French patent in 1993 [167], European patent in 1994 [168] and US patent in 1999 [169] by a research group in LMGP. It has many advantages. Precursors are kept in a neutral environment outside the evaporation and reaction zone so that they are not effected by reactions gases or by excessive heat. In case of multicomponent precursors where each component material is not possible to dissolve in the same solvent, the way out is to dissolve each component material in their respective solvent and inject simultaneously into the evaporation chamber using multiple injectors and precursor containers (*cf.* figure 4.8). In this way, a multilayer deposition is also an easy task by just determining the sequence of precursors injection into the reactor. This sequence of injection must take account of the deposition parameters, properties

of reactant materials, and the desired multilayer. In order to have a smooth injection rate, it is imperative to use clean solution without any colloidal undissolved particles. The injector has to be cleaned after each deposition to remove any sort of particles trapped in the injector nozzle.

4.6.2 Evaporator and Delivery Line

The evaporator is a vacuum chamber kept at high temperature at least comparable to the evaporation temperature of the precursor solution. To be more careful the temperature of evaporator is kept higher than the evaporation temperature of the precursor solution but lower than the precursor decomposition temperature so as to avoid the premature decomposition of precursor molecules inside the evaporation chamber. The evaporator and the delivery line to the reactor are practically kept at the same high temperature to avoid the condensation of precursor solution vapors on the wall of delivery line. Temperature of the reactor is kept higher than that of the evaporator and delivery line. The evaporation chamber is kept under constant vacuum (low pressure) and the tube containing precursor solution under constant high pressure so that a constant pressure gradient enables unifrom delivery of liquid precursor to the evaporation chamber.

4.6.3 Process Reactor

Precursor vapors coming out of the evaporator are directed to reactor through the delivery line as shown in the figure 4.8.

The reactor shown in figure 4.8 is a vertical type MOCVD reactor, in which the precursor vapors are transported vertically upwards and the substrate is held normal to it. This arrangement helps in reducing the contamination of substrate by falling the flaking of particles from the reactor walls. The substrate is conductively heated by the substrate holder and convectionally by the reactor walls. Reactor walls are heated

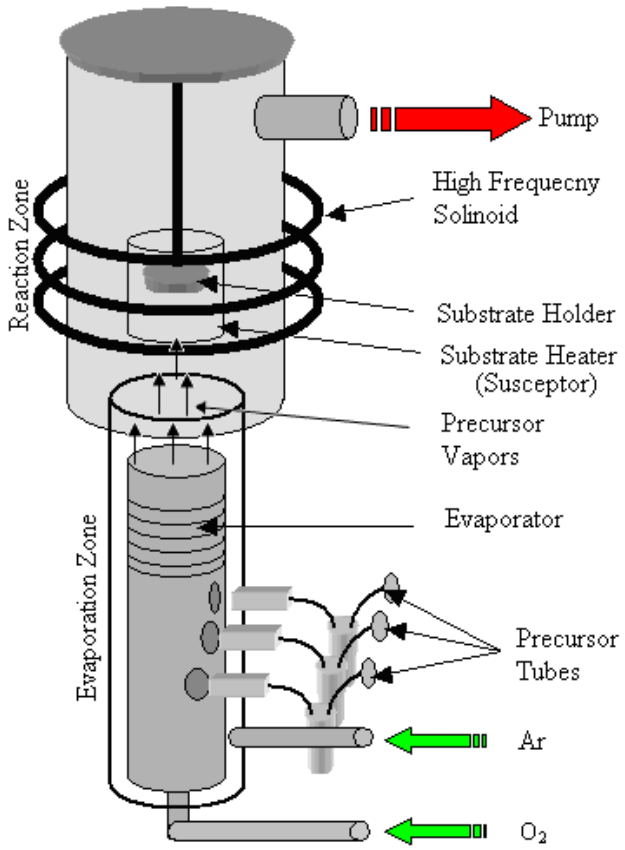

Figure 4.8: Evaporation and reaction zones of the MOCVD system in LMGP

to almost the same temperature by resistive heating. Temperature inside the reactor is maintained at such high value to decompose the precursor vapors near to or on the substrate surface. Total pressure inside the reactor is contributed by precursor vapors, carrier and reaction gases, and the by-product of the precursor decomposition reaction. A predetermined specific pressure is maintained inside the reactor by controlling the precursor feed rate, gases flux, and pumping out the reaction by-products. Pressure and temperature both have a dominant effect on the phase and nature of the growth as explained by John Blocher [12]. In order to avoid the contamination of substrate, a reverse gas flow is allowed during heating and cooling of the substrate before and after deposition.

4.6.4 Precursor Solution Preparation

Metalorganic precursor in liquid form was prepared by dissolving Tetramethyl-heptanedionate (tmhd) organic powder of 99% pure $Cu(tmhd)_2$, 99.99% of $Sr(tmhd)_2$ triglyme adduct in 99% pure m-xylene (C_8H_{10}) in a range of Cu to Sr ratios. Small percentages of 99.99% pure $Ba(tmhd)_2$ from 5 to 15% was also added to the precursor as dopant.

Precursor: Tetramethyl-heptanedionate $(tmhd)_2$ - Cu $(C_{11}H_{19}O_2)_2$
- Sr $(C_{11}H_{19}O_2)_2$
- Ba $(C_{11}H_{19}O_2)_2$

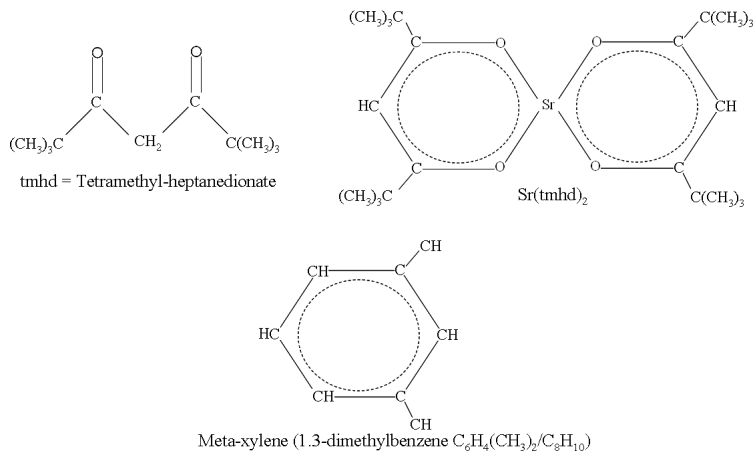

Figure 4.9: Organic chemical structure of precursors and solvent

From the known molar masses of Cu $(tmhd)_2$ = 430.096 g/mol, $Sr(tmhd)_2$ trig = 632.39 g/mol and Ba $(tmhd)_2$ = 503.877 g/mol, their concentration (molarity) was calculated and the solution was prepared by dissolving their corresponding masses in 15 ml of m-xylene. The solution was kept on stirring till no colloidal particles were visible in the solution. This normally takes one hours, but to be more careful the

solution was kept on stirring during the night and was then used for deposition in the morning.

4.6.5 Deposition Parameters

Properties of the thin film and the type of its growth depends rigorously on the nature of substrate and its temperature. Therefore, depositions on various substrates such as Si, Ge, YSZ, and glass were performed in the temperature range 400-650 °C. Evaporation temperature of m-xylene is 139 °C, therefore temperature of the evaporator and that of the delivery line was maintained at 280 °C. The deposition was carried out with pulsed injection of liquid precursor at 1.1 Hz frequency and 1.9 ms opening time of the injector. This corresponds to the injection of 15ml solution in 70 minutes with an average injection rate of 3.5×10^{-3}ml/s. Deposition was performed in an O_2, Ar atmosphere. The total pressure inside the deposition reactor was maintained at 5 torr. Depositions were carried out at constant 5 torr pressure with various percentages of O_2 partial pressure to Ar, ranging from 10 to 70%. The effects of these various deposition parameters will be discussed in details in the next chapter.

5

Results and Discussion

THIS PhD research work was carried out as a part of a European project NATCO (Novel Advanced Transparent Conducting Oxides). The NATCO project was financed by European Commission and technically supported by seven European partners (4 academia and 3 industries) from France, Belgium, Greece, Hungary and Ireland. The job of LMGP of the Grenoble Institute of Technology, France as a partner of the NATCO project was the fabrication of Ba-doped SCO thin-film by MOCVD. I joined this project as a Ph.D student in 2007. At the beginning large number of experimental trials were devoted to obtain Cu/Sr = 2 in the films as the aim was to grow a thin film of pure $SrCu_2O_2$ phase. However, the Cu/Sr ratio in the film not only depends on the ratio of Cu to Sr concentration in the precursor solution, but also on the deposition temperature and oxygen partial pressure in the reactor. The as-deposited films were always composed of strontium carbonates ($SrCO_3$) and copper oxides (CuO). In order to decompose the strontium carbonates, to crystallize the film, and to obtain pure SCO phase, the films were annealed in various gaseous environments at various temperatures for various durations. Along with decomposition of strontium carbonates and crystallization of the film, the variation in Cu to Sr ratio was also observed after annealing. Therefore, Cu to Sr ratio in the solution was adjusted according to the

deposition and post-deposition annealing conditions to obtain pure SCO phase in the film. Annealing effect on the morphology of the film was also observed in the form of grain sintering and cracks. Optoelectrical properties of the undoped SCO were tried to measure and compare with those of 5, 10 and 15% Ba-doped SCO, but no remarkable effect of Ba doping was noticed due to the reproducibility problem in the annealing conditions and Ba contamination in the depostion reactor.

5.1 As-deposited Films and their Characterizations

Films just after their deposition were characterized by Energy Dispersive X-ray (EDX) and Wavelength Dispersive X-ray (WDX) analysis for elemental composition and spatial compositional uniformity. The morphology and thickness was measured by SEM, the visual aspect by optical microscope and the naked eye appearance was pictured with a digital camera. Phase identification was done by XRD, FTIR and Raman spectroscopy. The adhesion strength of the film to the substrate was measured by scotch-tape test. The detail of all the above mentioned characterizations are given in the following subsections.

5.1.1 Visual Aspect

Deposition of SCO at 300 °C by PLD had been reported by Kudo et al. in 1998 [3]. Therefore, we started deposition of SCO by MOCVD at lower temperatures as 300 °C, but only a dark narrow strip appears at the border of circular Si substrate at deposition temperatures $\leq$ 400 °C as shown in figure 5.1 (a). Reason of such such behavior may be the temperature gradient between the center and border of the substrate induced by the hot wall configuration. Deposition at temperatures $\geq$ 450 °C [figure 5.1 (b)] give rise to smooth shiny films covering the whole substrate. However, deposition at temperatures $\geq$ 570 °C [figure 5.1 (c)] yields rough and diffusive films which may be attributed to the grain aggregates observed in SEM images (figure 5.2) for high

temperature deposited films. Films deposited at temperatures $\geq$ 570 °C also show less adherence to the substrate.

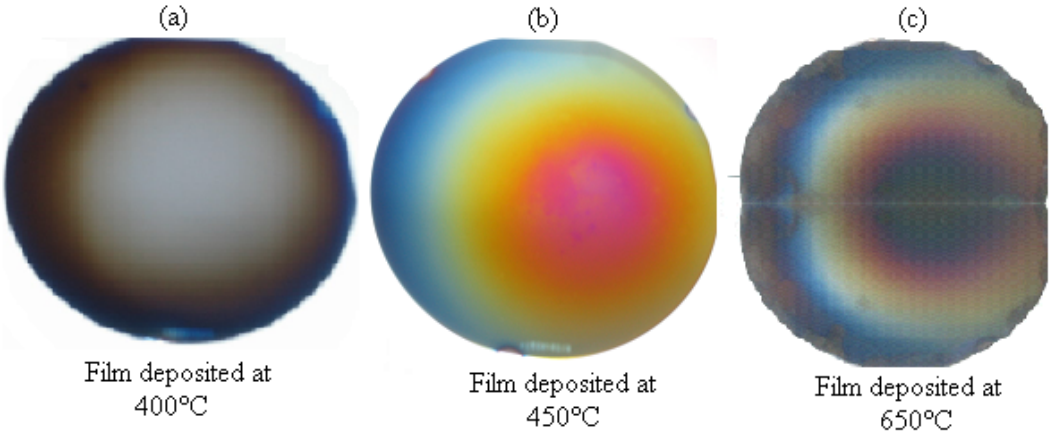

Figure 5.1: Digital camera images of the films deposited at various temperatures. Image (a) corresponds to lower deposition temperature yielding only a dark strip at the border, image (b) represents film deposited at high temperature, and image (c) corresponds to higher temperature of deposition film showing a rough and diffusive visual aspect

5.1.2 Morphological Characterization

Morphology of the films deposited at various temperatures (480-570 °C) was analyzed by SEM (Philips XL-30). SEM images of the film's surface given in figure 5.2 show very uniform morphology with uniform grain sizes.

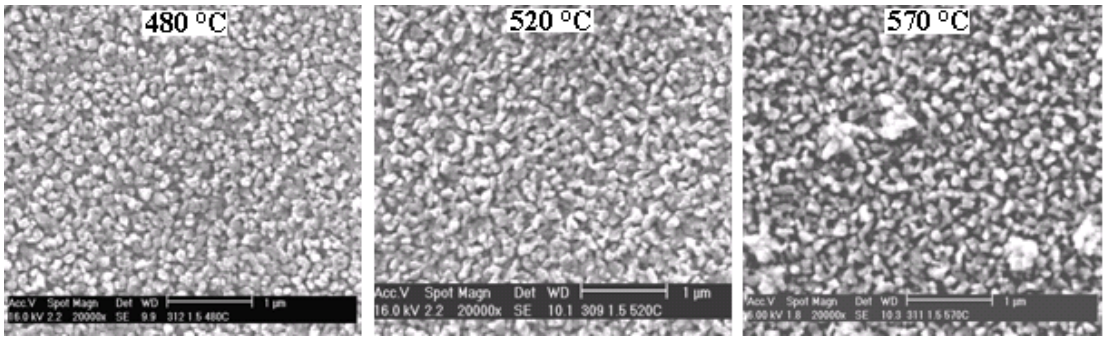

Figure 5.2: Comparison of SEM images of films deposited at various temperatures. Films deposited at higher temperature shows diffusive aspect due to formation of aggregates of grains

It can, however, be noted that film deposited at 570 °C shows some aggregates of grains which might be responsible for the diffuse visual aspect of the film as was obvious [figure 5.1(c)] for the films deposited at higher temperatures.

Film thickness and grain size were measured by another high resolution field emission gun (FEG) scanning electron microscope (Hitachi S-4500) at LMGP. The grain size varies between 50-200 nm (approximately) and the approximate thickness is 200-300 nm for a 15 ml precursor solution inject at an average rate of 3.5x10^{-3}ml/s in 70 minutes approximately at 520 °C as shown in the figure 5.3.

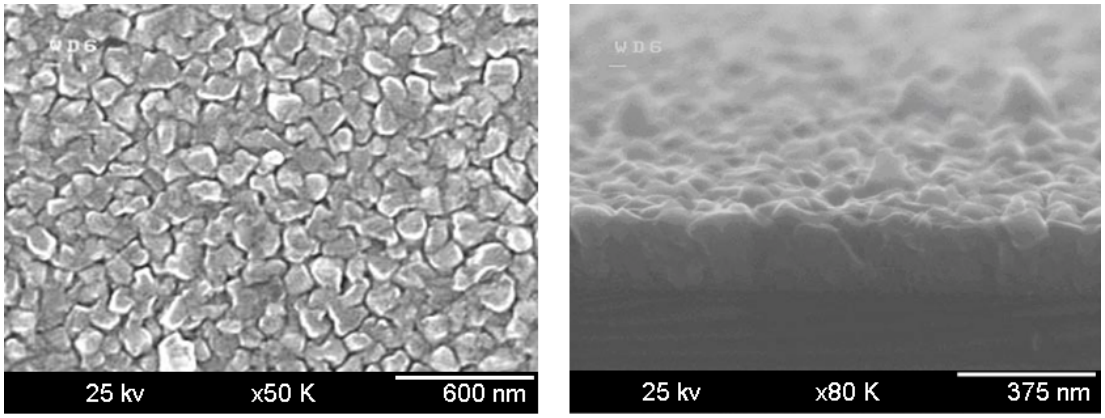

Figure 5.3: SEM-FEG high resolution images of the film for thickness and grain size measurements

5.1.3 Elemental Analysis

Precursor solution was prepared by dissolving Cu and Sr in m-xylene to obtain $SrCu_2O_2$ phase in the film, where Cu/Sr = 2. Keeping this point in mind, Cu and Sr were dissolved with a concentration Cu = 2Sr in m-xylene. However, the deposition efficiency of Cu is much higher than Sr and films deposited with Cu/Sr = 2 in solution always give higher Cu/Sr ratio in the films deposited at low temperatures. Deposition efficiency of Sr increases with the increase in deposition temperature. Therefore, in order to have Cu/Sr = 2 in the film, higher concentrations of Sr relative to Cu were tried at higher temperatures. The Cu/Sr ratios in the film were plotted against those in

the solution and the results obtained are as give in the figure 5.4.

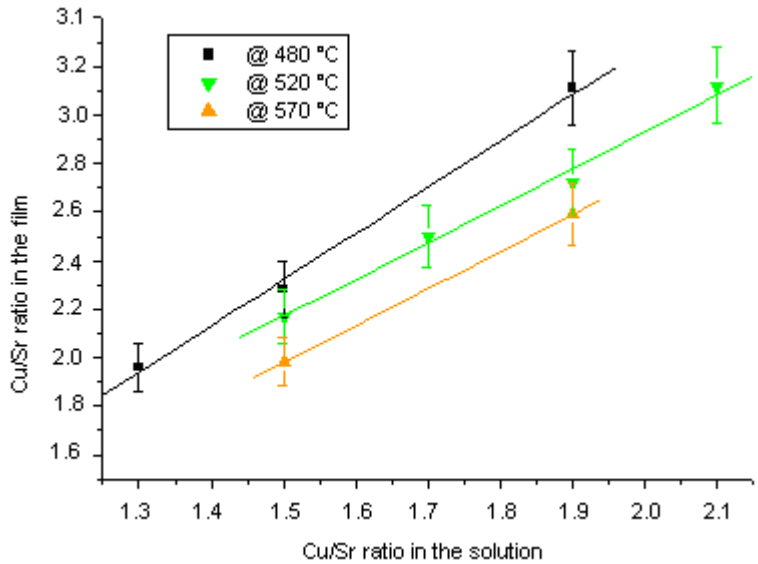

Figure 5.4: The Cu to Sr ratios at different deposition temperatures in the film measured by WDX versus their molar ratios in the solution. The $\frac{Cu}{Sr}$ ratio in film decreases with the increase in temperature due to the increase of Sr content in the film

To have Cu/Sr = 2 in the film, solutions were prepared according to the data shown in figure 5.4. The Cu/Sr ratio in the film decreases with the increase in deposition temperature which indicate that higher deposition temperature promotes the deposition of Sr and vice versa.

Elemental compositions of the Cu and Sr, along with Ba as dopant at various deposition temperatures were analysed by WDX and almost the same behavior (as in figure 5.4) was found in a sense that higher deposition temperature increases Sr contents in the film. A plot of Cu/Sr+Ba (with 15% Ba) in the solution versus Cu/Sr in the film at various deposition temperature is given in figue 5.5.

From the comparison of figures 5.4 and 5.5, it can be established that for Cu/Sr = 2 in the Ba-doped films, Sr contents in the Ba containing precursor solution must be increased.

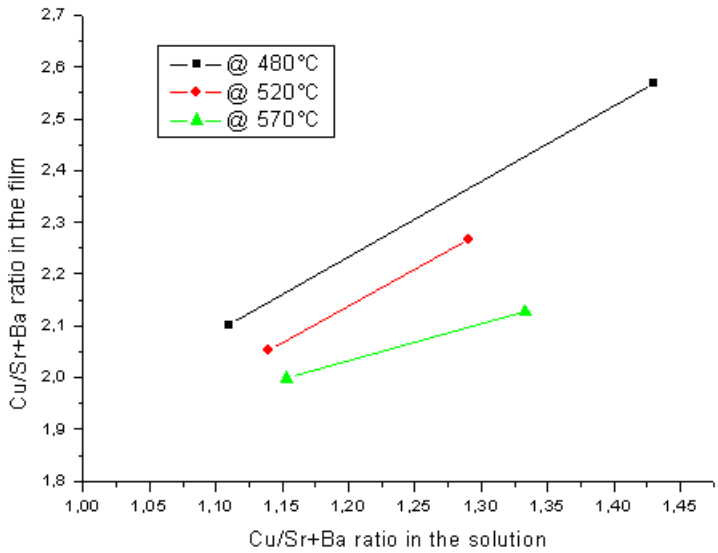

Figure 5.5: Cu/Sr+Ba ratio in the precursor solution versus Cu/Sr+Ba ratio in the as-deposited film, higher deposition temperatures tend to reduce Cu/Sr+Ba ratio in the film

Effect of Ba doping percentage for the same deposition temperature (480 °C) on the Cu/Sr ratio in the film was also studied and the result is given in the figure 5.6.

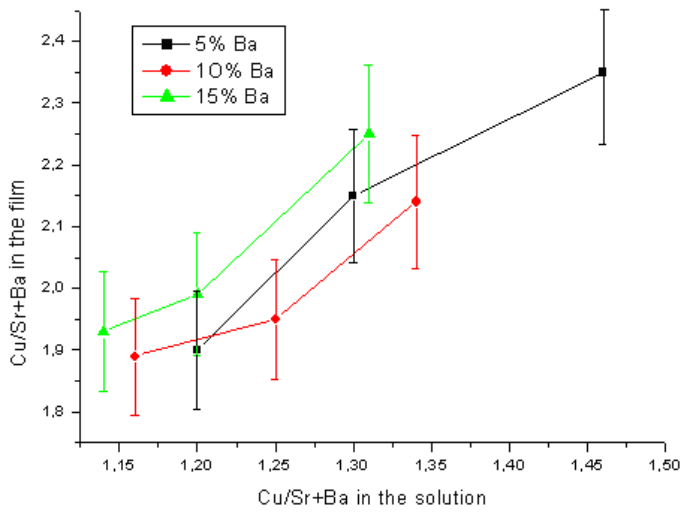

Figure 5.6: Effect of doping percentage on Cu/Sr ratio in the film. Low doping (5-15%) of Ba doping do not change significantly the Cu to Sr ratio in the film.

According to the accuracy of composition measurement there is no significant

effect of low level Ba doping (5-15%) on Cu/Sr ratio in the film.

It has been also noted that the composition of the film also varies slightly with the distance of the substrate from the chimney of the reactor and by changing oxygen partial pressure in the reactor.

5.1.4 Uniformity of Elemental Composition

Elemental composition of the as-deposited film was also analysed at various positions of the film, and a radial variation in composition was found as shown in the figure 5.7.

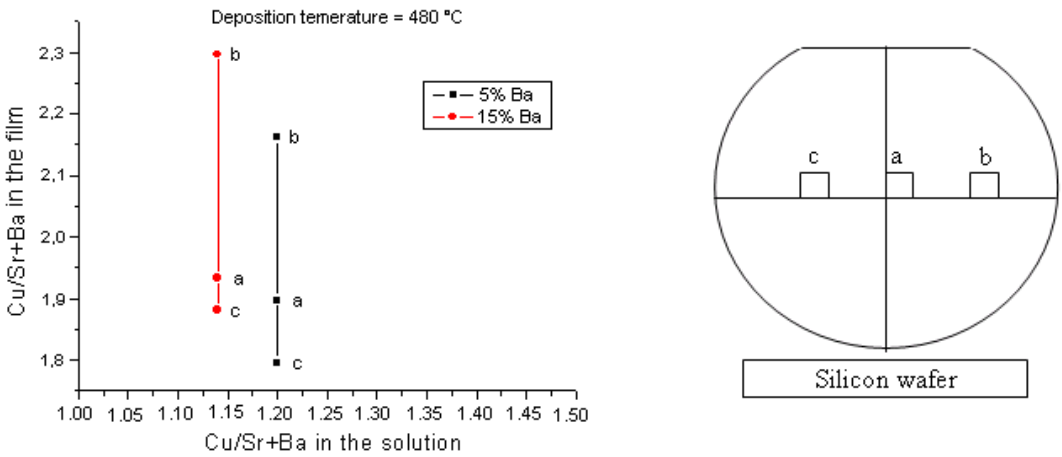

Figure 5.7: Radial variation of elemental composition along the diameter of circular Si substrate

Figure 5.7 shows a spatial variation of elemental composition in radial direction along the diameter of a circular Si wafer. Since the precursor vapor from evaporator to reactor pass though a “U” shaped carrier line, therefor this effect could be related to the difference in atomic weights of the different elements present in precursor vapors. Spatial uniformity of elemental composition could be improved by rotating substrate.

5.1.5 Thickness Uniformity

Thickness uniformity of the film was studied by measuring thickness at various positions using profilometer (Talystep) after photolithography and etching steps processed at FORTH (collaborator of NATCO in Greece) as shown in the figure 5.8. Thickness of the film goes on decreasing as we move away from the center, uniformity in thickness can be observed within 10% for 4 inch diameter.

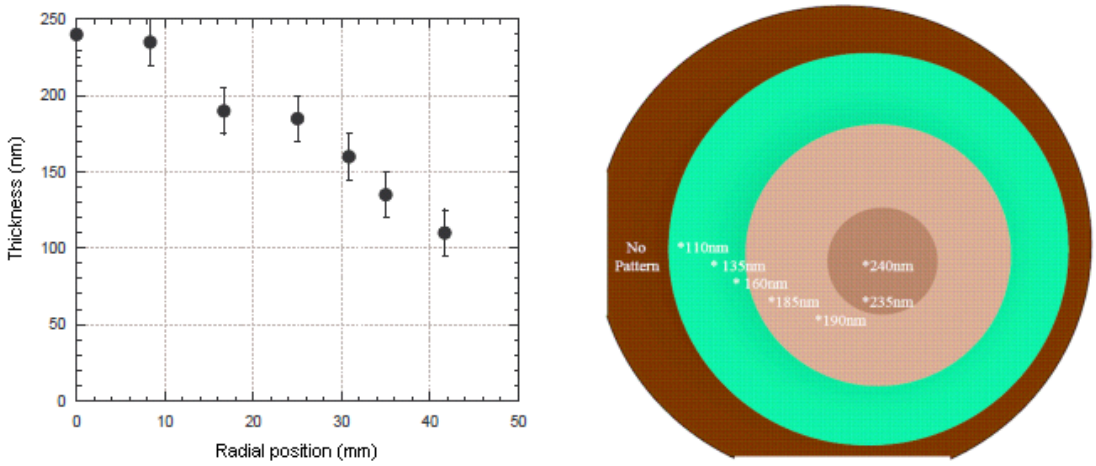

Figure 5.8: Measure of film thickness variation on 4 inch Si wafer. Thickness goes on decreasing as one moves away from the center

5.1.6 Chemical Phases

As-deposited films were analysed by XRD, FTIR, and Raman spectroscopy to identify the chemical phases the films composed of. XRD analysis of the as-deposited films at various deposition temperatures is given in the figure 5.9.

XRD peaks in the figure 5.9 show that whatever the deposition temperature may be (480-540 °C), the as-deposited films do not contain the desired $SrCu_2O_2$ phase. Rather it is composed of $SrCO_3$ and CuO.

To confirm the existence of $SrCO_3$ and CuO detected by XRD is as-deposited

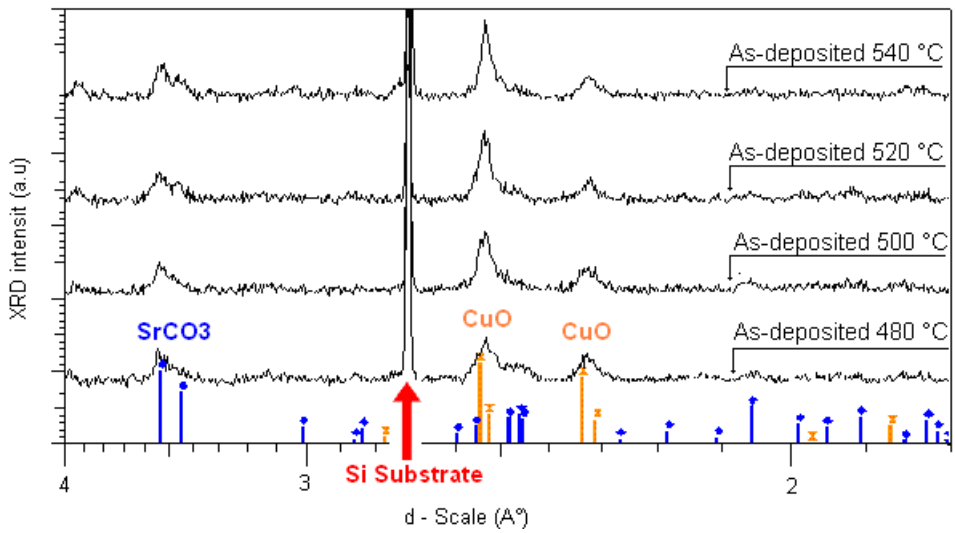

Figure 5.9: XRD pattern of the as-deposited films deposited at various temperatures showing $SrCO_3$ and CuO as main components of the as-deposited films

films and search for amorphous phases undetected by XRD, the as-deposited films were characterized by FTIR and Raman spectroscopy and the corresponding results are given in figures 5.10 and 5.11 respectively.

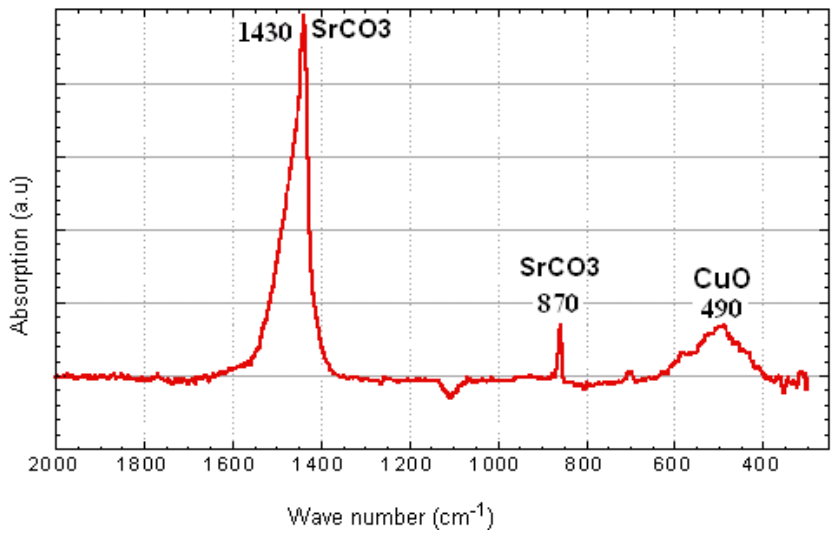

Figure 5.10: FTIR analysis of the as-deposited film showing characteristic peaks of $SrCO_3$ and CuO

FTIR peaks at 1430 cm^{-1} and 870 cm^{-1} are the characteristics peaks for strontium carbonates $SrCO_3$ [170, 171] and peaks in 450-590 cm^{-1} correspond to the peaks of CuO [172–174].

Raman spectroscopy (figure 5.11) also confirms the existence of $SrCO_3$ [175] and CuO [176, 177] in the as-deposited film, while the main peak at 520.9 cm^{-1} corresponds to Si substrate [178]. Si substrate peak at 520 cm^{-1} was also confirmed by analysing a bare Si substrate.

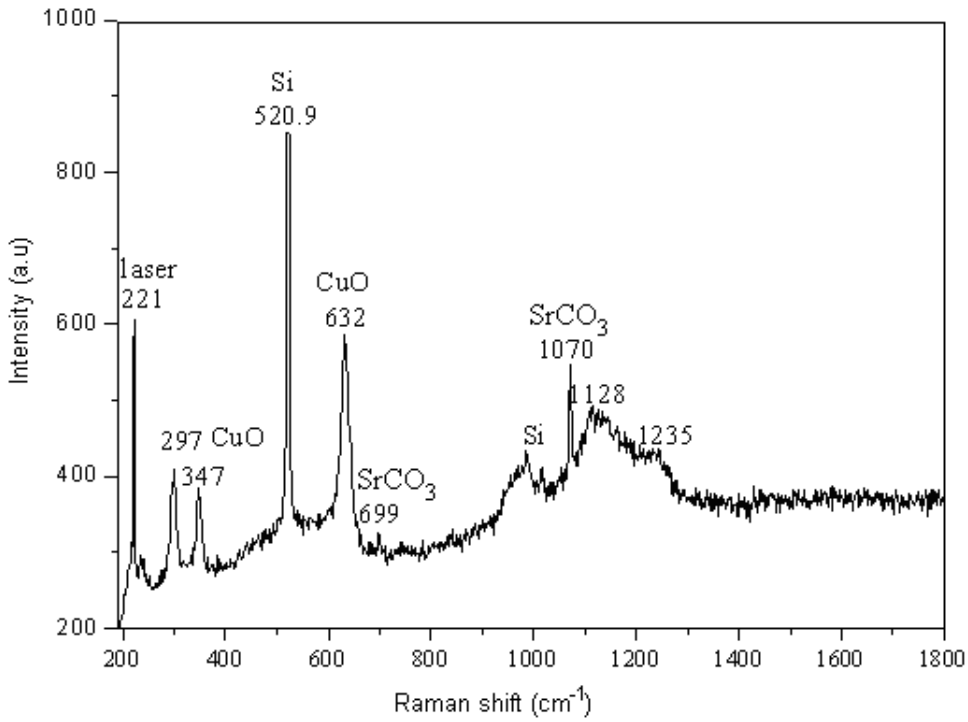

Figure 5.11: Raman peaks of the as-deposited film with 520.9 cm^{-1} as the Si substrate peak and rest of the peaks correspond to CuO $SrCO_3$

From the results in figures 5.9 (XRD), 5.10 (FTIR), and 5.11 (Raman), it is obvious that the as-deposited films do not contain the desired SCO phase. Therefore, some post-deposition treatment is mandatory to decompose carbonates and develop SCO.

5.2 Post-Deposition Treatment

As a first step of post-deposition treatment, Rapid Thermal Process (RTP) annealing under Ar at various temperatures for various durations was applied and the best RTP temperature was found to be 600 °C for the decomposition of $SrCO_3$ in three steps each of 30 seconds as shown in the figure 5.12.

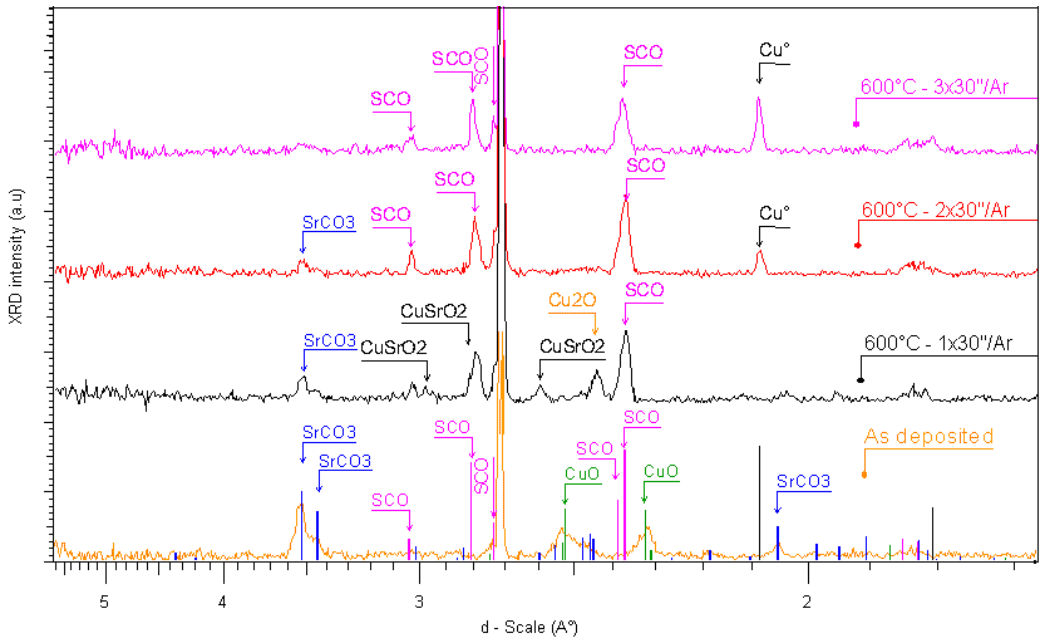

Figure 5.12: XRD analysis of the RTP annealed film under Ar

RTP step at 600 °C for 30 seconds under Ar was not sufficient to decompose $SrCO_3$ completely and yield pure SCO phase, rather two additional phases $SrCuO_2$ and CuO_2 appeared along with SCO. In order to decompose $SrCO_3$ completely, another 30 second RTP step under the same conditions as in the first step was applied. In the second RTP step $SrCO_3$ reduced further, $SrCuO_2$ and CuO_2 disappeared, SCO intensities increased while metallic copper appeared. To eliminate $SrCO_3$ completely, a third RTP step of another 30 seconds was applied. Though this last RTP step was very effective in completely eliminating $SrCO_3$, it increased the quantity of metallic copper.

This means that decomposition of $SrCO_3$ in a reduced oxygen atmosphere leads to the formation of metallic Cu that could be followed by the following reactions.

$$SrCO_3 \rightarrow SrO + CO_2$$
$$SrO + CuO \rightarrow SrCuO_2$$
$$CO_2 + C \rightarrow 2CO$$
$$CO + 2CuO \rightarrow Cu_2O + CO_2$$
$$CO_2 + C \rightarrow 2CO$$
$$CO + Cu_2O \rightarrow 2CO_2 + 2Cu$$
$$CO + SrCuO_2 \rightarrow SrO + Cu + CO_2$$
$$SrO + Cu_2O \rightarrow SrCu_2O_2$$

Carbon contents in the film were induced by the organic nature of precursor. Appearance of metallic copper in Ar annealed films was thought to be due to the reduced oxygen environment. Therefore, in order to avoid the formation of metallic copper the as-deposited film was first annealed by RTP for 30 seconds in O_2 at 600 °C and then in Ar, under the same conditions. The XRD results of the two steps O_2 and Ar annealing are given in the figure 5.13.

In this two steps RTP annealing, O_2 steps is very efficient for decomposing carbonates completely just in 30 seconds. The O_2 RTP annealing step gives rise to a new chemical phase Cu_2SrO_3. This is a high absorbent dark phase [24] as seen by naked eye. In the next Ar RTP step, the Cu_2SrO_3 was completely converted into the desired SCO phase along with Cu_2O and small quantity of metallic copper. This was a promising step towards getting pure SCO thin film. In order to have a pure SCO thin-film, this two steps RTP annealing was repeated again and again for various durations and at various temperatures, but almost the same result was obtained. The appearance of Cu_2O and metallic copper in the film was then thought to be due to high copper concentration in the precursor solution.

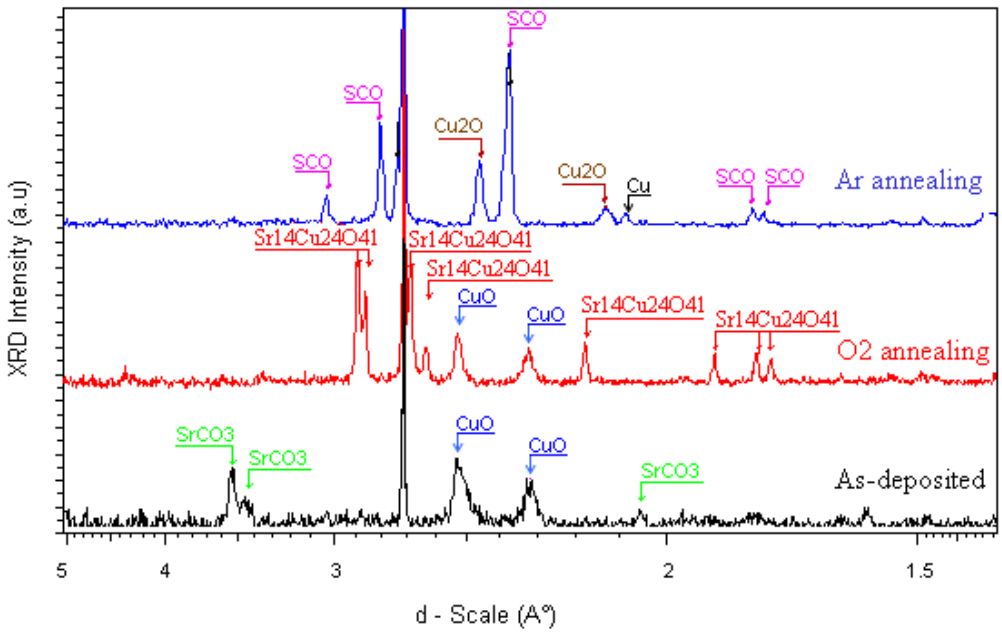

Figure 5.13: XRD analysis of the two steps RTP annealed film under O_2 and Ar. RTP under O_2 completely decompose $SrCO_3$ and gives rise to new phase Cu_2SrO_3. RTP under Ar then leads to SCO phase along with a very small quantity of metallic copper

New films deposited with low copper concentration in the precursor solution were annealed under the same conditions (as those of figure 5.13) and pure SCO phase was obtained, as shown by the XRD results given in figure 5.14.

From XRD data in figure 5.14, it can be concluded that SCO phase cannot be developed below 600 °C.

Metallic copper contents can also be eliminated by low temperature O_2 annealing as shown in the figure 5.15.

It can be also noted from the figure 5.15 that long RTP annealing under Ar leads to large quantity of metallic copper in the film deposited on YSZ substrate. However, O_2 annealing can completely oxidize metallic copper and give rise to $Sr_14Cu_24O_41$ phase. Short RTP annealing under Ar then lead to SCO phase with a small quantity of metallic copper which can be eliminated with conventional annealing under O_2 at low

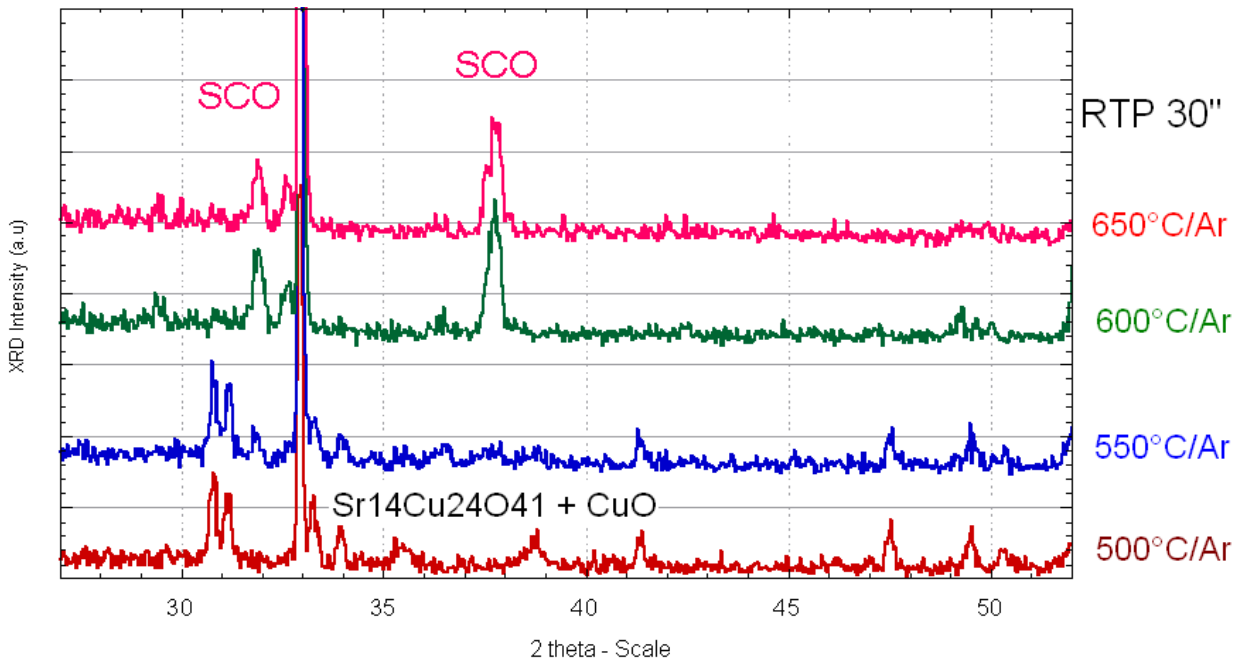

Figure 5.14: XRD analyses of the two steps RTP annealed film under O_2 and Ar with low copper concentration in the precursor solution that results in a pure SCO phase

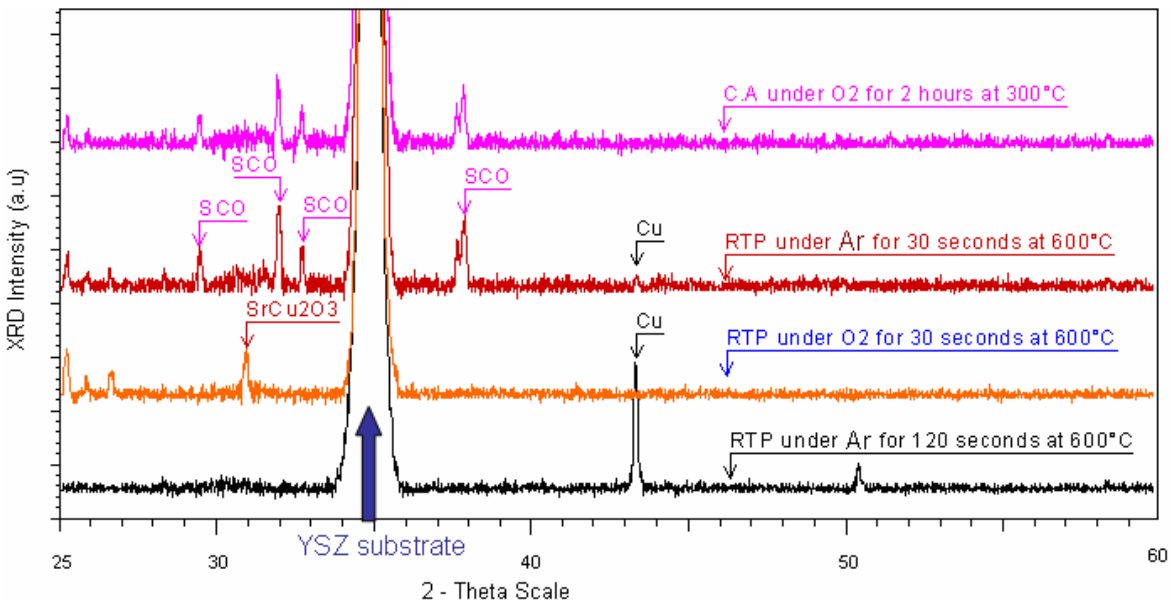

Figure 5.15: Elimination of Cu contents by O_2 annealing at low temperature as 300 °C.

temperature as 300 °C without disturbing SCO phase.

XRD results given in figure 5.14 were verified by FTIR, as shown in figure 5.16.

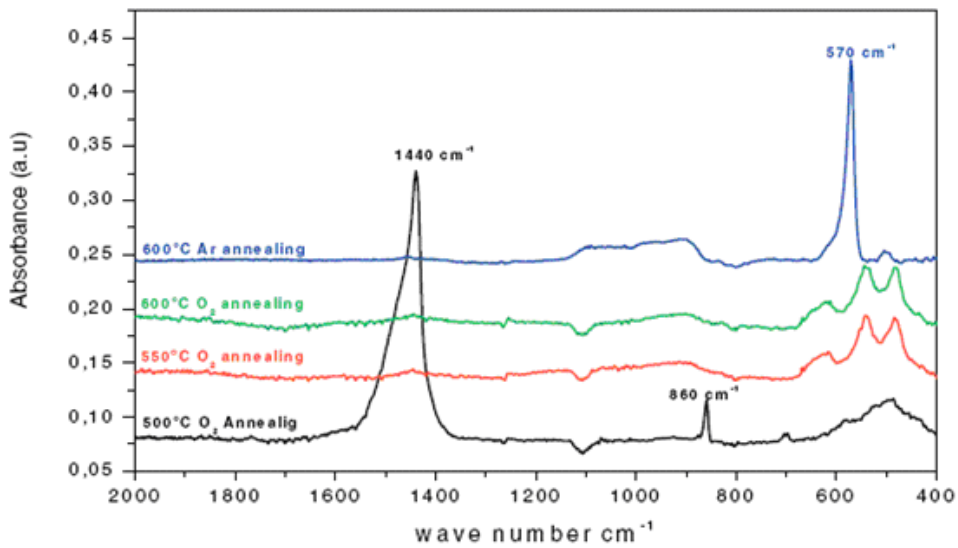

Figure 5.16: FTIR analysis of the two steps RTP annealed film under O_2 and Ar. O_2 annealing above 500 °C decompose carbonates and develops $Sr_14Cu_24O_41$ (peaks at 490 cm^{-1} and 540 cm^{-1} and Ar annealing at 600 °C leads to SCO phase (peak at 570 cm^{-1})

From FTIR analysis in figure 5.16, it is clear that carbonates (1440 cm^{-1} and 860cm^{-1}) can only be decomposed at 550 °C and above, under O_2, and SCO (570 cm^{-1}) [78] can be achieved at 600 °C or above. The two peaks at 490 cm^{-1} and 540 cm^{-1} correspond to $Sr_14Cu_24O_41$ phase [83].

5.3 Phase Transformation Pathway

We have seen in the previous two sections that an as-deposited film is composed of $SrCO_3$ and CuO, while a two step RTP annealing process with O_2 followed by Ar, results in a pure SCO phase. In order to know the pathway of this phase transformation, an in-situ study by Raman spectroscopy was performed.

In-situ study of the annealing process was done by Raman spectrometer provided

with a sample holder capable of heating the sample up to 600 °C in various gaseous environment like, air, O_2, Ar, and N_2, etc. First of all, the as-deposited sample in air at room temperature was analysed and the spectra obtained is given in figure 5.17.

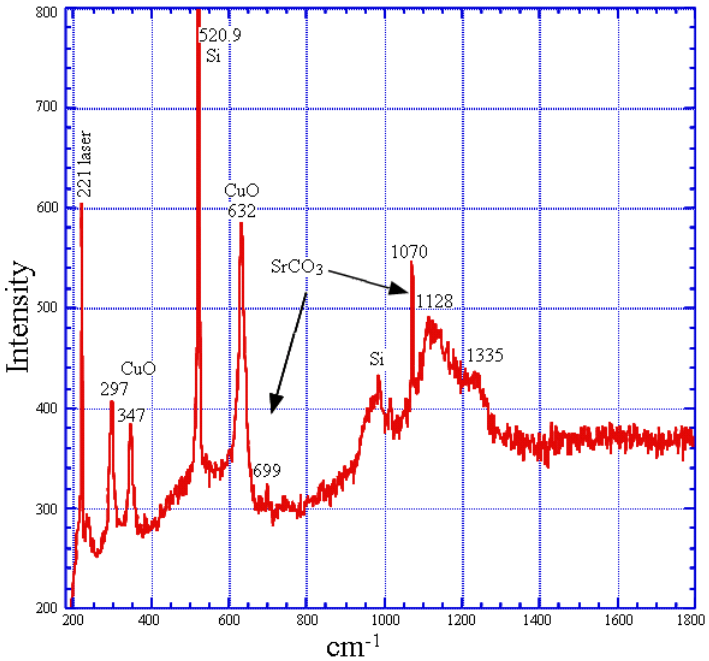

Figure 5.17: In-situ Raman spectra of the as-deposited film on Si substrate at room temperature

The temperature of the sample was then raised from room temperature to 600 °C under O_2 in various steps and the phase transformation was noted by the shift in Raman peaks as shown in the figure 5.18.

The room temperature Raman characteristic peak of $SrCO_3$ at 1070 cm^{-1} continues to decrease and also shifts towards lower frequency value as the temperature increases and completely disappears after 550 °C. The heating rate was set as 20 °C per minutes and each temperature step was given 5 minutes for the possible phase change in the film and to stabilize the temperature. Each step was measured twice to get the average value for 10 minutes. Thus each step got 25 minutes to undergo any possible phase change. At 600 °C two spectra were taken; one exactly in the same way

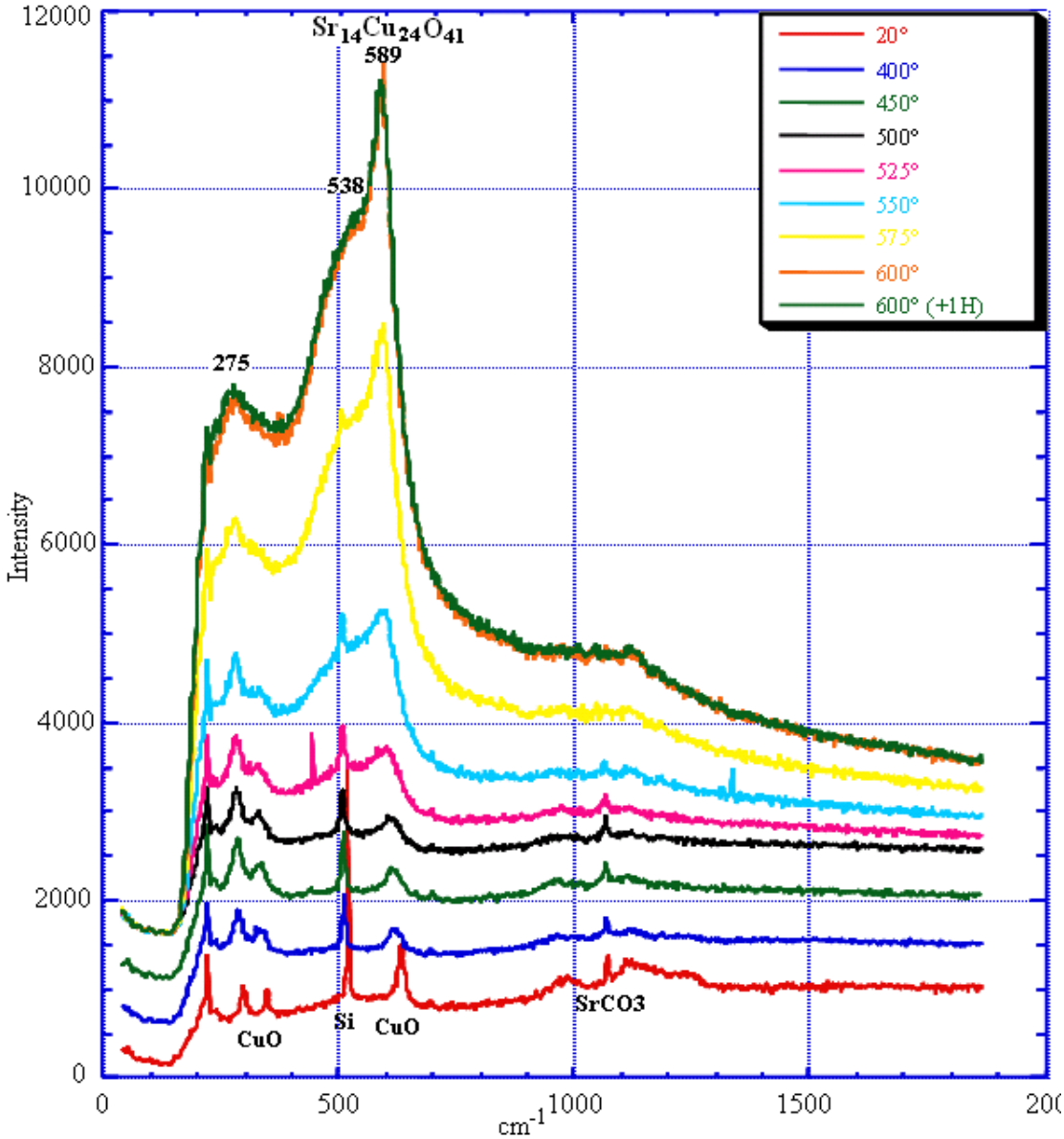

Figure 5.18: Shift in the Raman peaks with the increase in temperature in O_2 atmosphere. The peaks for CuO, Si substrate, and $SrCO_3$ disappear and new phase $Sr_14Cu_24O_41$ appears

like the previous low temperature steps and the second with 1 hour wait time to see any other possible phase change. However, no phase other than $Sr_14Cu_24O_41$ [179] was observed in accordance with ex-situ RTP annealing. This whole phase transformation process (though it was in steps) took almost 4.5 hours.

At the same time almost the same behavior as that of $SrCO_3$ is also shown by the Si characteristic peaks, i.e., Si characteristic peak at room temperature 520 cm^{-1} continuously decreases and shifts to lower frequency value as the temperature goes on increasing, and completely disappears at 600 °C. A magnified image of the shift in Si peaks in the figure 5.18 is shown in the figure 5.19, to demonstrate the diminution of Si intensity peaks with the increase in temperature in O_2 atmosphere more clearly.

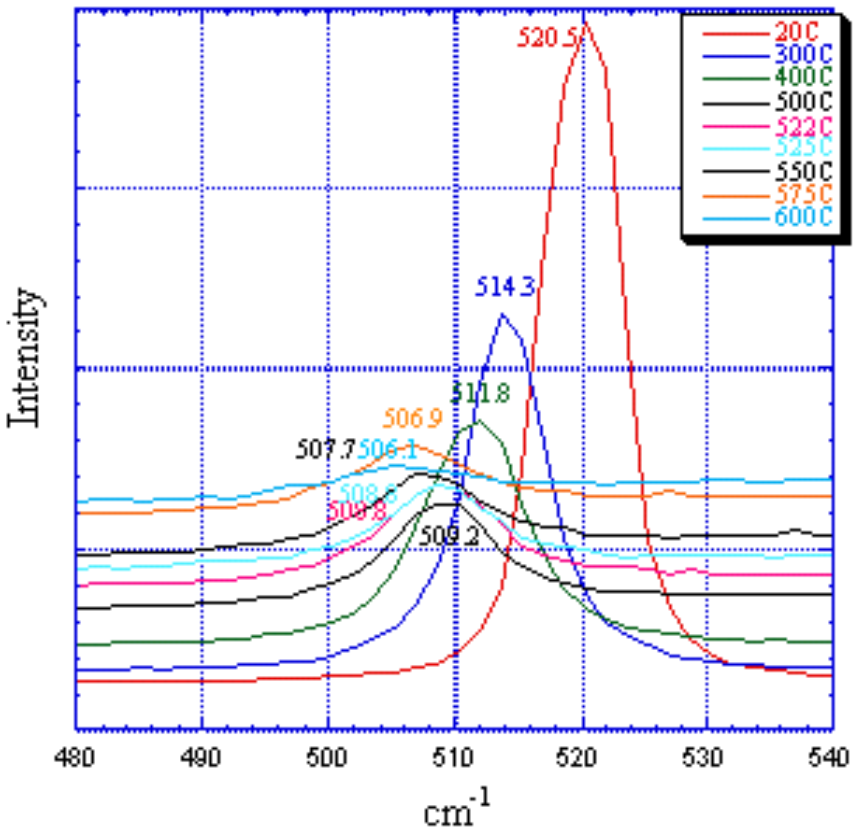

Figure 5.19: Devolution and shifting of Si peaks towards lower frequency value with the increase in annealing temperature under O_2

Disappearance of the Si peak at 600 °C is thought to be due to formation of high absorbent dark phase $Sr_14Cu_24O_41$, under which the Si substrate was invisible for laser

to detect.

In the next step of this in-situ annealing, O_2 gas was replaced by Ar, and Ar gas atmosphere was maintained there for 1 hour to stabilize Ar inside the Raman cell and to allow any possible chemical phase change. After 1 hour in Ar atmosphere at 600 °C, the Raman spectrum was measured twice, each for 10 minutes and a new phase was observed as shown in the figure 5.20.

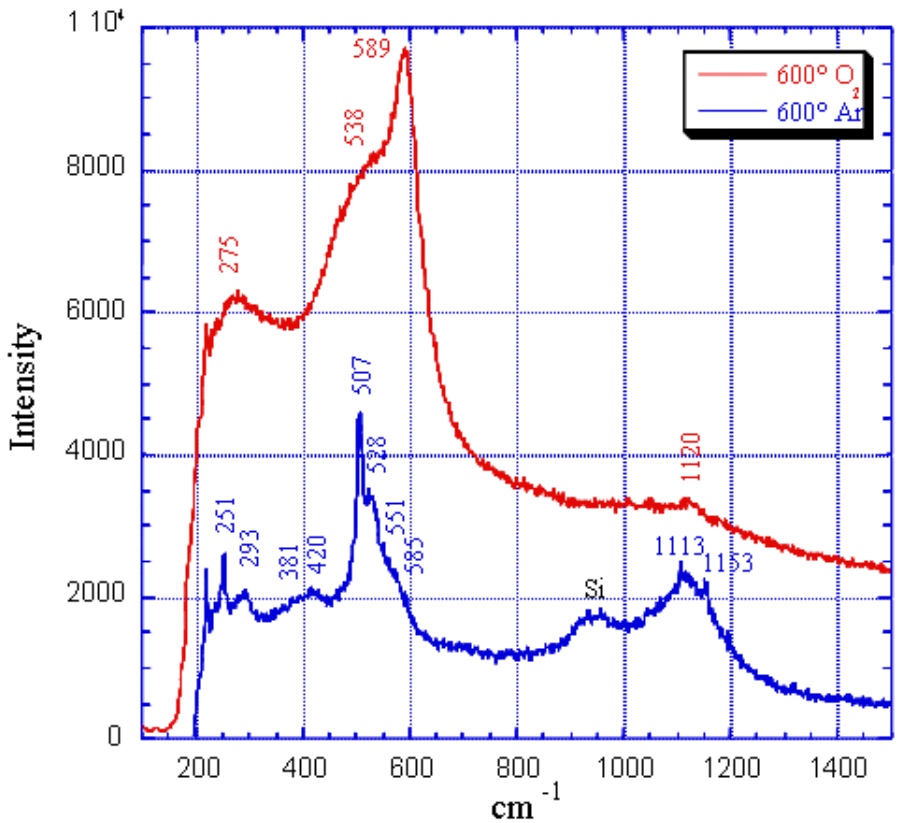

Figure 5.20: New phase formation with replacement of O_2 by Ar

In figure 5.20, the upper red spectrum represents the chemical phase of the film in O_2 atmosphere, and the lower blue shows the new phase formed under Ar. The main peak at 507 cm^{-1} in the blue spectrum was first considered as Si and the newly formed phase was thought to be a transparent one, under which Si was visible to laser

light. However, this transparent phase was later on recognized as SCO, which shows the same Raman spectrum as the blue one in figure 5.20, with the main peak at 520 cm^{-1} at room temperature for the same film on glass substrate (*cf.* figure 5.39).

When the film was allowed to cool down slowly under Ar, the transparent phase having major peak at 507 cm^{-1} at 600 °C reversed into $Sr_14Cu_24O_41$ with major peaks at 533 and 582 cm^{-1} at room temperature [179]. This reversal of phase on slow cooling under Ar is shown in the figure 5.21.

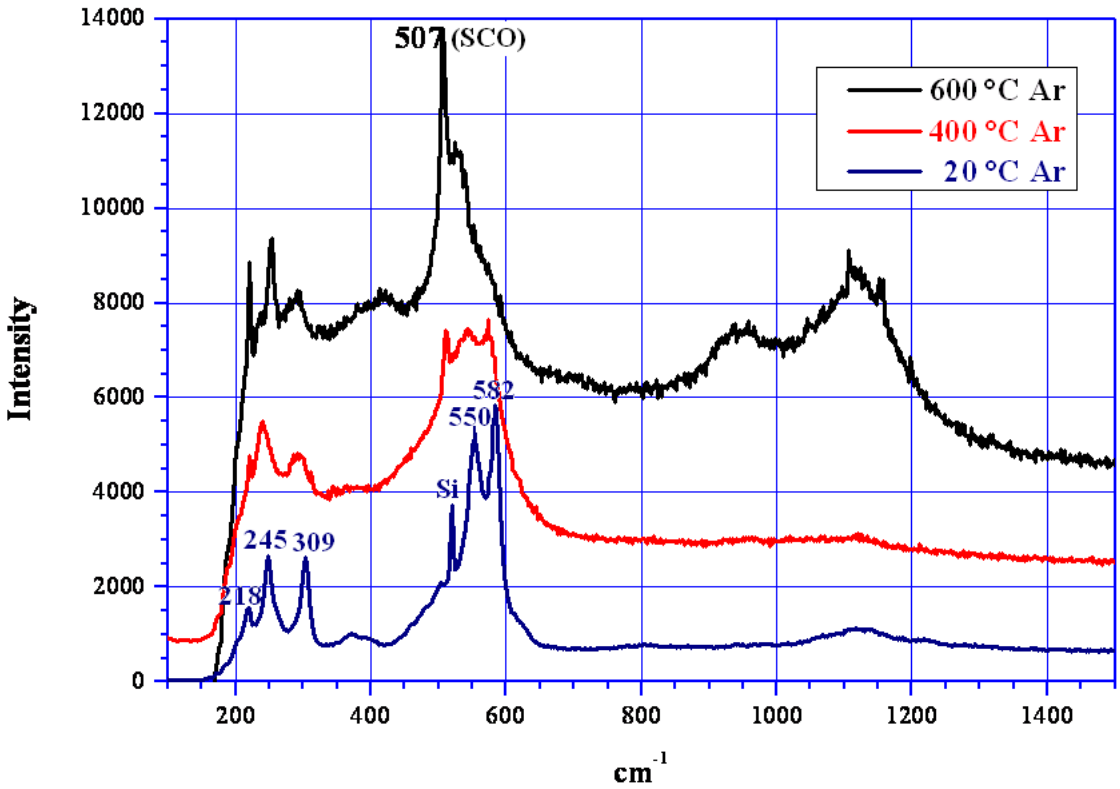

Figure 5.21: Reversal of phase on slow cooling of the film under Ar

From the result of figure 5.21, it can be inferred that in order to retain the transparency of the film (which is due the presence of SCO phase in the film), it is necessary to cool down the film very quickly.

This transformation pathway was also confirmed by recently developed in-situ

XRD study in LMGP as shown in the figure 5.22.

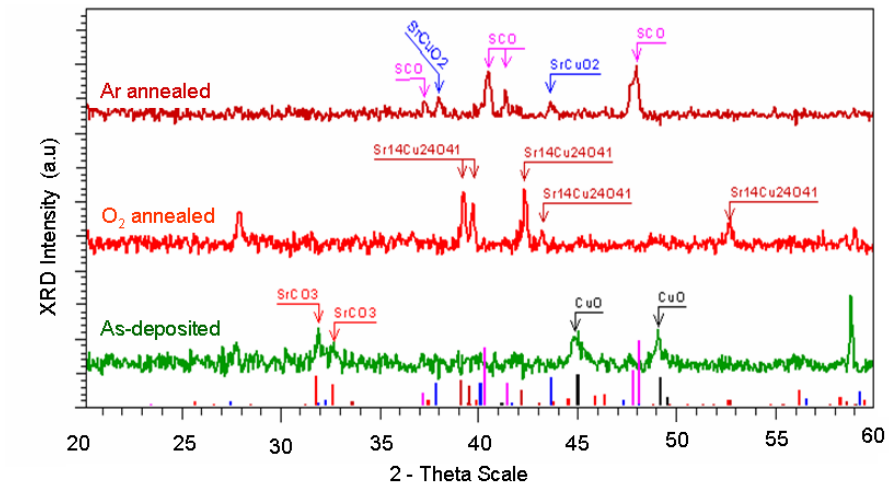

Figure 5.22: In-situ XRD study of transformation pathway of Sr-Cu-O system

As usual, room temperature measurement of the as-deposited film gives $SrCO_3$ and CuO. Film was then heated up to 600 °C under O_2, and $Sr_14Cu_24O_41$ found as the new transformed phase. After obtaining $Sr_14Cu_24O_41$ phase, the film was heated under Ar and then allowed to cool down very quickly by heavy flow of Ar and new phases detected at room temperature after fast cooling was SCO and $SrCuO_2$.

These in-situ XRD results were also verified by another ex-situ XRD measurements for the same sample and the results are given in the figure 5.23.

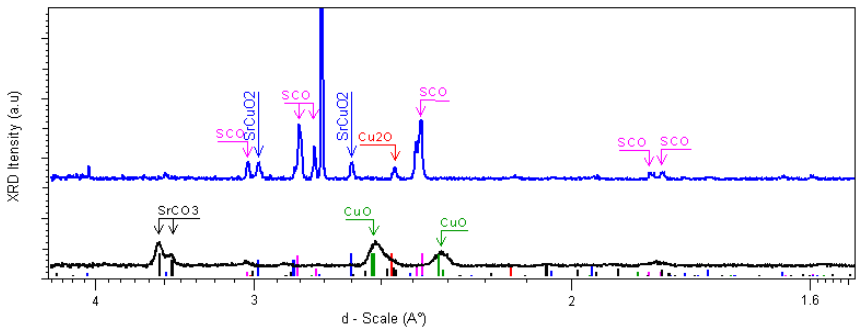

Figure 5.23: Confirmation of In-situ XRD study of transformation pathway in figure 5.22

The in-situ (figure 5.22) and ex-situ (figure 5.23) XRD measurements of the same sample are in good agreement.

5.4 Slow and Fast Cooling of the films in Ar

As we saw in the previous section that slow cooling of the film under Ar in the second step of annealing results in the reversal of SCO into $Sr_14Cu_24O_41$. To verify this fact explicitly, we made a conventional annealing system with the facility of movable furnace to allow slow and fast cooling during Ar annealing step. Raman cell do not allow fast enough cooling rate necessary for the retention of SCO phase once developed in the film at high temperature (around 600 °C). Like wise, there was no such facility in RTP annealing system to allow enough slow cooling rate to verify the in-situ Raman result of natural cooling in the previous section. Therefore, a conventional annealing system of the shape shown in the figure 5.24, was devised to allow natural slow cooling as well forced fast cooling rate.

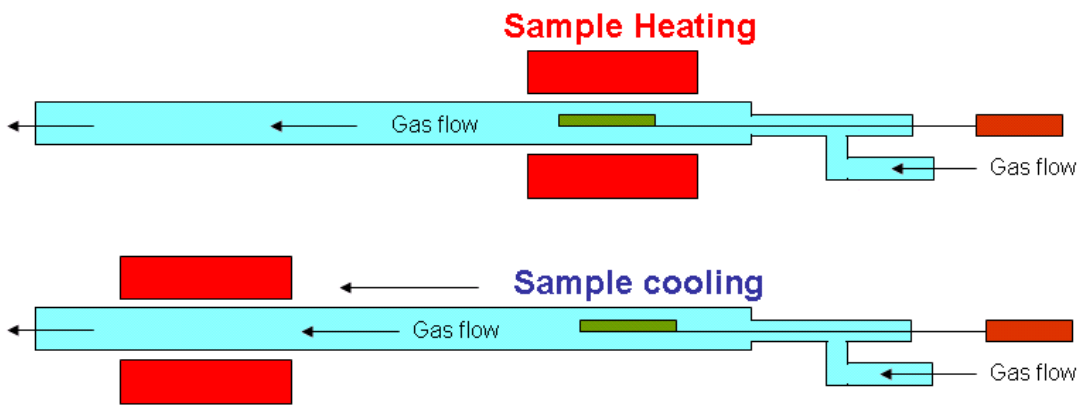

Figure 5.24: Conventional annealing system with fast and slow cooling facility. Moving the furnace away from the sample and allowing high gas flow rate results in fast cooling of the sample

During the heating step of annealing, the furnace is moved towards the sample and the gases (O_2 in the first step, and Ar in the second) are allowed to flow through the sample. In this particular arrangement, shown in the figure 5.24, the sample is

heated up to 630 °C under O_2. From the dark gray visual appearance, one can infer existence of $Sr_14Cu_24O_41$ phase in the film, this takes almost 1.5 hours. At this stage, O_2 gas flow is replaced by Ar and heating of the sample at 630 °C is continued till a bright visual phase appears. This bright visual phase appears in almost 1.5 hours and gives indication of $SrCu_2O_2$ phase. Now at this stage, if one stops the heating and allow cooling of the film under Ar without moving the furnace aside, the bright visual phase disappears when the film reaches room temperature. In contrary to this, if one stops heating and moves the furnace away from the sample, and allow a heavy flow of Ar gas, the sample cooling rate increases too much and one can easily see the bright visual appearance of the film even at room temperature after such fast cooling rate. Difference between slow and fast cooling rate is demonstrated in figure 5.25.

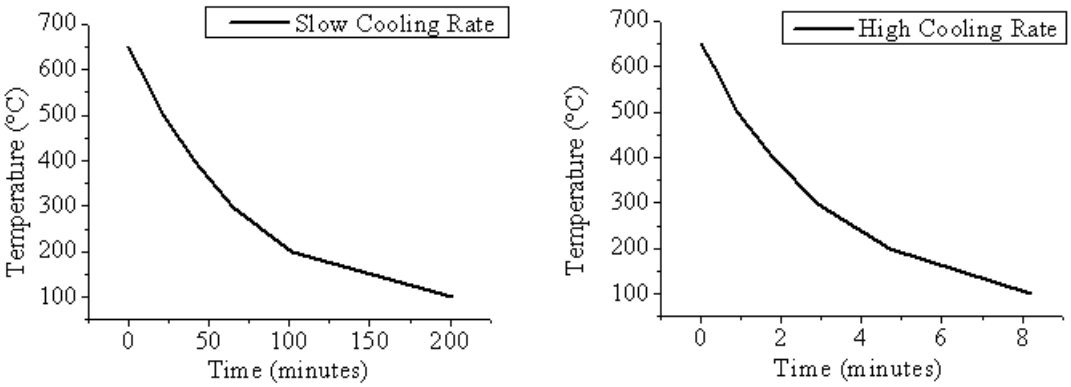

Figure 5.25: Fast and slow cooling rate under Ar. Movable furnace arrangement and heavy flow of gases reduce the cooling duration from 200 to 8 minutes

Time required to reduced temperature from 630 °C to 100 °C during fast cooling is only 8 minutes, while for slow cooling this time prolongs to 200 minutes.

Films annealed under the conditions shown in figures 5.24 and 5.25 were analysed by XRD and the results are given in the figure 5.26.

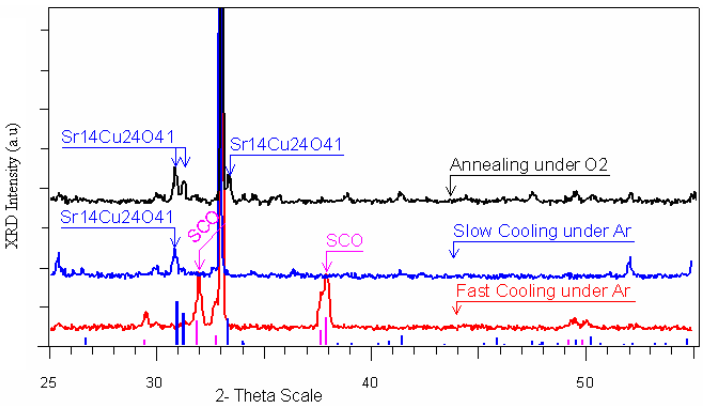

Figure 5.26: Fast cooling under Ar gives rise to SCO, while slow cooling to $Sr_14Cu_24O_41$ phase

From the comparison of XRD peaks given in the figure 5.26, one can see; i) existence of $Sr_14Cu_24O_41$ phase (corresponds to the dark visual phase) in the film due to annealing under O_2, ii) reappearance of $Sr_14Cu_24O_41$ due to slow cooling under Ar, and iii) SCO phase (corresponds to bright visual phase) retained in the film due to fast cooling.

5.5 Effect of Gas Flow rate

In order to note the effect of gas flow rate during annealing, we performed annealing without flow (stationary state), at intermediate flow (2.5 lit/min), and at high flow (5 lit/min) at fixed furnace temperature as 700 °C. The effect of these annealing steps is given in the figure 5.27.

Comparison of the XRD peaks in figure 5.27 shows that no SCO phase can be obtained during annealing when the gas flow is less than 5 lit/min. The two intense peaks at 25.5 and 52.08 on 2θ scale correspond to Cu_3Si phase. The gas flow rate during annealing actually controls temperature in the sample zone. With no gas flow, temperature of the sample as high as that of the furnace, while increase in gas flow rate decreases temperature in the sample zone.

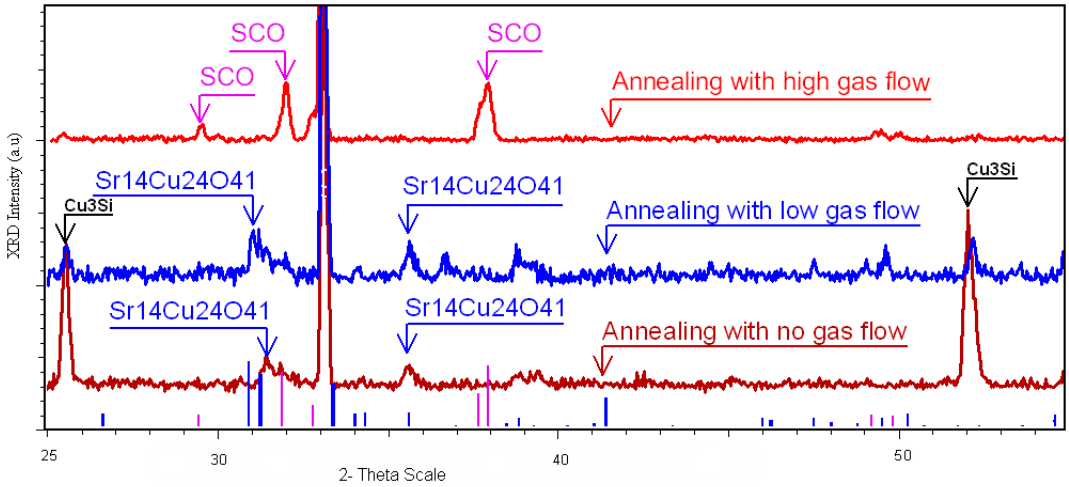

Figure 5.27: Effect of gas flow rate during annealing on the chemical phases. No or low gas flow (< 5 lit/min) cannot develop SCO phase, while heavy gas flow ($\geq$ 5lit/min) is sufficient to develop SCO phase.

The effect of gas flow rate and hence annealing on the morphology of the film was also studied and the comparison is given in figure 5.28.

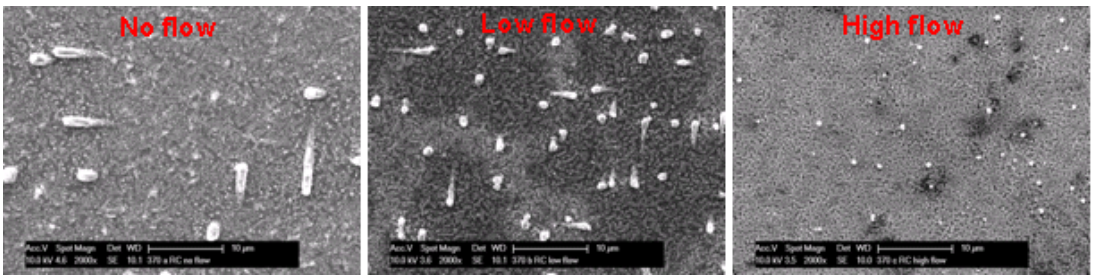

Figure 5.28: Effect of gas flow rate during annealing on the film morphology. The big white spots may correspond Cu_3Si phase formed at high temperature during annealing due to low or no gas flow

Low or no flow of gases during annealing develop copper silicates (big white spots) due to high temperature. However, with high flow there are no silicates and pure SCO phase can be developed as obvious from the XRD data in figure 5.27. This control of temperature in the sample zone by gas flow rate during annealing later proved an important step for fast cooling and heating rate of the film in order to stabilize the SCO phase and minimize cracks.

Due to high temperature, reaction between Cu and Si substrate takes place to form Cu_3Si phase as a result of epitaxial growth at (100) and (200) planes. Formation Cu_3Si can easily be demonstrated from the TEM images given in figure 5.29.

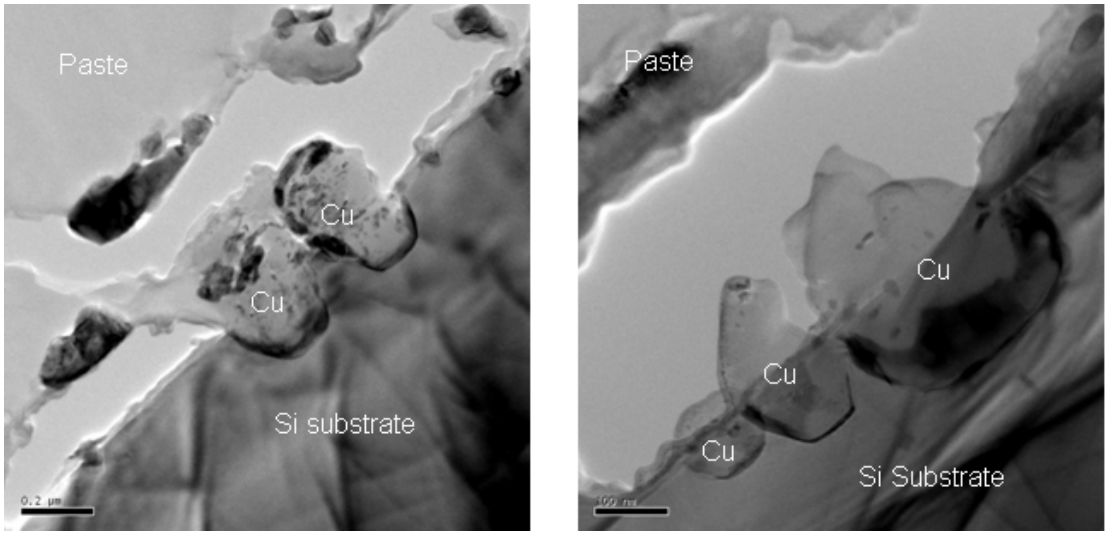

Figure 5.29: Formation of Cu_3Si phase due to diffusion of Cu into Si substrate

Figure 5.29 shows TEM images of cross-sectional view of annealed film under Ar without gas flow which gives rise to high temperature and Cu diffuses into Si substrate forming big grains of Cu_3Si.

5.6 One Step N_2 Annealing

It has been verified by some authors that the type of gas used during annealing also plays significant role [180, 181]. Therefore, conventional annealing with the movable furnace was also performed in N_2 atmosphere at 600 °C. After 2 hours a visual change was observed in color of the film. XRD measurement of this new phase reveals that this change in visual color corresponds to the intermediate phase $SrCuO_2$, already been observed in one step Ar RTP annealing. The same film was then again annealed for 2 hours under the same conditions and a pure SCO phase was observed as shown

in the figure 5.30.

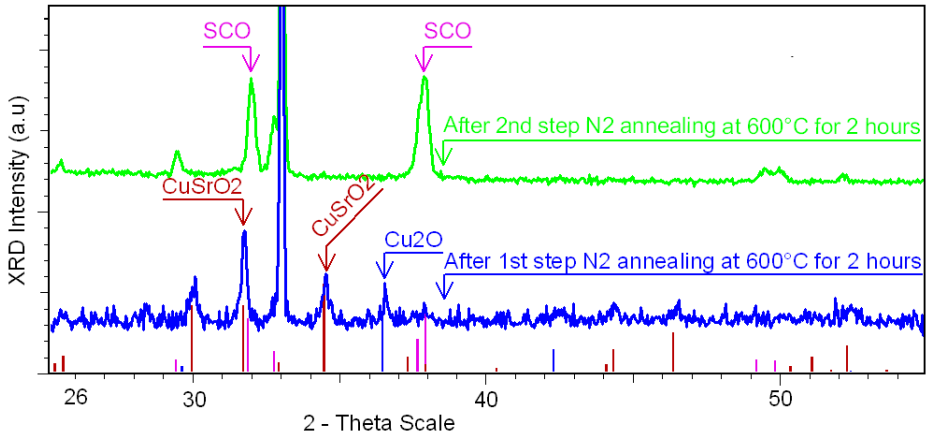

Figure 5.30: Conventional annealing under N_2

This one step conventional annealing under N_2 in comparison to one step Ar RTP annealing is advantageous in a sense that Ar RTP annealing leads to the formation of metallic copper along with SCO, while N_2 annealing leads to pure SCO phase. This may be either due to the change in gas type (from Ar to N_2) or the difference of annealing temperature, as we don't know the exact surface temperature of the film in RTP annealing and the thermocouple measures only the back surface temperature of Si wafer used as stage for the sample. So the measured temperature in RTP annealing may be lower than the real temperature of the film surface.

5.7 Film Deposition on Glass Substrates

SCO phase is believed to be optically transparent and electrically p-type conductive. Therefore, optical transparency and electrical conductivity of the SCO films deposited on Si substrate cannot be measured explicitly because of electrically semiconducting, and optically opaque nature of the Si. Thus, in order to measure the optoelectrical properties of SCO explicitly, one needs to deposit SCO thin film on optically transparent and electrically insulating substrates. For this purpose, we used glass as a

substrate and applied the previously optimized deposition and post-deposition annealing conditions to obtain SCO phase on glass as well. The annealing conditions and XRD data for SCO film obtained on glass substrate is given in the figure 5.31.

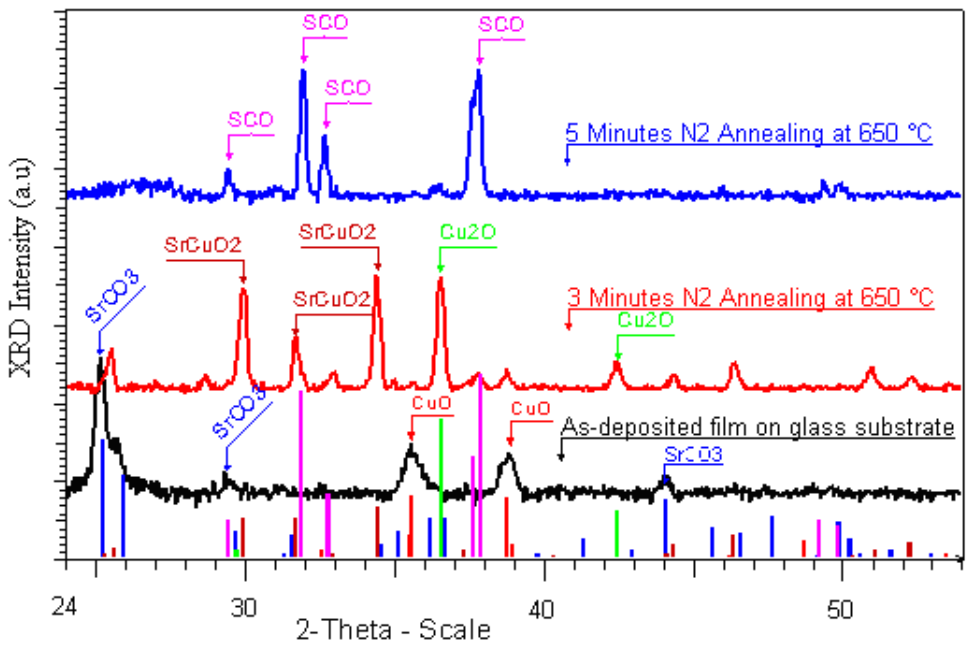

Figure 5.31: XRD analysis of SCO phase on glass substrate. Pure SCO phase in films glass develops after 5 minutes conventional annealing under N_2 with $SrCuO_2$ as an intermediate phase which develops during 3 minutes.

Result given in figure 5.31 is very interesting in a sense that on one hand it gives pure SCO phase on glass substrate and on the other hand the annealing during of 5 minutes is very short as compare to the 4 hours annealing duration for obtaining SCO phase on Si substrate. In RTP annealing we have seen that phase transition takes place in almost one minute. Thus to attain RTP annealing conditions for conventional annealing, a preheated furnace at very high temperature ($\approx$ 850 °C) is moved towards the sample. Due to high temperature gradient between furnace and film, heating of the film takes place at very high rate. Reason of this short annealing time on glass substrate in comparison to long annealing time on Si substrate may be the high annealing

temperature (650 °C) and the fact that heat transfer by convection from the furnace to sample is dominated by radiation. On Si substrate, films annealed at high temperature (> 600 °C) yield epitaxial growth of Cu_3Si, which suppress formation of SCO phase, while there is no such problem of Cu_3Si on glass substrate even at 650 °C annealing temperature. Annealing temperature above 650 °C on glass substrate was not tried as it exceeds the glass transition point T_g of the substrate. This fact of short annealing was also confirmed by obtaining SCO phase on YSZ substrate for 5 minutes annealing at temperature $\geq$ 650 °C.

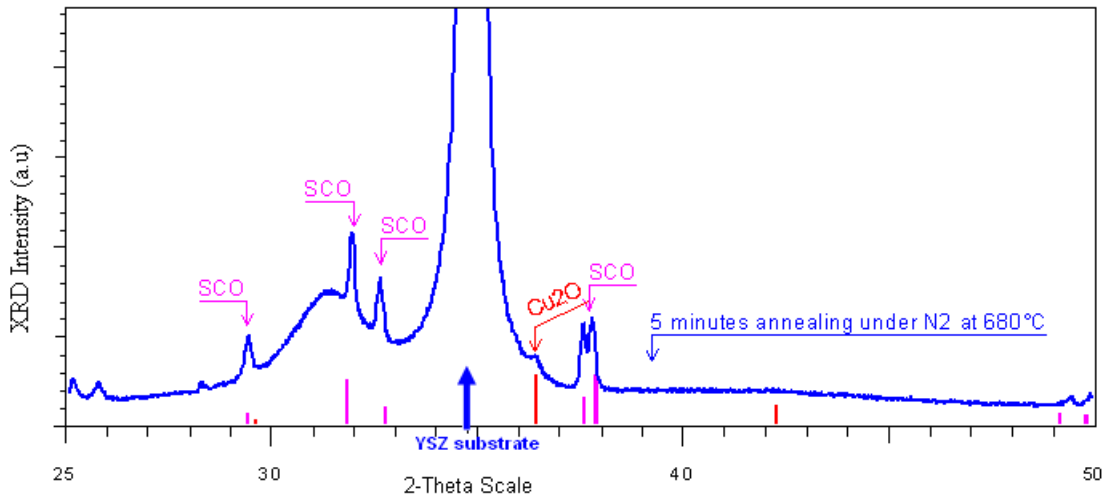

Figure 5.32: 5 minutes annealing in N_2 at 680 °C give rise to SCO phase.

From XRD results given in figures 5.31 and 5.32, one can conclude that short annealing duration could be related to high temperature and mode of heat transfer from furnace to the sample.

One surprising outcome of this annealing in case of long duration ($\geq$ 4 hours) is the complete removal of Sr from the film and the appearance of pure Cu_2O phase as shown in figure 5.33.

This removal of Sr from the films in case of long annealing duration under N_2

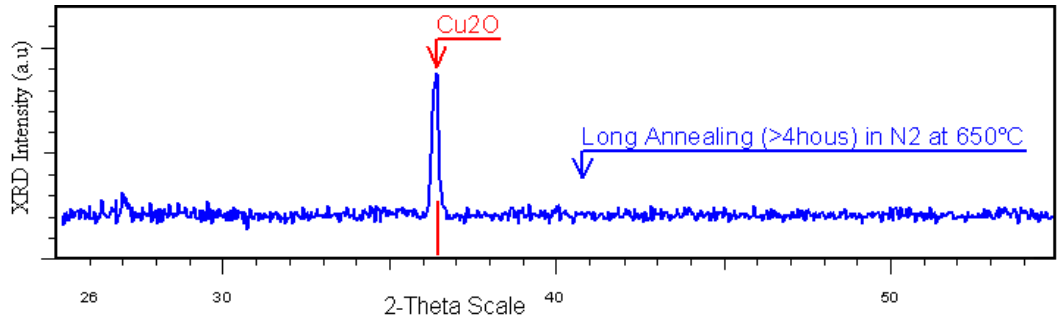

Figure 5.33: Effect of long annealing (≥4 hours) in N_2 at 650 °C. Sr contents in film defuse into the substrate and the film is composed of only Cu_2O

could be due to the diffusion of Sr atoms into glass substrate. To verify this fact, Cu_2O film obtained after prolonged annealing was studied by TEM in the cross sectional orientation and EDX analysis of the substrates determined diffusion of Sr into the substrate as shown in the figure 5.34.

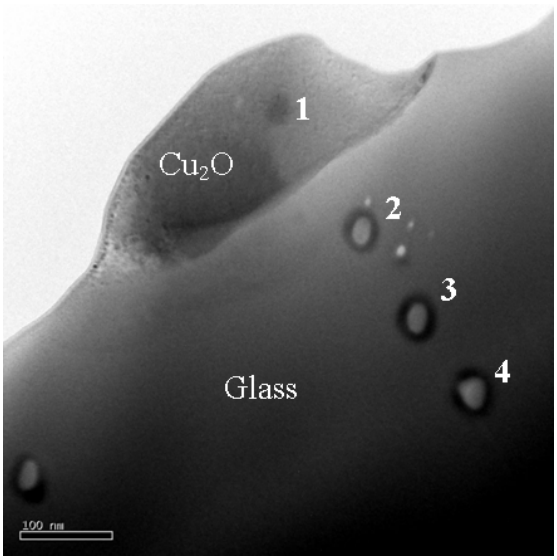

Figure 5.34: Cross-sectional view of the prolonged annealed film on glass substrate by TEM. EDX analysis were performed at Points 1,2,3 and 4.

EDX analysis of the points 1,2,3 and 4 in figure 5.34 is given in figure 5.35.

From the EDX analysis of the grain at point 1 (figure 5.34), it is clear that there

EDX 1

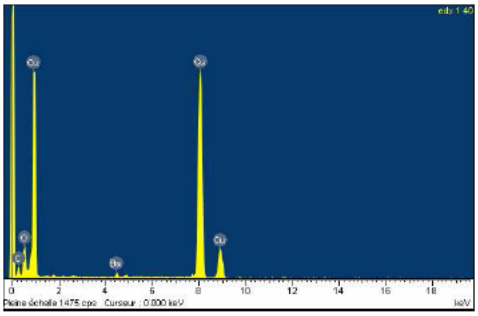

Element	%Mass	%Atomic
C K	3.65	14.19
O K	7.55	22.01
Cu K	85.35	62.64
Ba L	3.44	1.17
Total	100.00	

EDX 2

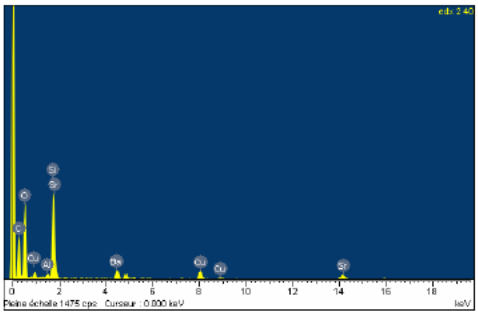

Element	%Mass	%Atomic
C K	25.07	41.37
O K	31.02	38.44
Al K	0.78	0.57
Si K	21.49	15.17
Cu K	4.85	1.51
Sr K	6.18	1.40
Ba L	10.61	1.53
Total	100.00	

EDX 3

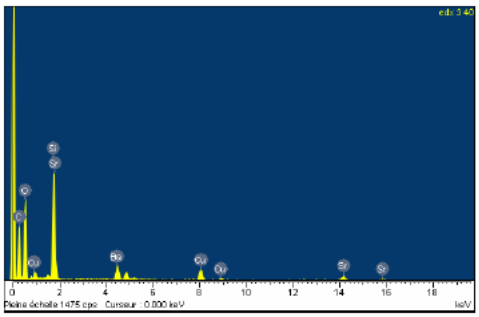

Element	%Mass	%Atomic
C K	25.42	42.86
O K	28.45	36.01
Si K	22.80	16.44
Cu K	5.17	1.65
Sr K	4.37	1.01
Ba L	13.79	2.03
Total	100.00	

EDX 4

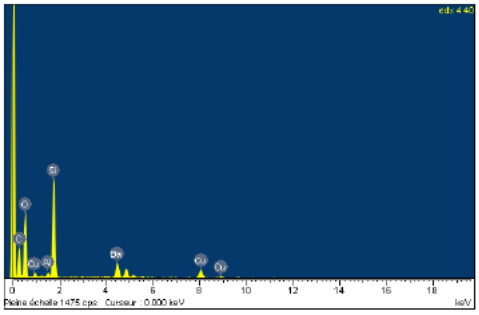

Element	%Mass	%Atomic
C K	18.80	33.88
O K	29.57	40.00
Al K	0.83	0.67
Si K	27.01	20.82
Cu K	4.83	1.65
Ba L	18.95	2.99
Total	100.00	

Figure 5.35: EDX analysis of the points 1,2,3 and 4 shown in figure 5.34.

is no Sr inside the grain. So, as detected by XRD in figure 5.33, the grain is composed of Cu_2O. EDX analysis detect Sr for points 2 and 3 inside the substrate. Quantity of Sr at point 2 is more than at point 3, while there is no Sr at point 4. This means that Sr diffusion into the substrate go on decreasing as we go deep into the substrate.

SCO film obtained on glass substrate after short annealing (5 minutes) was also studied by TEM, and EDX analysis of the grain and substrate was performed to know about the Sr content in the grain and in the substrate. Figure 5.36 shows the cross-sectional view of SCO film on glass substrate by TEM.

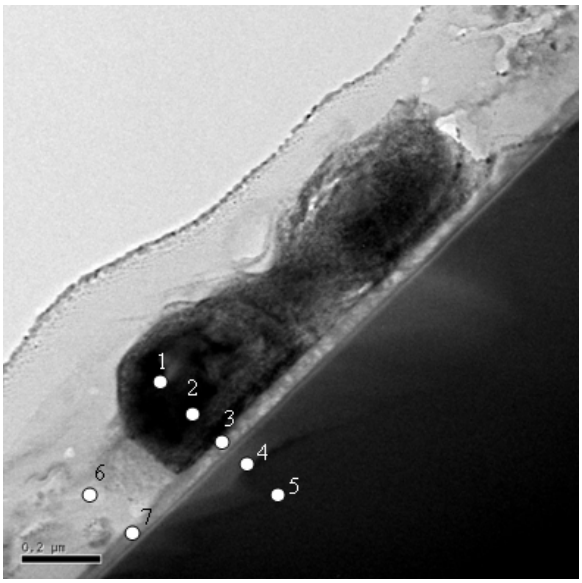

Figure 5.36: Cross-sectional view of the SCO film on glass substrate obtained after short annealing (5 minutes) by TEM. EDX analysis were performed at Points 1,2,3...7.

In figure 5.36, points 1 and 2 correspond to film grain, point 3 to interface between the grain and the substrate, points 4 and 5 to the substrate, point 6 to the amorphous phase region between the grains, point 7 to the interface between the substrate and amorphous phase of the film.

EDX analysis of the points 1,2,3,4 and 5 in figure 5.36 is given in figure 5.37.

EDX 1

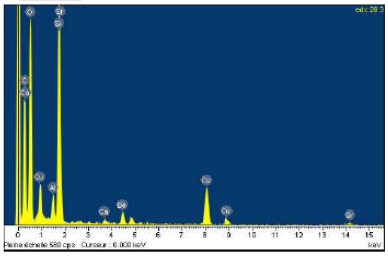

Element	%Mass	%Atomicque
C K	21.67	54.34
O K	8.99	16.93
Cu K	42.10	19.96
Sr K	22.39	7.70
Ba L	4.86	1.07
Total	100.00	

EDX 2

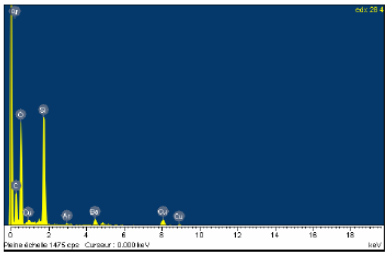

Element	%Mass	%Atomicque
C K	17.08	43.23
O K	13.14	24.97
Ca K	0.38	0.29
Cu K	58.53	28.00
Sr K	8.74	3.03
Ba L	2.12	0.47
Total	100.00	

EDX 3

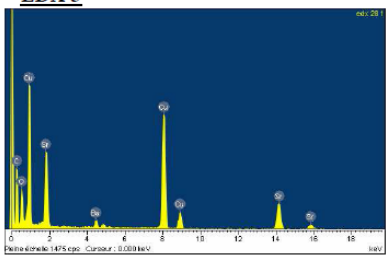

Element	%Mass	%Atomicque
C K	27.46	42.04
O K	34.04	39.12
Al K	2.20	1.50
Si K	20.96	13.72
Ca K	0.47	0.22
Cu K	8.46	2.45
Sr K	1.27	0.27
Ba L	5.13	0.69
Total	100.00	

EDX 4

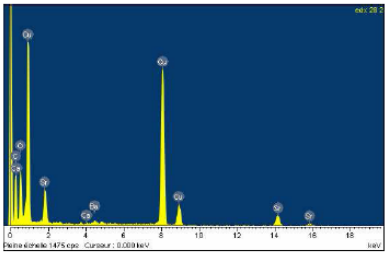

Element	%Mass	%Atomicque
C K	17.29	27.22
O K	43.62	51.55
Si K	28.20	18.98
Ar K	0.41	0.19
Cu K	3.79	1.13
Ba L	6.70	0.92
Total	100.00	

EDX 5

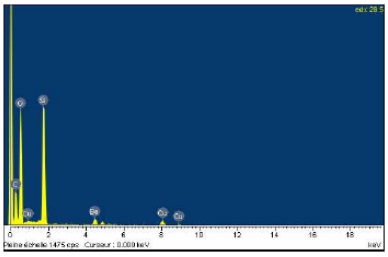

Element	%Mass	%Atomicque
C K	16.42	25.83
O K	44.39	52.42
Si K	29.84	20.07
Cu K	2.47	0.73
Ba L	6.89	0.95
Total	100.00	

Figure 5.37: EDX analysis of the points 1,2,3,4 and 5 shown in figure 5.36.

From the EDX analysis of points 1 and 2, it is clear that the grain contains Cu as well as Sr which could give rise to SCO as detected by XRD peaks in figure 5.29. For the interface point 3, a small quantity of Sr is detected, where there is no Sr at points 4 and 5 of the substrate. Thus, from the EDS analysis of the glass substrate by TEM in figure 5.34 and 5.36, it can be concluded that prolonged annealing results in the diffusion of Sr into the substrate.

EDX analysis of points 6 and 7 of figure 5.36 is given in figure 5.38.

EDX 6

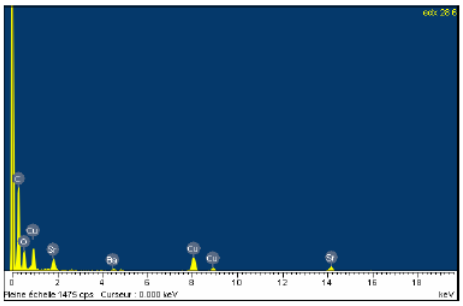

Element	%Mass	%Atomic
C K	62.41	81.05
O K	14.56	14.19
Cu K	12.39	3.04
Sr K	7.96	1.42
Ba L	2.68	0.30
Total	100.00	

EDX 7

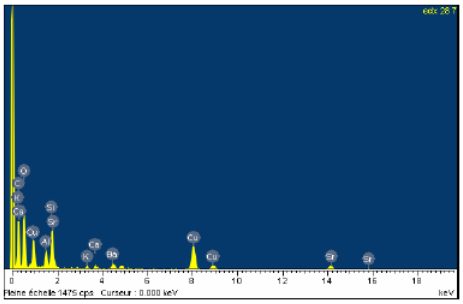

Element	%Mass	%Atomic
C K	34.77	54.66
O K	25.05	29.56
Al K	3.83	2.68
Si K	9.26	6.23
K K	0.60	0.29
Ca K	0.74	0.35
Cu K	14.63	4.35
Sr K	4.64	1.00
Ba L	6.47	0.89
Total	100.00	

Figure 5.38: EDX analysis of the points 6 and 7 shown in figure 5.36.

EDX elemental analysis of points 1 and 2 (figure 5.37), and 6 (figure 5.38) shows that Cu and Sr quantities at the grain positions are much higher than the region between the grains.

The XRD result given in figure 5.31 was also confirmed by Raman spectroscopy as given in figure 5.39.

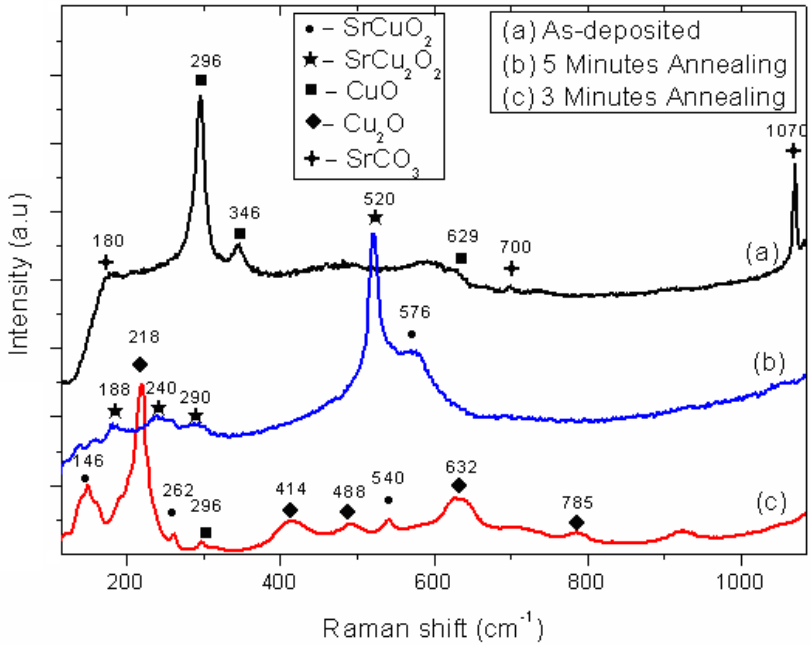

Figure 5.39: Ex-situ Raman study of 3 and 5 minutes annealing effect at 650 °C. Annealing under N_2 for 3 minutes leads to $SrCuO_2$ and Cu_2O, and SCO phase appears after 5 minutes.

As always expected the as-deposited film is composed of $SrCO_3$ [175] and CuO [176, 177]. After 3 minutes annealing at 650 °C $SrCO_3$ decomposes and new phases $SrCuO_2$ [182–184] and Cu_2O [185, 186] appear. However, annealing under N_2 for 5 minutes gives pure SCO with main peak at 520 cm^{-1} [78]. Ex-Situ Raman spectrum in figure 5.39 for SCO on glass substrate is analogous to that in the in-situ Raman spectrum (figure 5.20) obtained with replacement of O_2 gas by Ar. Hence it can be concluded from the results of figures 5.20 and 5.39 that the main peak at 507 cm^{-1} at 600 °C under Ar (in figure 5.20) actually corresponds to the SCO phase at 520 cm^{-1} at room temperature (in figure 5.39).

5.8 Optical Transparency Measurement

Next important step was to measure optical transparency of the SCO thin film. Though we had a chemically pure SCO phase on glass substrate, it was showing lower

transparency compared to as-deposited film. This fact was obvious from visual observation as well as from spectrometric measurement given in the figure 5.40.

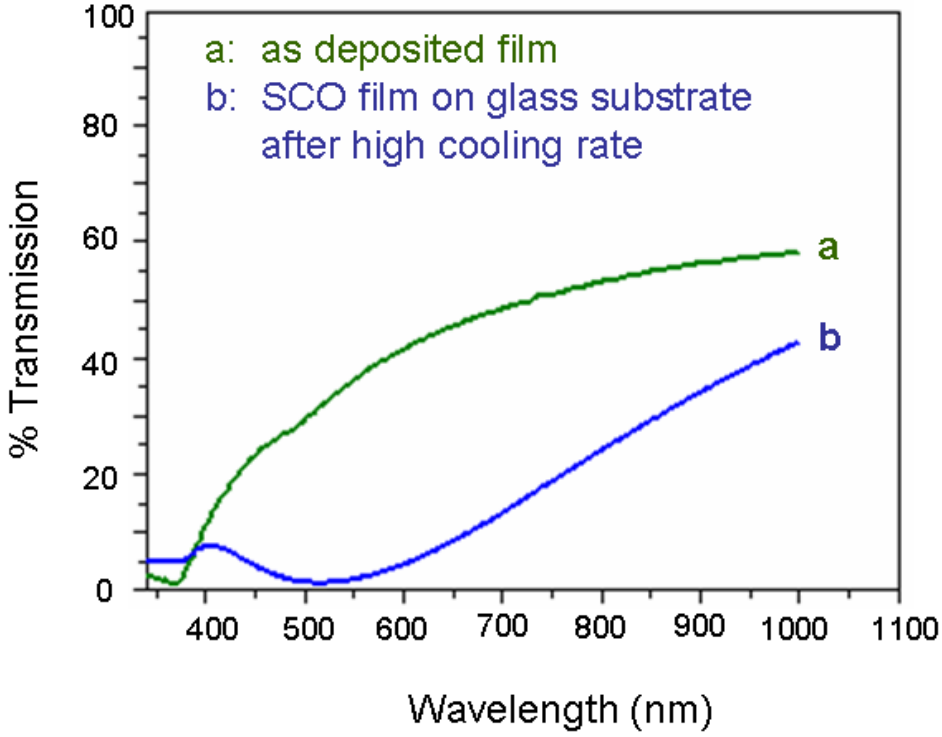

Figure 5.40: Transparency measurement of as-deposited and SCO thin film on glass substrate. As-deposited film shows higher transparency than SCO

Reason of this low transparency (high diffusion) of the SCO film in comparison to the as-deposited film was thought to be due the morphological defects arising during annealing. Surface roughening of the film upon annealing is governed by the well-known Ostwald ripening. This is a coalescence process involving growth of larger crystallites at the expense of smaller crystallites. Through atoms migration small crystallites migrate to larger crystallites resulting in large volume of voids [130]. Comparison of SEM images of the film before and after conventional annealing is given in figure 5.41.

In the conventionally annealed film (figure 5.41) one can see wide cracks devel-

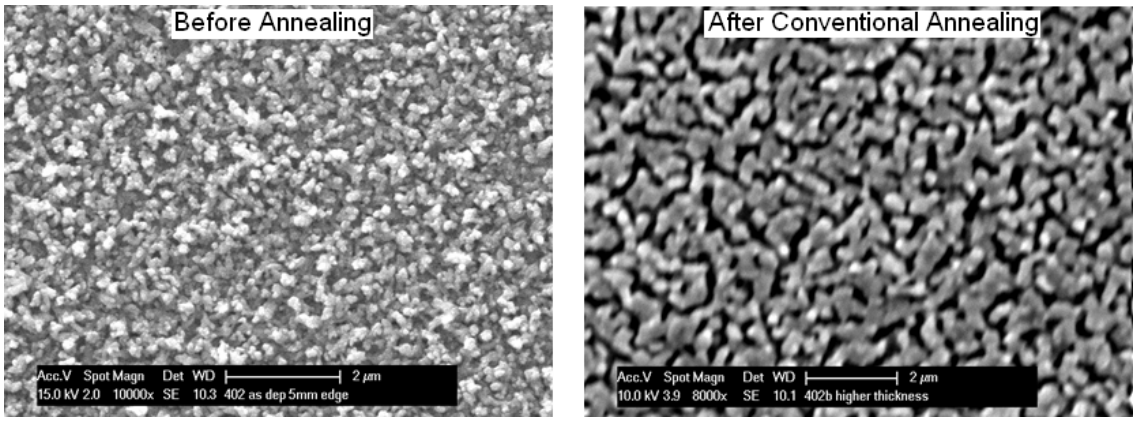

Figure 5.41: Morphology comparison of the film before and after conventional annealing. Wides cracks in the film appear after conventional annealing

oped in the film during annealing. Cracks in the films arise due to internal stresses in the film [187, 188]. Many factors, such as; mismatch between the thermal expansion coefficients of the film and the substrate, lattice misfit with the substrate, variation of the interatomic spacing with crystal size, crystallization processes, microscopic voids, and phase transformation, etc., are thought to play role in creating stresses in the films [138, 187, 189]. Cracks are disadvantageous towards efficiency (optical, electrical, magnetic etc.) of the films [138, 190]. Rate of heating and cooling can play an important role in depressing the crack generation during annealing [139, 190]. Cracks formation in the film can also be attributed to the elastic mismatch between the film and the substrate, and to the thickness ratio between the substrate and the film [191]. Some studies also reveals the effect of annealing gas on the cracks magnitudes [187, 190].

To avoid the formation of cracks in the film during annealing, we adopted three approaches; 1) increasing the heating rate during annealing, 2) depositing thicker films, and 3) using YSZ as a substrate due to its small lattice mismatch with SCO to obtain epitaxial film. However, it was found after some experiments that not only the heating and cooling rate, but duration of annealing has also a prominent effect on crack magnitude. The idea of increased heating rate is obvious from the morphological comparison

of the RTP and slowly heated conventionally annealed film as shown in the figure 5.42.

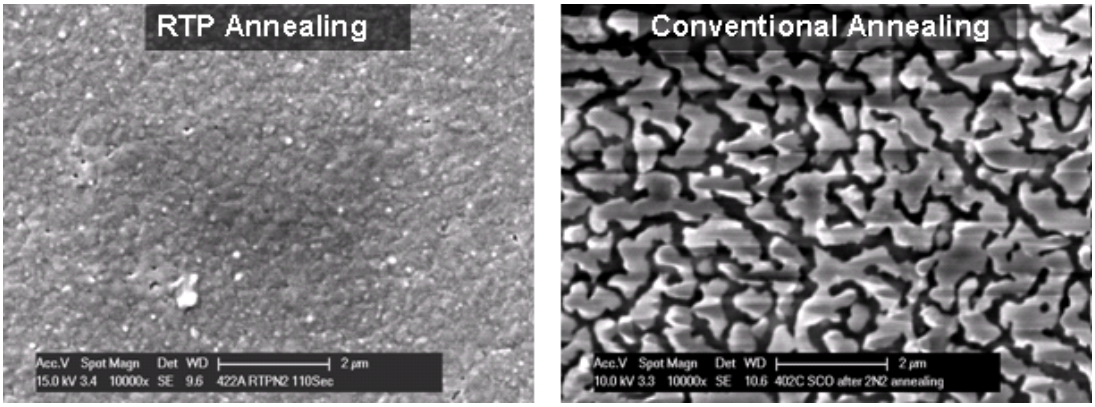

Figure 5.42: Morphological comparison of the RTP and slow heated conventionally annealed films. RTP annealed film has no cracks due to high heating and cooling rate, and short annealing duration

RTP annealed film shows no cracks in comparison to the slowly heated conventionally annealed film. Thus in order to achieve almost the same RTP annealing conditions for conventional annealing, the preheated furnace at very high temperature is moved towards the film as shown in the figure 5.43.

When a preheated furnace at high temperature is moved towards the sample, heating of the film takes place at very high rate due to high temperature gradient between furnace and the film. Temperature at the sample zone is controlled by heavy flow of gas to keep temperature below the substrate transition temperature (T_g). For example, in case of films deposited on glass substrates, a preheated furnace at 850 °C is moved towards the sample and temperature of the sample is maintained at 650 °C, a temperature just below the glass transition temperature T_g = 660 °C of the substrate. A high thickness film was also annealed in the same way to see the effect of film thickness in avoiding the cracks. SEM images of low and high thickness films conventionally annealed with high heating and cooling rate is given in the figure 5.44.

From SEM images of the films shown in figure 5.44, it is evident that high heating rate during conventional annealing is very efficient in avoiding cracks formation.

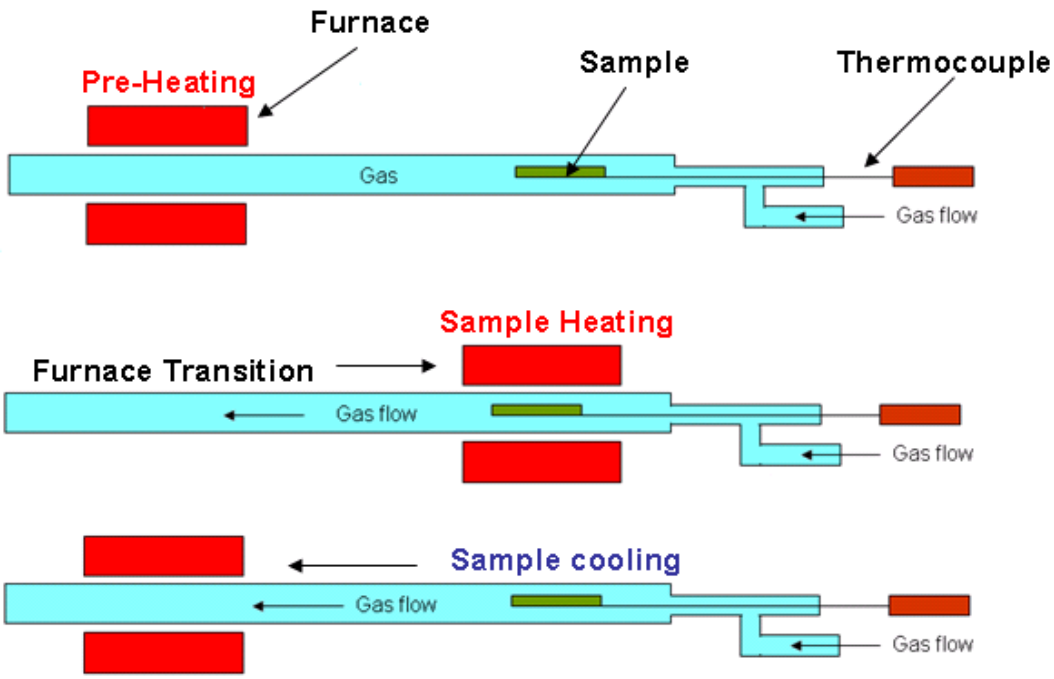

Figure 5.43: Conventional annealing system with high heating and cooling rate facility. High heating and cooling rate is achieved by moving the heated furnace towards and away from the sample

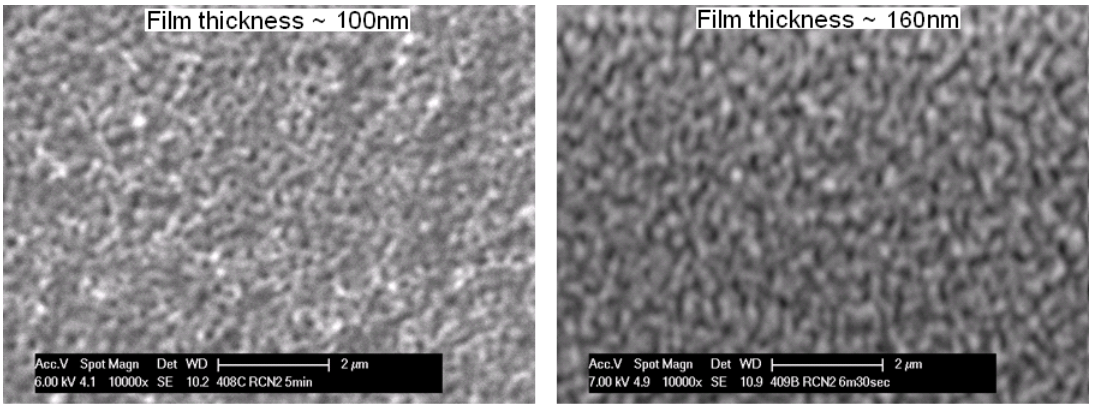

Figure 5.44: Conventionally annealed films with high heating and cooling rate. High heating and cooling rate greatly reduce cracks in the film

It can also be further noted that the role of film thickness in avoiding cracks is not obvious.

Crack free films shown in figure 5.44 were also looking very transparent in comparison to as-deposited and film with wide cracks shown in figure 5.42. Transparencies of these crackless films were measured and compared with those of the both as-deposited and film with wide cracks, given in figure 5.45.

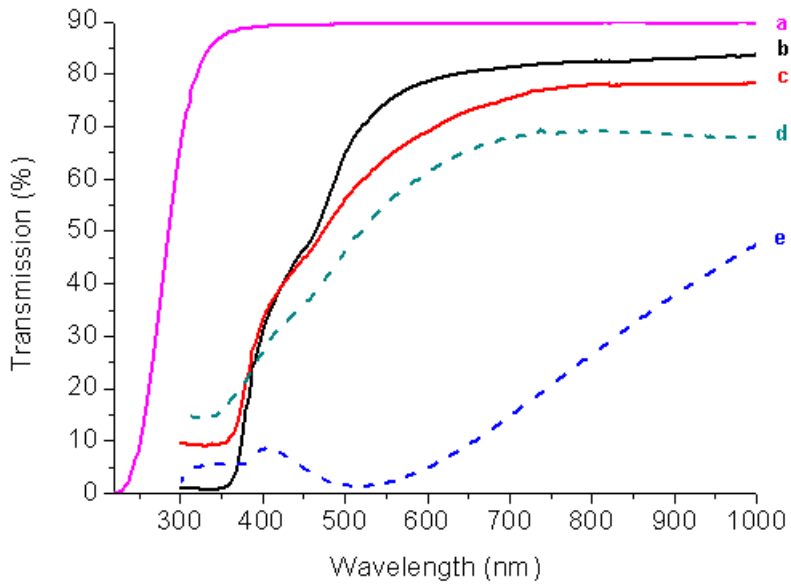

Figure 5.45: Transparency measurement of (a) glass substrate, (b) low thickness film with small cracks, (c) high thickness film with small cracks, (d) as-deposited film, and (e) film with wider cracks. Film with small cracks and low thickness shows high transparency

This comparison shows a notable improvement in transparency by avoiding the cracks formation in the film. Film with lower thickness (∼100 nm) shows slightly higher transparency than that with higher thickness (∼160 nm).

Figure 5.46 shows percent transmittance of our SCO thin film with and without substrate and of the substrte alone.

Transparency of our SCO films (75% trasmittance at 550 nm) shown in the figure 5.45 is in good agreement with the published transparency data about SCO thin films deposited by PLD deposition technique [3, 52, 56, 79] and e-beam evaporation [24].

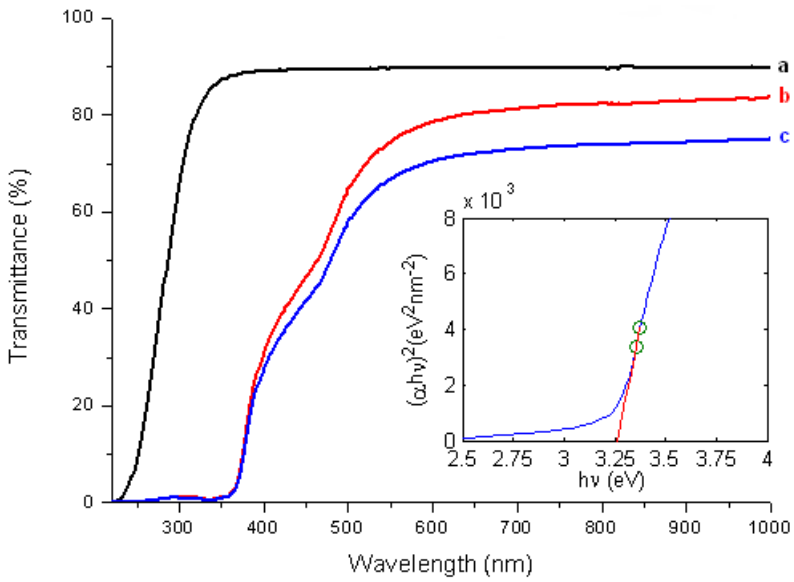

Figure 5.46: Transparency measurement of (a) glass substrate, (b) film without substrate, and (c) film along with substrate. The inset shows plot of $(\alpha h\nu)^2$ versus photon energy $h\nu$

The fundamental absorption, which corresponds to electron excitation from valence band to conduction band can be used to determine the nature and value of the optical bandgap. Relation between absorption coefficients (α) and incident photon energy ($h\nu$) can be written as [56]

$$(\alpha h\nu)^{1/n} = A(h\nu - E_g)$$

where A is a constant, E_g is bandgap of the material, and the exponent n depends on the type of transition. For direct allowed transition $n = 1/2$ and for indirect allowed transition $n = 2$. A plot of $(\alpha h\nu)^2$ versus photon energy $h\nu$ is shown in the inset of figure 5.46. The optical bandgap E_g from the intercept of $(\alpha h\nu)^2$ versus $h\nu$ was found to be 3.26 eV which is in good agreement with theoritical predictions and experimentally obtained value for the SCO bandgap [3, 24, 52, 56, 79].

Movable furnace arrangement shown in the figure 5.43 for high heating rate was

very effective as can be seen from the comparison given in figure 5.47.

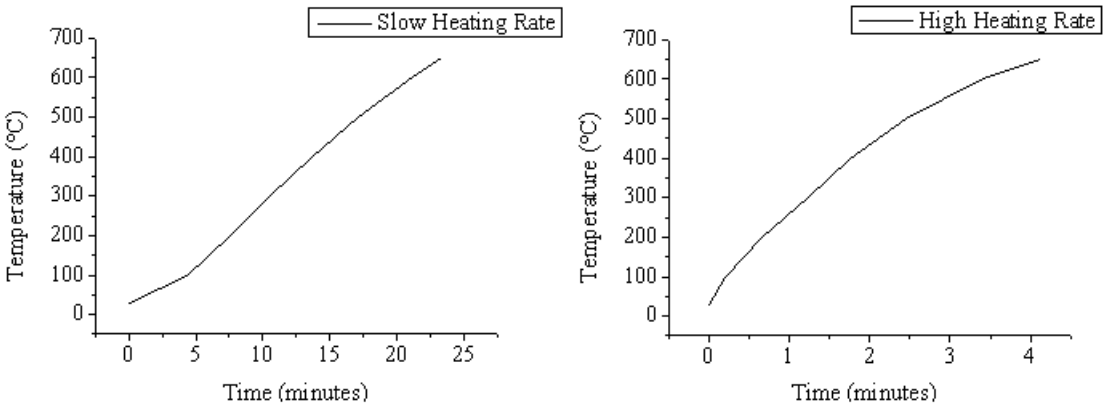

Figure 5.47: Slow and fast heating. Movable pre-heated furnace arrangement shown in figure 5.43 reduce heating time form 24 to 4 minutes

Figure 5.47 shows that moving preheated furnace towards the sample increase the heating rate from 30 °C/minute to 160 °C/minute.

Duration of annealing also plays a key role in crack formation in the film. SEM of the film annealed for variation durations under the same conditions are shown in the figure 5.48.

In order to minimise crack formation in the film during annealing, various substrates were used. And it was found that films deposited on YSZ substrates develop less cracks in comparison to films on glass or Si substrates. However, films annealed for longer duration (irrespective of the substrate) develop wider cracks as shown in the figure 5.45. Besides cracks formation, thickness of the film also decreases with the increase in annealing duration. Reduction of thickness could be due to i) restructuring of the lattice into more dense manner ii) evaporation of the film at high temperature annealing [130] and diffusion of the film contents into the substrate as shown by TEM images in figures 5.29 and 5.33. We have even observed a complete evaporation of the film due long annealing duration as shown in figure 5.49.

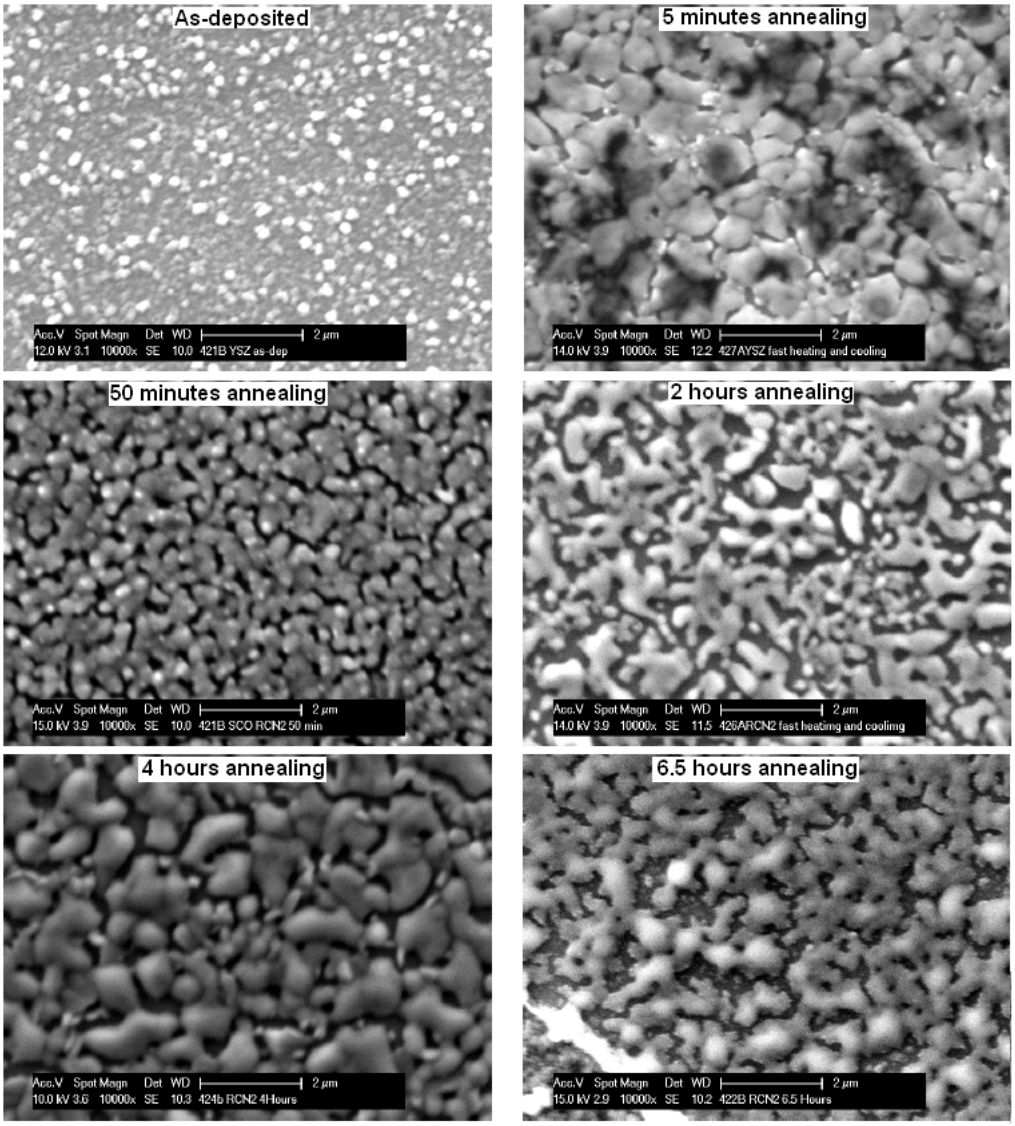

Figure 5.48: Effect of annealing duration on magnitude of crack formation. Longer annealing duration tends to produce wide cracks and vice versa

5.9 Electrical Conductivity Measurement

The electrical conductivity of the SCO film on glass, SiO_2 coated Si, and yttrium stabilized zirconia (YSZ) substrates were measured by four-point probe and Van der Pauw techniques. Four-point probe method measures resistivies in the range 50-200

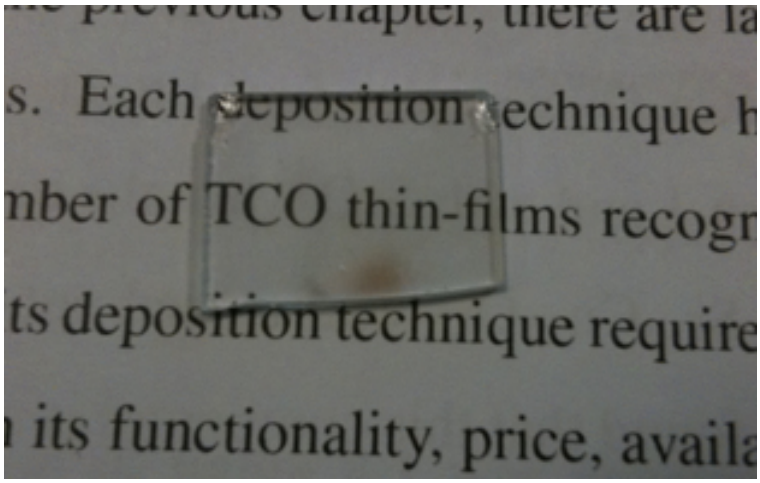

Figure 5.49: Almost complete removal of the film after very long annealing duration

Ωcm (for three samples) for various SCO films and at various points of the same film. The Van der Pauw method measures conductivities in the range 4.3×10^{-2} to 7.6×10^{-3} Scm^{-1} for three samples. If we consider mobility for our SCO film as 5 cm^{2}V^{-1}s^{-1}, then the carrier concentration will be in the range 10^{16} to 10^{17} cm^{-3}. Conductivity of our SCO film deposited by MOCVD is in good agreement with the published data of SCO deposited by PLD [3, 52, 56, 79] and e-beam evaporation [24], where resistivities vary as 10^{-2} - 10^{-3}, mobilities as 0.46 - 6.7 cm^{2}V^{-1}s^{-1}, and concentrations as 6.5×10^{15} - 6.1×10^{17}cm^{-3}. An epitaxial growth on YSZ substrate can further improve the electrical properties of the film, however measuring its optical transparency on YSZ substrate will be difficult to measured accurately. The computer simulation and theoretical calculation shows increase in conductivity of SCO by Ba doping, but considerable effect of the Ba doping has not yet noted experimentally for our Ba doped SCO films in comparison to undoped SCO, because of Ba contamination in the CVD reactor and irreproducibility of the short annealing process.

6

Conclusions and perspectives

6.1 Conclusions

This PhD research work was started in 2007 in the framework of European project NATCO. Our job as partner of the NATCO project was to synthesize efficient p-type TCO thin-film by chemical vapor deposition route. Based on the detailed study of published literature on p-type TCOs and first-principles studies of NATCO partners, Ba-doped SCO ($SrCu_2O_2$) was selected to be our candidate material.

We started our deposition trials with low temperatures as 300 °C, but no uniform deposition was obtained below 450 °C. For $SrCu_2O_2$ phase, we need Cu = 2Sr, therefore our next job was to obtain Cu/Sr = 2 in the film, for which precursor solution with copper concentration Cu = 2Sr was prepared and depositions were performed at 450 °C at various O_2 partial pressure in the deposition reactor. However, every time we obtained higher Cu concentration in the film compared to Sr. Temperatures higher than 450 °C were used for deposition, and it was found that higher deposition temperatures increase Sr contents in the film. Though higher deposition temperature promotes Sr deposition efficiency, films deposited at temperatures $\geq$ 570 °C suffer from low adherence to substrate and rough morphology. For obtaining Cu/Sr = 2 in the film, precursor

solution with low Cu concentration and various deposition temperature in the range 450-570 °C were used, and after a large number of trial depositions we obtained Cu/Sr = 2 in the film depending on nature of the substrate. It was also found by various characterization techniques that as-deposited films are not composed of $SrCu_2O_2$ phase and it can be obtained after some post-deposition annealing steps.

Some interesting findings regarding synthesis of SCO thin film by MOCVD can be summarized in the following points.

1. Deposition and post-deposition annealing conditions vary according to nature of the substrate.

2. Change in O_2 partial pressure and position of the substrate in the deposition chamber change Cu to Sr ratio in the film.

3. Annealing duration for obtaining SCO phase goes on decreasing with the increase in annealing temperature.

4. Longer annealing duration results in the diffusion of film into the substrate, thereby reducing thickness of the film, changing Cu to Sr ratio and results in wider cracks in the films, irrespective of nature of the substrate.

5. High annealing temperature for film on Si substrates provokes epitaxial growth of copper silicates, thereby suppressing formation of SCO. However, there is no such problem with films on glass and YSZ substrates.

6. Fast cooling down to room temperature in the annealing step is necessary to retain SCO phase in the film obtained at high annealing temperature.

7. Fast heating and cooling, and short annealing duration is essential for obtaining SCO thin film with no or less cracks.

8. Cracks in the film reduce optical transparency as well as electrical conductivity.

9. Due to reproducibility problem in annealing conditions, effect of Ba doping on optical and electrical properties of SCO has not yet determined.

6.2 Perspectives and further work

The following points constitute interesting perspectives to the work presented in this thesis.

- A lot of work has been dedicated to the improvement of thin film deposition by MOCVD and post-deposition annealing process. It would be quite interesting to study these improvements and to employ them in future for similar studies. For example, the same optimized deposition and post-deposition annealing conditions have recently employed in our lab for obtaining Sr and Cd-doped Cu_2O thin film by the same MOCVD system to verify the optical bandgap widening of Cu_2O as determined by first-principle calculations by the group of M. Nolan in Tyndall.

- Regarding practical applications of the SCO thin films synthesized by MOCVD in this PhD research, a lot of work still remains to obtain the desired results. However, initial findings of our work have put some milestones on the way towards better performance of p-type TCOs and ultimately towards the development of transparent electronics. Here we also leave some suggestions for the improvement of optoelectrical properties of the MOCVD deposited SCO thin film for the future work in this context:

    1. TEM study for the search of non-conducting amorphous phase on the grain boundaries.

2. Laser and UV exposure as a new RTA of the film to improve interlinking between the grains and remove grain boundary defects.
3. Use of glass substrates of higher thermal expansion coefficients to avoid wider cracks in the film.
4. Epitaxial growth of SCO thin film on YSZ substrate so as to minimize grain boundary effect, thereby increasing its electrical and optical properties.
5. Improvement of the annealing setup in order to measure and control O_2 partial pressure during annealing and study the effect of O_2 partial pressure on phase transformation, so as to make the annealing process reproducible each time.
6. Synthesis of large number of undoped and Ba-SCO thin film samples to search for the factors affecting their optoelectrical properties.
7. Concerning deposition process, use of UV or plasma assisted reactor to avoid formation of strontium carbonates and deposit SCO thin film at reduced temperature which is necessary for the use in flexible electronics applications.

.....End.....

After all these years, I do not know what I may appear to the world, but to myself, I seem to have been only a boy playing on the sea-shore and diverting myself in, now and then, finding a smoother pebble or a prettier shell than ordinary whilst the great ocean of truth lay all undiscovered before me. — Isaac Newton

Bibliography

[1] H. Hosono et al. *Journal of Crystal Growth*, 237-239:496–502, 2002.

[2] X. Nie et al. *Physical Review Letters*, 88, No 6:066405, 2002.

[3] A. Kudo et al. *Appl. Phys. Lett.*, 73 No. 2:220–222, 1998.

[4] Wilfrid Meffre. *Rare earth dopped oxides for waveguides; prepared by liquid source MOCVD, for applications in integrated optics (in French)*. PhD thesis, Grenoble Institute of Technology, 1999.

[5] P.P. Edwards et al. *Dalton Transaction*, pages 2995–3002, 2004.

[6] A.N. Banerjee and K.K. Chattopadhyay. *Progress in Crystal Growth and Characterization of Materials*, 50:52–105, 2005.

[7] X. Nie et al. *Physical Review B*, 65:075111, 2002.

[8] Su-Huai Wei et al. *29th IEEE - Photovoltaic specialists conference.*, pages 496–499, 2002.

[9] G. Kate et al. *J. Mater. Chem*, 20:1086–1096, 2010.

[10] Alex Martinson and D. Ginley. Synthesis of single phase srcu2o2 from liquid precursors. *Journal of Young Investigators*, 10. No.3, 2004.

[11] M. J. Hampden-Smith and T. T. Kodas. *Chem. Vap. Deposition*, 1, No. 1:8–23, 1995.

[12] Jr John M. Blocher. *J. Vac. Sci. Technol*, 11, No. 4:680–686, 1974.

[13] H. Kawazaoe et al. *MRS Bull*, 25. No. 8:28–36, 2000.

[14] R. S. Roth et al. *J. Am. Ceram. Soc.*, 72, No. 8:1545–1549, 1989.

[15] C. B. Alcock and Baozhen Li. *J. Am. Ceram. Soc.*, 73, No. 5:1176–1180, 1990.

[16] R. O. Suzuki et al. *J. Am. Ceram. Soc.*, 75, No. 10:2833–2842, 1992.

[17] C.L. Teske and Hk. Muller-Buschbaum. *Z. Anorg. Allg. Chem.*, 379:113–121, 1970.

[18] V. Varadarajan et al. *Thin Solid Films*, 488:173–177, 2005.

[19] H. Bach and D. Krause. *Thin Films on Glass*. Springer-Verlag, Berlin, 2003.

[20] Zhigang R. Li and Hong Meng. *Organic Light-emitting Materials and Devices*. CRC Press, USA, 2007.

[21] J.E. Medvedeva and A.J. Freeman. *Europhys. Lett*, 69. No.4:583–587, 2005.

[22] T. Minami el al. *Semicond. Sci. Technol*, 20:S35–S44, 2005.

[23] T. Minami. *MRS Bull*, 25 No.8:38–44, 2000.

[24] E. Bobeico et al. *Thin Solid Films*, 444:70–74, 2003.

[25] Su Sheng et al. *Phys. Stat. sol (a)*, 203. No. 8:1891–1900, 2006.

[26] R.G. Gordon. *MRS Bull*, 25. No. 8:52–57, 2000.

[27] K. Baedeker. *Ann. Phys.*, 22:749–766, 1907.

[28] G. Rupprecht. *Zeitschrift fur Physik*, Bd 139S:504–517, 1954.

[29] G. Haacke. *Ann. Rev. Mater. Sci.*, 7:73–93, 1977.

[30] B.G. Lewis and D.C. Paine. *MRS Bull*, 25 No.8:22–27, 2000.

[31] Q. Zhou et al. *Materials Letters*, 61:531–534, 2007.

[32] H. Sato et al. *Thin Solid Films*, 236:27–31, 1993.

[33] H. Kawazoe et al. *Nature*, 389:939–942, 1997.

[34] H. Hosono. *Thin Solid Films*, 515:6000–6014, 2007.

[35] D.S. Ginley and C. Bright. *MRS Bull*, 25. No. 8:15–18, 2000.

[36] A.J. Freeman et al. *MRS Bull*, 25. No. 8:45–51, 2000.

[37] J. Lewis et al. *Mat. Res. Soc. Symp. Proc.*, 814:I8.5.1–I8.5.10, 2004.

[38] K.A. Sierros et al. *Thin Solid Films*, 517:2590–2595, 2009.

[39] A. Rahy et al. *Applied Surface Science*, 255:7084–7089, 2009.

[40] H. Ohta et al. *Solid State Electronics*, 47:2261–2267, 2003.

[41] Task 1.2 (2006) NATCO 18 Month Report WP1.

[42] H. Demiryont. *SPIE Newsroom DOI: 10.1117/2.1200608.0340.*, 2007.

[43] Review of TCO Thin Films. http://www.eng.tau.ac.il/∼boxman/TCO%2020singapore%20207%2020July%202008-rb-sg%5B3%5D.doc.

[44] A. R. Babar et al. *J. Phys. D: Appl. Phys*, 41:135404, 2008.

[45] J. Ru and R. G. Gordon. *Mat. Res. Soc. Symp. Proc.*, 283:891–896, 1993.

[46] Z. Q. Yu et al. *Electrochemical and Solid-State Letters*, 11 No 5:B76–B78, 2008.

[47] M. Okuyama et al. *Appl. Phys A.*, 21 No 4:339–343, 1980.

[48] J. Koo et al. *Mat. Res. Soc. Symp. Proc*, 474:61–66, 1997.

[49] E. Dogheche et al. *Applied Optics.*, 37 No. 19:4245–4248, 1998.

[50] U. Rabibisoa et al. *Ferroelectrics*, 225:303–310, 1999.

[51] H. Hosono et al. *Vacuum*, 66:419–425, 2002.

[52] H. Kawazoe et al. Oxide thin film. *US Patent (US 6294274 B1)*, Sep. 25, 2001.

[53] C. Lv et al. *Jpn. J. Appl. Phys*, 46 No. 4B:2603–2808, 2007.

[54] H. Mizoguchi and P. M. Woodward. *Chem. Mater.*, 16 No. 25:5233–5248, 2004.

[55] H. Ohta et al. *International Journal of Modern Physics B*, 16 No. 1 & 2:173–180, 2002.

[56] Su Sheng et al. *Semicond. Sci. Technol*, 21 No 5:586–590, 2006.

[57] K. Ramamoorthy et al. *Current Applied Physics*, 6:103–108, 2006.

[58] A. Tiburcio-Silver et al. *J. Appl. Phys.*, 76, No. 3:1992–1994, 1994.

[59] A. Jain et al. *Solid State Electronics*, 50 No. 7-8:1420–1424, 2006.

[60] A. Walsh et al. *Physical Review B*, 78:075211, 2008.

[61] David O. Scanlon and Graeme W. Watson. *Chem. Mater*, 21 No. 22:5435–5442, 2009.

[62] Jorge I. Cisneros. *Applied Optics*, 37 No. 22:5262–5270, 1998.

[63] O. Vigil et al. *J. Phys.: Condens. Matter*, 17:6377–6384, 2005.

[64] Plasma oscillation. http://en.wikipedia.org/wiki/plasma_oscillation.

[65] L. Solymar and E. Shamonina. *Waves in Metamaterials*. Oxford University Press Inc., New York, 2009, Page - 77.

[66] James J. Y. Hsu. *Nanocomputing: computational physics for nanoscience and nanotechnology*. Pan Stanford Publishing Ptc, Ltd. Singapore, 2008, page - 262.

[67] John. F. Wager. *Science*, 300:1245–1246, 2003.

[68] S. B. Zhang et al. *J. Appl. Phys*, 83, No. 6:3192–3196, 1998.

[69] H. Ohta and H. Hosono. *Materials Today*, 7. No. 6:42–51, 2004.

[70] H. Yanagi et al. *Journal of Electroceramics*, 4, No. 2-3:407–414, 2000.

[71] J. Robertson et al. *Thin Solid Films*, 411:96–100, 2002.

[72] J.P. Hu et al. *Chemical Physics Letters*, 450:39–43, 2007.

[73] Min-Ling Liu et al. *Key Engineering Materials*, 368-372:666–668, 2008.

[74] Min-Ling Liu et al. *J. Appl. Phys*, 102:116108, 2007.

[75] C.C.B Lynch et al. *Chemical Physics Letters*, 401:223–226, 2005.

[76] Wei-Wei Zhuang et al. Sco thin film. *US Patent (US 7087526 B1)*, 2006.

[77] D. Louloudakis et al. *phys. stat. sol. (a)*, 207, No. 7:1726–1730, 2010.

[78] M. Modreanu et al. *Thin Solid Films*, 515:8624–8631, 2007.

[79] E. L. Papadopoulou et al. *Thin Solid Films*, 516:1449–1452, 2008.

[80] B. Roy et al. *National Center for Photovoltaics and Solar Program Review Meeting*, Colorado, USA, 2003.

[81] Y. Nakamura et al. *Journal of the European Ceramic Socity*, 25:2167–2170, 2005.

[82] Wei-Wei Zhang et al. *US Patent (US 2007/0054042 A1)*, 2007.

[83] J. L. Deschanvres et al. *phys. stat. sol. (a)*, 205, No. 8:2013–2017, 2008.

[84] A. Kudo et al. *Appl. Phys. Lett.*, 75, No. 18:2851–2853, 1999.

[85] H. Ohta et al. *Appl. Phys. Lett.*, 77, No. 4:475–477, 2000.

[86] H. Ohta et al. *J. Appl. Phys*, 89, No. 10:5720–5725, 2001.

[87] Final Technical Report (2008) NATCO project No: FP6-511925.

[88] Michael Nolan. *Thin Solid Films*, 516:8130–8135, 2008.

[89] NTCO Final Report to European Comission.

[90] Michael Nolan and Simon D. Elloit. *Chem. Mater*, 20, No. 17:5522–5531, 2008.

[91] S. Park et al. *Appl. Phys. Lett.*, 80:4393–4394, 2002.

[92] H. Yanagi et al. *Journal of Solid State Chemistry*, 175, No. 1:34–38, 2003.

[93] R. K Bhandari. *Jpn. J. Appl. Phys*, 43, No. 10:6890–6893, 2004.

[94] K. Ueda et al. *J. Appl. Phys.*, 89, No. 3:1790–1793, 2001.

[95] H. Yanagi et al. *Mat. Res. Soc. Symp. Proc*, 666:F3.14.1–F3.14.6, 2001.

[96] R. Nagarajan et al. *J. Appl. Phys*, 89, No. 12:8022–8025, 2001.

[97] M. Snure and A. Tiwari. *Appl. Phys. Lett.*, 91, No. 9:092123, 2007.

[98] N. Duan et al. *Appl. Phys. Lett.*, 77, No. 9:1325–1326, 2000.

[99] M. K. Jayaraj. *Mat. Res. Soc. Symp. Proc.*, 666:F4.1.1–F4.1.9, 2001.

[100] Y. Ogo et al. *Phys. Status Solidi (A)*, 206, No. 9:2187–2191, 2009.

[101] U. Kumar Barik et al. *Thin Solid Films*, 429 No. 1-2:129–134, 2003.

[102] H. Hiramatsu et al. *Appl. Phys. Lett.*, 82 No. 7:1048–1050, 2003.

[103] H. Hiramatsu et al. *Chem. Mater.*, 20, No. 1:326–334, 2008.

[104] K. Ueda et al. *J. Appl. Phys.*, 102, No. 11:113714, 2007.

[105] H. Mizoguchi et al. *Appl. Phys. Lett.*, 80, No. 7:1207–1209, 2002.

[106] Zhenguo Ji et al. *Phys. Stat. sol (c)*, 5, No. 10:3364–3367, 2008.

[107] John R. Arthur. *Specimen handling, preparation, and treatments in surface characterization*. Plenum Publishers, New York, 1998.

[108] A. Z. Moshfegh et al. *Proceedings of the International Workshop on Physics and Technology of Thin Films*. World Scientific Publishing Co. Ptc. Ltd USA, 2004.

[109] Krishna Seshan. *Handbook of Thin Film Deposition: Processess and Technologies*. William Andrew Publishing/Noyes New York, 2002.

[110] Yi Liu Z.L. Wang and Ze Zhang. *Handbook of Nanophase and Nanostructured Materials: Volume I*. Kluwer Acadamic/Plenum Publishers, New York, 2003.

[111] M. Kitabatake K. Wasa and H. Adachi. *Thin Films Material Technology: Sputtering of Compound Materials*. Brent Beckley / William Andrew, Inc New York, 2004.

[112] Charles A. Bishop. *Vacuum deposition onto webs, films, and foils*. William Andrew Publishing, New York, 2007.

[113] J. I. Pankove and T. D. Moustakas. *Semiconductors and semimetals: a treatise. Gallium Nitride (GaN) II*. Academic Press, San Deigo, 1999.

[114] Jong-Hee Park and T. S. Sudarshan. *Chemical Vapor Deposition*. ASM International, 2001.

[115] Robert V. Coleman and Karl Lark-Horovitz. *Solid state physics*. Academic Press Inc, New York, 1974.

[116] Hugh O. Pierson. *Handbook of chemical vapor depostion*. Noyes Publications, New York, 1999.

[117] Kasturi L. Chopra and Suhit Ranjan Das. *Thin film solar cells*. Plenum Press, New York, 1983.

[118] Yun Chan Kang et al. *JOURNAL OF MATERIALS SCIENCE LETTERS*, 21:1027–1029, 2002.

[119] M. Haruna H. Nishihara and T. Suhara. *Optical integrated circuits*. McGraw-Hill Professional Publishing, 1989.

[120] Y. Pauleau. *Chemical physics of thin film deposition processes for micro- and nano-technologies*. Kluwer Acadamic Publishers, Netherland, 2002.

[121] H. Mader D. Widmann and H. Friedrich. *Technology of integrated circuits*. Springer-Verlag, Berlin, 2000.

[122] A. Busnaina. *Nanomanufacturing handbook*. Taylor & Francis Group, LLC. USA, 2007.

[123] L. E. Scriven. *Mat. Res. Soc. Symp. Proc*, 121:717–729, 1988.

[124] T. Wagner. Thin film science http://www.mpg.de/pdf/europeanwhitebook/wb_materials_196_2

[125] R. F. Bunshah. *Handbook of deposition technologies for films and coatings*. Noyes Publications, New Jersey, 1994.

[126] Maria Gamboa-Aldeco John O'M. Bockris, Amulya K. N. Reddy. *Modern electrochemistry, Volume 2*. Kluwer Acadamic / Plenum Publishers, New York, 2000.

[127] Orlando Auciello and Alan R. Krauss. *In situ real time characterization of thin films*. John Wiley & sons, Inc. Canada, 2001.

[128] Thomas B. Elloit. *Trends in Semiconductor Research*. Nova Science Publishers, Inc. New York, 2005.

[129] Donald L. Smith. *Thin Film Deposition: Principles and practice*. McGraw-Hill, Inc. USA, 1995.

[130] C. R. Kim et al. *Current Applied Physics*, 10:S294–297, 2010.

[131] B. Rau et al. *Mat. Res. Soc. Symp. Proc*, 910:0910–A25–03, 2006.

[132] S. Marsillac et al. *Applid Surface Science*, 15:171–179, 1999.

[133] G. Aguilar et al. *Thin Solid Films*, 517:5728–5733, 2009.

[134] A. T. Foiry. Mehods in rapid thermal annealing. *8th International Conference on Advanced Thermal Processing of Semiconductors, Gaithersburg, Md*, pages 15–25, 2000.

[135] F. Roozeboom and N. Parekh. *J. Vac. Sci. Technol. B*, 8, No. 6:1249–1259, 1990.

[136] Fred Roozeboom. *Advances in rapid thermal and integrated processing*. Kluwer Acadamic Publishers, Netherland, 1996.

[137] Misirlioglu et al. *J. Appl. Phys.*, 99:104103, 2006.

[138] I. Ozen and M. Ali Gulgun. *Advances in Science and Technology*, 45:1316–1321, 2006.

[139] Liping Zhu et al. *International Journal of Modern Physics B*, 20, No 25, 26 & 27:4034–4039, 2006.

[140] Shigeyuki Nakamura. In *3rd World Conference on Photovolraic Energy Conversion*, May 11-18, 2003 Osaka, Japan.

[141] K. Y. Cheong and F.A. Jasni. *Microelectronics Journal*, 38:227–230, 2007.

[142] S. Halder et al. *Materials Science and Engineering B*, 133:235–240, 2006.

[143] Jianou Shi and James C. Mitchener. *US Patent (US 6284050 B1)*, 2001.

[144] J. M. Jacques et al. *Mater. Res. Soc. Symp. Proc.*, 914:0914–F01–07, 2006.

[145] F. Wenner. *Bull. Bureau Stand*, pages 469–478, 1916.

[146] L. J. Van der Pauw. *Philips Tech. Rev*, 20:220–224, 1958.

[147] Chemical vapor deposition. http://en.wikipedia.org/wiki/chemical_vapor_deposition.

[148] W. A. Bryant. *Journal of Materials Science*, 12:1285–1306, 1997.

[149] Andrew R. Barron. Chemical vapor deposition. Technical report, http://cnx.org/content/m25495/1.2/, 2009.

[150] NASA. http://www.grc.nasa.gov/www/k-12/airplane/boundlay.html.

[151] J. P. Hirth and G. M. Pound. *Condensation and Evaporation*. Pergammon Press, Oxford, 1963.

[152] Jong-Hee Park and T. S. Sudarshan. *Chemical Vapor Deposition*. ASM International, 2001.

[153] M. Murakawa et al. *Thin Solid Films*, 308-309, No. 31:245–248, 1997.

[154] Pascal Voort E. F. Vansant and Karl C. Vrancken. *Characterization and chemical modification of the silica surface*. Elsevier Science B.V. Netherland, 1995.

[155] Marshall Sittig. Metal-organic compounds. *AMERICAN CHEMICAL SOCIETY*, 23:v, 1959.

[156] B. E. Yoldas. *Journal of Materials Science*, 12, No. 6:1203–1208, 1977.

[157] Metal organic chemical vapor deposition. http://physics.units.it/Ricerca/docXXciclo/Fis02/epitaxy3.pps.

[158] A. Fujiwara and S. Hiramatsu. Mocvd apparatus and mehods. *US Patent (US 2005/0014366 A1)*, 2006.

[159] Safa O. Kasap and Peter Capper. *Springer handbook of electronic and photonic materials*. Springer Science + Business Media Inc, 2006.

[160] A. Wang et al. *Proceedings of the National Academy of Science (PNAS) USA*, 98, No. 13:7113–7116, 2001.

[161] B. G. Gribov. *Russian Chemical Reviews*, 42, No. 11:893–903, 1973.

[162] Guglielmo G. Condorelli et al. *Chemical Vapor Deposition*, 5, No. 1:21–27, 1999.

[163] John W. Benko et al. Mocvd method and apparatus. *US Patent (US 1993/00518756 A)*, 1993.

[164] Coordination complex. http://en.wikipedia.org/wiki/Coordination_complex.

[165] Organometallic chemistry. http://en.wikipedia.org/wiki/Organometallic_chemistry.

[166] Metalorganics. http://en.wikipedia.org/wiki/Metalorganics.

[167] J.P. Senateur et al. French patent, fr 2,707,671 (1993).

[168] J.P. Senateur et al. European patent, ep 730,671 (1994).

[169] J.P. Senateur et al. Us patent, us 945,162 (1999).

[170] Titipun Thangtem et al. *Materials Letters*, 64, No. 4:510–512, 2010.

[171] Zhagn Ming-Xaun et al. *Chinese J. Struc. Chem*, 27, No. 10:1223–1229, 2008.

[172] G. Papadimitropoulos et al. *journal of physics: conference series*, 10:182–185, 2005.

[173] D. M. Fernandes et al. *Materails of Chemistry and Physics*, 115:110–115, 2009.

[174] B. Balamurugan and B.R. Mehta. *Thin Solid Films*, 396:90–96, 2001.

[175] Chung-Cherng Lin and Lin-Gun Liu. *J. Phys. chemi. Solids*, 58, No. 6:977–987, 1997.

[176] Soumyendu Guha et al. *Physical Review B*, 43, No. 16:13092–13101, 1991.

[177] J. F. Xu et al. *Journal of Raman Spectroscopy*, 30, No. 5:413–415, 1999.

[178] Bibo Li et al. *Physical Review B*, 59, No. 3:1645–1648, 1991.

[179] M. V. Abrashev et al. *Physica C*, 280:297–303, 1997.

[180] Dae-Kue Hwang et al. *Applied Physics Letters*, 90:021106, 2007.

[181] C.X. Li et al. *IEEE Conference on Electron Devices and Solid-State Circuits*, pages 185–188, 2007.

[182] M. V. Abrashev et al. *Physical Review B*, 55, No. 14:9136–9141, 1997.

[183] Z. V. Popovie et al. *Physica C*, 351:386–394, 2001.

[184] Xingiang Zhou et al. *Physica C*, 282-287:1011–1012, 1997.

[185] H. Holache-Carranco et al. *5th International Conference on Electrical Engineering, Computer Science and Atutomatic Control*, pages 421–424, 2008.

[186] A. Compaan and H. Z. Cummins. *Physical Review B*, 6, No. 12:4753–4757, 1972.

[187] M. P. Singh and S. A. Shivashankar. *Mat. Res. Soc. Symp. Proc*, 749:201–206, 2003.

[188] Kaustubh S. Gadre and T. L. Alford. *Thin Solid Films*, 394:125–130, 2001.

[189] A. Furuya et al. *IEEE Transaction on Magnetics*, 37, No. 4:2407–2410, 2001.

[190] Shigeyuki Nakamura. *3rd World Conference on Photovoltaic Energy Conversion*, pages 422–425, May 11-18, 2003 Osaka, Japan.

[191] R. Huang et al. *Engineering Fracture Mechanics*, 70:2513–2526, 2003.

Abtract

Transparent Conducting Oxides (TCOs) are used in number of technological applications such as solar cells, liquid crystal displays, touch screen etc. However, these technological applications are limited to n-type TCOs due their good electrical conductivity and optical transparency. Copper oxides with delafossite structures ACuO2 (A being trivalent cation) or $SrCu_2O_2$ shows good p-type electrical conductivity and good optical transparency in the visible spectrum. Among the proposed p-type TCOs, $SrCu_2O_2$ is considered a promising one due to its large direct bandgap. In this PhD thesis MOCVD (metal organic chemical vapor deposition) technique is used to deposit thin films of SrCu2O2. The as-deposited film by MOCVD do not contain SrCu2O2 phase and can only be obtained after two annealing steps under oxygen then under argon or in one annealing step under nitrogen. The electrical and optical properties measured for SrCu2O2 thin films are in good agreement with the published data.

Keywors: MOCVD, Annealing, TCOs

Résumé

Les semi-conducteurs transparents de type oxyde, communément appelés TCO (Transparent Conducting Oxides) sont utilisés comme électrodes transparentes dans des nombreux d'applications telles que les cellules solaires, les écrans à cristaux liquides, les écrans tactiles et autres. Toutefois, les applications technologiques sont actuellement limitées puisque les TCO possédant des propriétés électriques et optiques satisfaisantes sont uniquement des semi-conducteurs de type n. Les oxydes de cuire de structures delafossite ACuO2 (où A est un cation trivalent) ou du type SrCu2O2, présentent des prometteuses avec un comportement de semi-conduction de type P et une faible absorption optique dans le spectre visible. Dans cette thèse, le systèm MOCVD (Dépôt chimique en phase vapeur du métal organique) a été utilisé pour le dépôt des couches minces de SrCu2O2. Cette phase est obtenue après quelques étapes de recuit sous oxygène puis argon, ou azote uniquement avec en particulier la nécessité de réalier des recuit rapaides. Les propriétés électriques et optiques mesurées pour la couche mince de SrCu2O2 ont un ordre de grandeur similaire à ce qui est publié dans la littérature.

Mot clés : MOCVD, Recuit, TCOs